## Numerical Study on Liquid-Vapor Phase

### Change with Applications in Vapor Bubble

### **DYNAMICS**

By

### Raunak Bardia

A dissertation submitted in partial fulfillment of the requirements for the degree of

Doctor of Philosophy

(Mechanical Engineering)

at the

University of Wisconsin - Madison

2020

Date of final oral examination: 01/27/2020

The dissertation is approved by the following members of the Final Oral Committee:
Mario Trujillo (Thesis Advisor), Associate Professor, Mechanical Engineering
Riccardo Bonazza, Professor, Engineering Physics
Gregory Nellis, Professor, Mechanical Engineering
Shiva Rudraraju, Assistant Professor, Mechanical Engineering
Jennifer Franck, Assistant Professor, Engineering Physics

### Acknowledgements

The over 5 years of graduate school that culminates with this thesis has been a very humbling, as well as a gratifying experience. The persistent work that I needed to finish this thesis would have been a lot more difficult without the love and support of my parents and sisters. Also, I thank my fiancee, Nidhi, whom I met here in Madison. I thank her for persevering with me and encouraging me every day to achieve the goal of finishing my dissertation.

I sincerely thank my thesis advisor, Prof. Mario Trujillo, for his thoughtful guidance throughout my time in Madison. I am thankful for the group that I worked in and I express my heartfelt appreciation for all the group members: Arpit Agarwal for hours of endless discussions about research and otherwise; Dr. Lakshman Anumolu for always being available for help; Dr. Douglas Ryddner for helping me settle in the group; Michael Mason, Chia-Wei Kuo, Mohan Ananth and Soumil Gurjar for their enthusiasm and necessary critique that helped me improve my communication skills. I would also like to extend my thanks to Joshua Leach for keeping our systems ready and sharp for uninterrupted functioning. Besides the group, I am grateful to the National Science Foundation and the Department of Mechanical Engineering for the financial support that was essential to continue my Ph.D.

Besides family and work colleagues, another important aspect helped shape me and my work in the past years. I would like to express a deep sense of gratitude towards my roommates, Sachin Muley, and Aashrith Koundinya, who have been great comrades in my Ph.D. journey outside of the office. At last, I would like to thank my friends, Yash, Neha, Nitish, Debaditya, Kaivalya, Shalaka, Prashant, Ashwin, Kshiteej, and Vivek, who helped to create a safe haven for me here in Madison, which helped me prosper in my work.

### **Preface**

This dissertation describes the contents of two papers that have been published and a final project that has been completed partly. Another project that was completed prior to the official start of the Ph.D. program as part of my Master's thesis has also been listed here. Details of all these projects and about contributions from each individual involved in these projects have been noted below.

1. **Doctoral Thesis - Published Work** # 1: <u>Bardia, Raunak</u>, and Mario F. Trujillo.

"Assessing the physical validity of highly-resolved simulation benchmark tests for flows undergoing phase change." *International Journal of Multiphase Flow* 112 (2019): 52-62. [1]

My contributions to this work:

- Identified the assumptions related to constant vapor density and interface temperature, which are taken by the highly-resolved simulation (HRS) studies and were assessed as part of this work.
- Formulated and developed the numerical model for spherical bubble growth, which was used as a benchmark for comparison with previously published HRS results.
- Derived the analytical expression, which defined the time period of bubble growth for which the HRS assumptions remained valid.

Contributions by Mario F. Trujillo:

• Developed the original Arbitrary Lagrangian-Eulerian methodology [2], which was modified and used in the benchmark bubble growth model in this study.

- Wrote the section on the relevance of the presented analysis in case of departure from sphericity for a vapor bubble.
- Derived proof for the analytical expression for the energy balance of a bubble used in the bubble growth model.
- Contributed to the copyediting, and proofing of the manuscript.
- Doctoral Thesis Published Work #2: <u>Bardia, Raunak</u>, and Mario F. Trujillo.
   "An improved categorization of vapor bubble collapse: Explaining the coupled nature of hydrodynamic and thermal mechanisms." *International Journal of Heat and Mass Transfer* 145 (2019): 118754.[3]

My contributions to this work:

- Compiled the literature on bubble collapse to identify the main ideas of intermediate collapse and collapse categorization that was analyzed.
- Formulated and developed the numerical model for spherical bubble collapse, which was the primary tool of analysis in this work.
- Conceptualized the categorization metric, and the final categorization map, which
  was the major contribution of this work.

#### Contributions by Mario F. Trujillo:

- Developed the original Arbitrary Lagrangian-Eulerian methodology [2], which was modified and used in the benchmark bubble growth model in this study.
- Contributed to the copyediting, and proofing of the manuscript.

3. **Doctoral Thesis Final Project (unpublished)**: <u>Bardia, Raunak</u>, and Mario F. Trujillo. "A consistent finite volume formulation for two-phase flow problems with phase change using Ghost Fluid Method (GFM)."

My contributions to this work:

- Performed a thorough test on the basic two-phase flow solver that was used as a starting point for further code development.
- Derived the liquid volume fraction advection equation for phase change and introduced the novel concept of effective flux used in the numerical implementation
- Overhauled the Ghost Fluid Method for use in a finite volume framework
- Coded all the changes in base solver needed to implement the interface advection and solving the momentum equation for two-phase flow with phase change.

Contributions by Mario F. Trujillo:

- Derived the reference expressions for the conservation of a general, physical quantity for both finite difference and finite volume methods
- Directed the use of Ghost Fluid Method instead of an earlier idea of in-cell reconstruction to capture interfacial discontinuities
- 4. Masters' Thesis Published Work # 3: <u>Bardia, Raunak</u>, Zhi Liang, Pawel Keblinski, and Mario F. Trujillo. "Continuum and molecular-dynamics simulation of nanodroplet collisions." *Physical Review E* 93, no. 5 (2016): 053104.

  My contributions to this work:

- Implemented the evaluation of kinetic energy for comparison with Molecular Dynamics (MD) simulations in OpenFOAM.
- Performed the continuum simulations in OpenFOAM for sensitivity analysis, and final comparison with MD simulations.

### Contributions by Zhi Liang:

- Performed all the MD simulations in an in-house solver developed in their research group at RPI.
- Used MD analysis to evaluate continuum level properties like density, viscosity, and surface tension, which were used in continuum simulations.

### Contributions by Pawel Keblinski:

• Contributed to the copyediting, and proofing of the manuscript.

### Contributions by Mario F. Trujillo:

- Conceptualized the section on numerical sensitivities, which provided insights into the limitations of continuum simulations at smaller length scales.
- Contributed to the copyediting, and proofing of the manuscript.

### **Abstract**

This thesis presents a detailed analysis of vapor bubble dynamics and the interfacial process of liquid-vapor phase change. A spherically symmetric model for single vapor bubble is employed to present a numerical and theoretical analysis of the intermediate bubble collapse, where in contrast to the thermally induced or inertia dominated collapse, both the effects of liquid-vapor interfacial heat transfer and the advection of the surrounding liquid play an important role. The contrast in thermal, intermediate, and inertial behavior of collapse is represented in the form of a regime map defined by two non-dimensional quantities,  $B_{sat}$  and  $\xi$ , which can be directly evaluated from the initial system conditions of collapse.

The same model is also used to simulate a spherically symmetric bubble growth configuration to assess the physical validity of a constant interface temperature assumption made by Highly-Resolved Simulation (HRS) studies aimed at solving flows undergoing phase change. Results show that HRS predictions are inaccurate during the initial period of bubble growth, which coincides with the inertial growth stage. A closed-form expression for a threshold time is derived, beyond which the commonly employed HRS assumptions hold.

Forgoing the limitation of spherical symmetry, the second theme of this thesis is on the development of a general two-phase flow solver that can handle the phase change process. Under a finite volume framework using a geometric Volume of Fluid (gVoF) approach, two key challenges with phase change flows have been addressed in this work, namely, (i) added deformation of the interface, and (ii) capture of velocity and pressure gradient discontinuity at the interface, both caused due to phase change. To track the interface in the gVoF scheme, an effective flux is defined that captures the effect of phase change on interface motion. This

method improves upon the source term approach used in other studies. For the solution of velocity, and pressure, a ghost fluid approach has been implemented, which is the first of its kind in a VoF-based phase change solver.

# Contents

1	Inti	roducti	on	1	
2 An In		Impro	oved Categorization of Vapor Bubble Collapse: Explaining the	•	
	Cot	ipled N	Nature of Hydrodynamic and Thermal Mechanisms	5	
	2.1	Litera	ture Review	6	
	2.2	Descri	ption of the Collapse Study	10	
	2.3	Comp	ressible Vapor Saturated Interface (CVSI) Solution for Bubble Collapse	11	
		2.3.1	Description of the Physical System & the CVSI Model	13	
		2.3.2	Numerical Solution	18	
		2.3.3	Validation of the CVSI Model	22	
	2.4	Interm	nediate Bubble Collapse	24	
		2.4.1	Explaining the Different Characteristics of Intermediate Collapse	29	
	2.5	Vapor	Bubble Collapse Categorization	32	
		2.5.1	Metric for Bubble Collapse	37	
		2.5.2	Categorization Map	40	
	2.6	Summ	OPV	43	

3	Assessing the Physical Validity of Highly Resolved Simulation Benchmark		
	Tes	ts for Flows Undergoing Phase Change	45
	3.1	Validating the CVSI Solution	47
	3.2	Departure from Physically Accurate Behavior in Published HRS Results	49
		3.2.1 Identifying Apriori Conditions Favorable to the Current HRS Treatment	55
	3.3	Summary	61
4	Nui	merical Method Development for Two-Phase Flows With Phase Change	63
	4.1	A Review of Phase Change Simulation Methods	64
	4.2	Framework for Phase Change Solver Development	71
		4.2.1 Advection Tests	72
		4.2.2 Surface Tension and Pressure Velocity Coupling Tests	76
	4.3	Phase Change Numerical Method Development	83
		4.3.1 Alpha Equation	83
		4.3.2 Pressure - Velocity Coupling (Ghost Fluid Method)	89
	4.4	Solver Development: ghostFluidPhaseChangeFoam	100
		4.4.1 Phase Change Tests	100
5	Sun	nmary & Future Work	108
$\mathbf{A}_{\mathrm{j}}$	ppen	adices	113
A	Nui	merical Convergence of CVSI Model Solutions	114
$\mathbf{R}$	Rel	evant Derivations for Phase Change	119

	B.1	Relation between Material Volume and Control Volume with a surface of	
		discontinuity	119
	B.2	Generalized equation for velocity divergence for a Material Volume	121
	B.3	Jump in pressure gradient at the interface due to phase change	123
		B.3.1 Test for the derived expression of jump in pressure gradient for vapor	
		bubble	128
$\mathbf{C}$	Der	ivations for Ghost Fluid Method	130
	C.1	Ghost values related to an interfacial face owned by liquid cell	132
	C.2	Ghost values related to an interfacial face owned by vapor cell	136
	C.3	Interpolated values at interfacial face	138
	C4	Gradient calculations at interfacial face	139

# List of Figures

2.1	Comparison between CVSI and experimental data sets for cases described in	
	table 2.1 along with mean error values	23
2.2	Transient variation of individual terms in generalized Rayleigh-Plesset equa-	
	tion for (a) Case $\#$ 2, (b) Case $\#$ 1, and (c) Case $\#$ 6 from table 2.1. Figure	
	(b) and (c) are provided for reference from the more established thermal and	
	inertial categories of collapse. Entries for all three plots in the legend are in the	
	same order as the order of terms in Eq. (2.23), starting with the acceleration	
	term $(R\ddot{R})$	26
2.3	Transient variation of individual terms in energy jump condition for (a) Case	
	# 2, (b) Case $#$ 1, and (c) Case $#$ 6 from table 2.1. Figure (b) and (c)	
	are provided for reference from the more established thermal and inertial	
	categories of collapse. Entries for all three plots in the legend are in the same	
	order as the order of terms in Eq. (2.10), starting with the latent heat term	
	$(m''h_{res})$	20

2.4	Time histories of terms in the vapor pressure rate of change equation (Eq. (2.20))	
	corresponding to (a) Case $\#$ 2, (b) Case $\#$ 1, and (c) Case $\#$ 6 from table 2.1.	
	The rate of change of vapor pressure is given by $[1/\gamma~R(t)~dP_V/dt]/[R_o~\Delta P^*/t_{ref}]$	,
	the heat transfer by $[(1-1/\gamma_V) k_V(\partial T_V/\partial r)_{\Gamma}]/[R_o \Delta P^*/t_{ref}]$ , and pressure	
	work by $[P_V u_{V,\Gamma}]/[R_o \Delta P^*/t_{ref}]$	30
2.5	Time histories for interfacial velocities corresponding to (a) Case $\#$ 2, (b)	
	Case # 1, and (c) Case # 6 from table 2.1	32
2.6	Comparison of transient variation of interface temperature for Case $\#$ 2 of	
	table 3.1 with $\theta_{Therm}$ and $\theta_{Iner}$	39
2.7	Categorization map for spherical vapor bubble collapse based on $B_{sat}$ and $\xi$	
	values. Collapse categories: Thermal $(\circ)$ , intermediate $(+)$ , and inertial $(*)$ .	
	Table 2.1 cases are also marked in the map: Case # 1 - $\star$ ; Case # 2 - $\diamond$ ; Case	
	$\#$ 3 - $\times$ ; Case $\#$ 4 - $\square$ ; Case $\#$ 5 - $\triangle$ ; Case $\#$ 6 - $\nabla$	41
3.1	Comparison between CVSI predictions, analytical solutions, and datasets pre-	
	sented in table 3.1	50
3.2	Comparison between CVSI predictions, HRS results, and analytical solutions	
	pertaining to the cases included in table 3.2	52
3.3	Non-dimensional interface temperature (left) and vapor density (right) as a	
	function of time for the cases described in table 3.2. The arrows mark the time	
	period for which HRS results have been reported [54, 90, 93, 94, 96]	53
3.4	Ratio of destabilizing over stabilizing forces $(max(We/Re,Re))$ for the preser-	
	vation of bubble sphericity as function of diameter for water and R113 systems.	60

4.1	Results for Notched Disk Advection	74
4.2	Results for 2-D Vortex Deformation Advection	75
4.3	Evaluation of Pressure Jump from at different grid sizes	78
4.4	Initial setup of the standing capillary wave test	79
4.5	Time variation of kinetic energy in the domain for a standing capillary wave	
	test case	80
4.6	Test cases for bubbles rising in liquid columns of different liquid properties.	
	Experimental pictures on the left $[126]$ and results from $interIsoFoam$ solver	
	on the right	82
4.7	An instantiation of cells tagged as liquid or vapor to be treated as such in the	
	solution of momentum equation. Cell faces shared by a liquid and vapor cell	
	have been highlighted in red and are the interfacial faces, where the changes	
	due to Ghost Fluid Method are directly implemented	90
4.8	An example pair of cells showing them tagged as liquid and vapor, and high-	
	lighting the interfacial face between them	92
4.9	An example computational cell grid, where the green cells represent liquid	
	cells and white cells represent vapor cells. The red highlighted cell boundaries	
	are the interfacial faces. Cells sharing an interfacial face are populated with	
	two velocity values, one corresponding to its original phase and another ghost	
	value	95
4.10	Algorithm for solution of interface advection and momentum equation for	
	two-phase flow with phase change presented in this thesis	101

4.11	Alpha field with $\alpha = 0.5$ contour (in white) for a circle growing purely due to	
	a prescribed mass flux at the interface. Results shown for grid size $64 \times 64$	102
4.12	Circle radius growing purely due to a prescribed mass flux at the interface	103
4.13	Representation of the liquid-vapor system in Stefan Flow	104
4.14	Comparison of phase change solver solutions with analytical values for Stefan	
	flow test case	106
4.15	Spatial pressure and velocity variation capturing sharp changes at the interface	.107
A.1	Bubble radius versus time plot for different levels of grid refinement for liquid	
	temperature equation, Eq. (2.24), with $\zeta=2,s_L=5,s_V=5,{\rm and}n_V=2000.$	115
A.2	Bubble radius versus time plot for different levels of grid refinement for vapor	
	temperature equation, Eq. (2.18), with $\zeta=2,s_L=5,s_V=5,{\rm and}n_L=1000.$	116
A.3	Bubble radius versus time plot for different extent of the liquid domain for	
	Eq. (2.24), with $s_L = 5$ , $s_V = 5$ , $n_L = 100$ , and $n_V = 100$	118
B.1	Generic two-phase volume with interface	120
B.2	Control volume $(\Omega_i)$ that includes an interface between the liquid (blue) and	
	vapor (green) phases. The red dot denotes the center of the control volume	123
C.1	Graphical representation of an interfacial face. In both figures, interface nor-	
	mal $(\mathbf{n}_{\Gamma})$ points from liquid to vapor phase, and face normal $(\mathbf{n}_f)$ faces from	
	the owner cell $(P)$ to neighbor cell $(N)$	131

# List of Tables

2.1	Description of published vapor bubble collapse cases used for validation of	
	the CVSI method. Here, $\psi = 2/(\Delta T_s \Delta P^*) \int_{T_{\infty}}^{T_{sat}(P_{\infty}^{max})} (P_{\infty}^{max} - P_{sat}(T)) dT$ , is	
	used in the evaluation of $B_{eff}$	22
2.2	Non-dimensional form of key variables for bubble dynamics equations	33
3.1	Description of experimental datasets used for validation of the CVSI method.	48
3.2	Description of cases used in HRS studies	51
3.3	Prediction of threshold times for achieving solutions in the heat-transfer-	
	dominated regime and the associated error with respect to the CVSI solution.	58
4.1	Error in calculation of oscillation time period for standing capillary wave	79
4.2	Test cases for bubbles rising in liquid columns of different liquid properties	81
4.3	Thermophysical properties for Stefan Flow	105

# Chapter 1

## Introduction

Bubble dynamics refers to the motion of an enclosed gas-filled entity present inside a liquid phase. Gas inside the bubble can be the vapor phase of the liquid that surrounds the bubble or a non-condensable gas, like air in water. The focus of this study is on the former, pure vapor bubbles. Such bubbles are oftentimes a point of interest in the context of boiling [4–7] or cavitation [8–11] phenomenon. Boiling refers to the process of vapor formation that occurs when liquid is heated beyond its saturation temperature (or boiling point); while cavitation is a term used for vapor formation due to sudden decrease in local pressure below its saturation value (de-pressurization) at the local temperature [12]. These phenomenon are important for several applications [13], such as,

- for heat and mass transfer processes [14, 15] in the power, electronics, and chemical industries,
- in dispersion processes [16, 17] in petroleum industry and atmospheric processes, and
- in surface erosion [18] processes for medical applications and in naval industry.

With such a wide range of applications, understanding the physics of bubbles has remained an active field of research in the past century.

Early research on vapor bubbles mainly relied on experiments [9, 19–31], and theoretical models that were essentially a reduced form of the Navier - Stokes equations [8, 10, 30, 32–40] under strict, simplifying assumptions. It has been well-established that vapor bubbles have a short length scale, and a small lifetime in physical processes, which implies clear limitations for experiments used to study bubble dynamics. Yet, excellent experimental works have provided insightful photographic evidence for bubble growth and collapse under various conditions that allowed for the validation or improvement of existing theoretical models [41]. While experiments have the factor of uncertainty, the theoretical analysis also tends to be impractical for realistic systems due to the departure from sphericity, presence of a multitude of bubbles, presence of multiple species/components, and a wide range of initial thermo-physical conditions. Nonetheless, they have provided a strong fundamental basis related to the governing mechanisms, and the relative importance of various physical factors in the process of bubble growth or collapse.

More recently, with the advancement in computing power, direct numerical simulations (DNS) have gained importance [11, 42–55]. Such analysis employs a solution for the numerically discretized form of the partial differential equations governing the coupled behavior of flow dynamics and energy transfer in a system of vapor bubbles. These methods are referred to as DNS methods with the underlying assumption that all time and length scales associated with the physical process are resolved in these simulations. However, to avoid ambiguity with different simulations, we prefer to refer to these methods as Highly Resolved Simulation methods or HRS methods. While powerful, the development of a robust and stable technique

using this method is not straightforward. Besides, there is a rapid increase in the computational cost for even moderately complex applications. Each mode of research must synergize with another, to provide meaningful insights about any process involving vapor bubbles.

This dissertation provides a numerical and theoretical take on the analysis for two of the most common phenomenon associated with vapor bubbles, namely, bubble growth and collapse. Furthermore, new ideas have been proposed as part of this thesis for the development of a generalized HRS method that can simulate the phenomenon of the phase change (boiling or condensation associated with vapor bubbles). Notably, the methods developed in this dissertation are not specific to any particular application and can be used to study any thermo-physical condition for vapor bubbles or phase change that satisfy the underlying assumptions of the proposed method.

The research work has been divided into three chapters:

- The work in chapter 2 is a detailed analysis of the physics of bubble collapse (Bardia and Trujillo [3]). At first, the existing literature about the physics of bubble dynamics is reviewed. Based on that, a numerical model is developed for a canonical system of single, spherical vapor bubbles from the two-phase momentum and energy equations. This model is then employed to obtain a bubble collapse rate for a range of system conditions. A closer look at the results revealed that certain cases of collapse had useful similar characteristics, and hence, a novel categorization for the process of vapor bubble collapse has been proposed.
- In chapter 3, the same model developed in chapter 2 is employed to study the limitations in existing HRS methods (Bardia and Trujillo [1]). These limitations are associ-

ated with the assumptions used to simplify the complex 3-D, coupled two-phase flow equations. An analytical expression is also proposed to circumvent these limitations.

- The third aspect of this research presented in chapter 4 describes the development of an in-house numerical solver for highly resolved simulations of vapor bubbles. The development focuses on the specific physical process of the phase change (evaporation or condensation), which is a critical surface phenomenon governing the behavior of vapor bubbles. The code has been developed using C++ within the OpenFOAM-v1706+ framework and builds upon the pre-existing two-phase fluid flow solver, *interIsoFoam*. Two key components have been completed and presented as part of this thesis:
  - A scalable and physically accurate tracking of the liquid-vapor interface, which
    deforms under the effect of bulk flow as well as phase change, and
  - A finite-volume Ghost Fluid Method (GFM) implementation to capture pressure gradient, and velocity discontinuities at the liquid-vapor interface arising due to phase change.

The novelty in this method especially stems from the enforcement of a jump in pressure gradient often ignored in older works [54, 56–60] of phase change numerical methods. These modifications have been tested without the solution of an energy equation.

Remaining aspects of the proposed phase change solver related to the temperature equation and evaluation of the rate of phase change will be points of future work as described in chapter 5.

# Chapter 2

An Improved Categorization of Vapor
Bubble Collapse: Explaining the
Coupled Nature of Hydrodynamic
and Thermal Mechanisms

This chapter elaborates on two objectives that were identified to have remained unexplored in the literature related to bubble collapse, namely:

- 1. An in-depth characterization of an intermediate category of vapor bubble collapse.
- 2. A new categorization that accounts for the effect of the transient period for changes in system or far-field conditions.

### 2.1 Literature Review

Vapor bubble collapse occurs either due to an increase in the liquid pressure surrounding the bubble  $(P_{\infty})$  or due to a decrease in the liquid temperature  $(T_{\infty})$  [61]. In one of the early works on bubble collapse, Florschuetz and Chao [20] showed that the severity or nature of bubble collapse is primarily governed by (i) the magnitude of liquid inertia or inertial mechanism and (ii) the rate of interfacial heat transfer or thermal mechanism. They characterized the relative importance of these two mechanisms by defining a non-dimensional parameter called  $B_{eff}$ . Physically,  $B_{eff}$  can be interpreted as a ratio of the time taken by a bubble to collapse completely in a purely heat-transfer controlled and a purely liquid inertia controlled process. Mathematically,  $B_{eff}$  is given by

$$B_{eff} = \psi^2 \left( \frac{\rho_L C_{p,L} \Delta T_s}{\overline{\rho_V} h_{LV}} \right)^2 \frac{\alpha_L}{R_o} \sqrt{\frac{\rho_L}{\Delta P^*}}, \tag{2.1}$$

where subscript L denotes liquid, and V denotes vapor. The variable  $\psi$  is a measure of the non-linearity in the saturation Pressure-Temperature curve of a real fluid, and  $\overline{\rho_V}$  is the average vapor density of the bubble during the collapse process. The latent heat, liquid density, specific heat, and thermal diffusivity are respectively given by  $h_{LV}$ ,  $\rho_L$ ,  $C_{p,L}$ ,  $\alpha_L$ , and  $R_o$  is the initial bubble radius. Furthermore,

$$\Delta T_s = T_{sat} \left( P_{\infty}^{max} \right) - T_{\infty}, \tag{2.2}$$

$$\Delta P^* = P_{\infty}^{max} - P_{sat}(T_{\infty}), \qquad (2.3)$$

where  $\Delta T_s$  refers to the degree of liquid temperature sub-cooling, and  $\Delta P^*$  refers to the maximum theoretical pressure difference. Subscripts sat and  $\infty$  represent saturated values and far-field system conditions, while the superscript max refers to the maximum system pressure.

Depending on the magnitude of  $B_{eff}$ , Florschuetz and Chao [20] proposed three categories of collapse:

$$B_{eff} < 0.05$$
, Thermal Collapse 
$$0.05 < B_{eff} < 10$$
, Intermediate Collapse 
$$B_{eff} > 10$$
, Inertial Collapse. 
$$(2.4)$$

A fundamental limitation of this categorization was that these distinctive values were proposed only for systems where the collapse was initiated by a sudden, step change in system pressure. But in any practical system, it takes a finite amount of time to increase the pressure of the surrounding liquid to the desired level.

Disregarding this limitation for the moment, Florschuetz and Chao [20] showed that in the limit as  $B_{eff} \to 0$ , the process is initiated by a small pressure difference resulting in a slow collapse, which is governed by a thermal mechanism [41] and is often described as thermal collapse. In such a case, the pressure inside the bubble increases almost instantaneously with the system pressure, maintaining a mechanical equilibrium at the bubble surface. It implies that the temperature of the saturated vapor near the interface  $(T_{sat}(P_V(t)))$  increases, while liquid away from the bubble remains sub-cooled at the far-field temperature,  $T_{\infty}$ . The subsequent development of a thermal boundary layer in the liquid phase and condensation

at the bubble surface drive the bubble collapse. Due to the importance of heat transfer for such cases, the evolution of liquid temperature as a function of space and time for the moving bubble interface has been the focus of studies in the past [33, 62, 63]. Other works have studied the effect of buoyancy [23, 31, 64] because, due to the longer lifetime of such bubbles, an appreciable bulk motion may be observed.

For  $B_{eff} \gg \mathcal{O}$  (10), the process is initiated by a large difference between the bubble pressure and far-field liquid pressure  $(P_{\infty}(t))$  producing pronounced inward movement of the surrounding liquid, and hence, the term liquid inertia collapse [8, 65]. For such cases, the collapse occurs very rapidly and the bubble pressure remains close to its initial value,  $P_{V,o}$ , for nearly the entire process. Correspondingly, the value of the vapor temperature remains nearly unchanged. Hence, only a small temperature difference persists between the bubble and far-field liquid temperature separated by an almost infinitesimal boundary layer. Due to the minute dimensions of this layer, the temperature gradient is sufficiently strong to balance the heat released due to condensation.

The third, intermediate category of collapse is governed by both liquid inertia and heat transfer and compared to the former two regimes has received much less attention. Unlike thermal and inertial cases, no simplifying relations can be made regarding the vapor pressure or temperature and the coupling of both inertial and heat transfer augments significantly the complexity of the phenomenon. For instance, the bulk motion of vapor has been suggested [20] as being important for the intermediate regime, which is commonly ignored in the analysis of thermal and inertial collapse. However, a review of the literature shows that this vapor side analysis for the intermediate collapse case is yet to be done. Furthermore, only a limited number of experimental studies [28, 66, 67] have presented bubble radius and liquid pressure

data for vapor bubble collapse under conditions that correspond with  $0.05 < B_{eff} < 10$ . Even within these works, the key differences between intermediate collapse from the more established thermal and inertial collapse are not analyzed.

Interestingly, intermediate bubble collapse behavior is important for a growing number of studies on bubble condensation in nucleate boiling at high sub-coolings [28, 68–70], and in the generation of micro-bubbles as a result of the collapse of a larger bubble [71–73] in heat exchangers. System conditions reported for these applications in the literature are typically in the range of 10 - 50 K sub-cooling at 1 atm pressure for water, which corresponds to  $0.04 < B_{eff} < 3.0$  for an initial bubble size of 1 mm, which places these studies within the intermediate category.

Another salient aspect of bubble collapse, which is often ignored, is the rate of change in far-field system pressure or temperature (system level metrics are represented by  $\infty$  subscript) that cause the collapse to occur [20]. While the finite rate of pressure increase has been reported in many previous works [20, 28, 29, 48], its effect on the collapse dynamics has not been studied. Only the total magnitude of the pressure change is considered, which may not even be realized if the collapse is faster than the system transient period. This can modify the behavior of the collapse process, which may result in a deviation from the regime characterization presented in Eq. 2.4, which is precisely what is found from the results presented later in this chapter.

### 2.2 Description of the Collapse Study

At first, we systematically delineate the differences in the dynamics of an intermediate collapse from the well established thermal and inertial cases. Moreover, the role of vapor velocity, often overlooked for collapse analysis, is investigated for intermediate systems. This description lays the foundation for a new generalized bubble collapse categorization, which is an extension of the work of Florschuetz and Chao [20]. Again in their work, summarized by Eq. (2.4), the collapse processes were initiated by a step change in pressure, i.e. having a Heaviside character in time. In the present study, we include the finite rate of rising in system pressure instead of an instantaneous change.

In §(2.3), the set of governing equations for bubble dynamics is presented. The numerical method used to solve this system of equations is described in §(2.3.2) followed by its validation against experimental data. In §(2.4), a typical case belonging to the intermediate category of collapse is analyzed using the transient behavior of individual terms in the Rayleigh-Plesset equation and energy balance at the interface. Comparison of vapor velocity magnitude against the rate of collapse is also shown in §(2.4.1). The discussion is facilitated with contrasting plots from the more established [20, 48, 62, 74] thermal and inertial regimes of collapse. A generalized categorization of the collapse process is mathematically proposed in §(2.5), which is subsequently supported by over 550 simulations to create a generalized categorization map. Finally, the key details of this chapter are summarized in §(2.6).

# 2.3 Compressible Vapor Saturated Interface (CVSI) Solution for Bubble Collapse

In this section, we present a spherically-symmetric model for a single vapor bubble surrounded by a homogeneous, pressurized liquid phase. Under spherical symmetry, the single phase governing equations for mass, momentum, and energy are respectively,

$$\frac{\partial \rho}{\partial t} + \frac{1}{r^2} \frac{\partial \left(\rho u r^2\right)}{\partial r} = 0, \tag{2.5}$$

$$\rho\left(\frac{\partial u}{\partial t} + u\frac{\partial u}{\partial r}\right) = -\frac{\partial P}{\partial r} + \left(\frac{4\mu}{3} + \kappa\right)\frac{\partial}{\partial r}\left(\frac{1}{r^2}\frac{\partial(r^2u)}{\partial r}\right),\tag{2.6}$$

$$\rho\left(\frac{\partial e}{\partial t} + u\frac{\partial e}{\partial r}\right) = -P\left(\frac{1}{r^2}\frac{\partial\left(r^2u\right)}{\partial r}\right) - \frac{1}{r^2}\frac{\partial\left(k\left(\frac{\partial T}{\partial r}\right)r^2\right)}{\partial r} + \Phi,\tag{2.7}$$

where  $\rho$ , u, P,  $\mu$ ,  $\kappa$ , e, k, and  $\Phi$  represent the density, radial flow velocity, pressure, dynamic viscosity, bulk viscosity, internal energy, thermal conductivity, and viscous dissipation, respectively.

In addition, the interfacial mass, momentum, and energy transfer are given by

$$\dot{m}'' = \rho_L \left( \dot{R} - u_{L,\Gamma} \right) = \rho_V \left( \dot{R} - u_{V,\Gamma} \right), \tag{2.8}$$

$$(P_V - P_L)_{\Gamma} = \frac{2\sigma}{R} - \dot{m}'' (u_L - u_V)_{\Gamma} + \frac{4\mu_V}{3} \left( \frac{\partial u_V}{\partial r} - \frac{u_V}{r} \right)_{\Gamma} - \frac{4\mu_L}{3} \left( \frac{\partial u_L}{\partial r} - \frac{u_L}{r} \right)_{\Gamma}$$
(2.9)  
+  $\kappa_V \left( \frac{1}{r^2} \frac{\partial (r^2 u_V)}{\partial r} \right)_{\Gamma} - \kappa_L \left( \frac{1}{r^2} \frac{\partial (r^2 u_L)}{\partial r} \right)_{\Gamma},$  and

$$\dot{m}'' h_{LV} = k_L \left(\frac{\partial T_L}{\partial r}\right)_{\Gamma} - k_V \left(\frac{\partial T_V}{\partial r}\right)_{\Gamma}, \qquad (2.10)$$

where subscript  $\Gamma$  denotes the value of a property at the interface. The variable T stands for temperature,  $\dot{m}''$ , and  $\sigma$  represent respectively mass flux due to phase change, and surface tension. Quantities that are dotted reflect temporal derivative; for instance, the interface velocity is written as,

$$\dot{R} = \frac{\mathrm{d}R}{\mathrm{d}t}.\tag{2.11}$$

The CVSI method bears various similarities with other past approaches [42, 48, 74, 75], but the solution procedure has some unique characteristics described in §(2.3.2). Also, all fluid properties used in the method for various calculations are obtained from the Engineering Equation Solver [76].

### 2.3.1 Description of the Physical System & the CVSI Model

The general system studied here consists of a vapor bubble with an initial radius,  $R(t = 0) = R_o$ , surrounded by a liquid domain having a maximum radial extent of  $r_{\infty}$ . Initially, the bubble interior is at thermal equilibrium with the liquid phase, such that

$$T(r \in [0, r_{\infty}], t = 0) = T_{\infty},$$
 (2.12)

where r=0 represents the bubble center location. The far-field location,  $r_{\infty}$  is sufficiently removed from the bubble interface such that it does not affect the observed dynamics of bubble collapse. The pressure inside the bubble corresponds to its saturated value given by

$$P_V(r \in [0, R_o], t = 0) = P_{V,o} = P_{sat}(T_\infty), \tag{2.13}$$

where subscript o refers to the initial value of a variable. Initially, the bubble is also at a mechanical equilibrium with the surrounding liquid, hence, the system pressure is given by,

$$P_{\infty}(t=0) = P_{sat}(T_{\infty}), \qquad (2.14)$$

which is the same as Eq. (2.13). It can be shown that the capillary pressure difference due to surface tension can be ignored for an initially large bubble.

The collapse of a bubble is triggered by increasing the system pressure [20, 28, 29, 77].

Here, the rate of increase is given by,

$$\frac{\mathrm{d}P_{\infty}}{\mathrm{d}t} = \begin{cases}
\frac{P_{\infty}^{max} - P_{sat}(T_{\infty})}{t_{rise}} & 0 \le t \le t_{rise} \\
0 & t > t_{rise},
\end{cases}$$
(2.15)

creating a far field pressure that rises linearly with time to  $P_{\infty}^{max}$  over a finite period,  $t_{rise}$ .

Consequently, the far-field pressure can be expressed as,

$$P_{\infty}(t) = P_{sat}(T_{\infty}) + \int_{0}^{t} \left(\frac{\mathrm{d}P_{\infty}}{\mathrm{d}t}\right) dt = min\left[P_{\infty}^{max}, P_{sat}(T_{\infty}) + \frac{\Delta P^{*}}{t_{rise}}t\right]. \tag{2.16}$$

The assumption of a linear increase in system pressure is consistent with the experimental details of two previous studies [20, 29], which reported a linearly increasing system pressure. Both these studies are used in this work to validate the numerical solution for bubble collapse in  $\S(2.3.3)$ . Consistent with this behavior, Eq. (2.16) is used to describe the system pressure,  $P_{\infty}(t)$ , for all bubble collapse cases described in this study.

For the bubble interior, the vapor phase is assumed to follow the ideal gas equation of state. Separate calculations, where the vapor phase was treated as a Van-der-Waals gas and a uniform bubble temperature (not included here for the sake of brevity) were done to assess this assumption. The use of a more elaborate equation of state had no perceivable effect on the bubble radius time histories. Also, vapor thermal conductivity and specific heat, are assumed to be constant as their variation with temperature has a negligible effect on bubble collapse behavior. An important assumption regarding the vapor phase pertains to the consideration of a uniform pressure inside the bubble. This assumption was analyzed

in a previous numerical study on bubble collapse [48] by calculating the radial variation of vapor pressure within the bubble interior. The uniform pressure approximation was found to hold quite well even for very high interface speed  $(\dot{R})$  that were realized close to the rebound stage of an inertial collapse in that study. Pressure changes at the interface are propagated through the bubble volume with the speed of sound  $(c_V)$ , but even the maximum interface speed associated with the collapse calculations performed in this work is comparatively much smaller in magnitude than  $c_V$  (Mach Number,  $M_V(t) = \dot{R}(t)/c_V(t) = \dot{R}(t)/\sqrt{\gamma_V R_V T_{V,\Gamma}(t)} < 0.3$ ).

Under the above conditions, a homo-baric model for a spherical vapor bubble is presented below. This model has been previously used in the literature [48, 75, 78, 79] to study inertial or thermal cases of collapse. From the continuity and energy equations along with the ideal gas equation of state, an expression for vapor velocity and evolution for vapor temperature is obtained, namely,

$$u_V(r,t) = \frac{1}{P_V} \left( 1 - \frac{1}{\gamma_V} \right) k_V \left( \frac{\partial T_V}{\partial r} \right) - \frac{r}{3\gamma_V P_V} \frac{\mathrm{d}P_V}{\mathrm{d}t}, \quad \text{and} \quad (2.17)$$

$$\rho_V C_{pV} \left( \frac{\partial T_V}{\partial t} + u_V \frac{\partial T_V}{\partial r} \right) = \frac{1}{r^2} \frac{\partial}{\partial r} \left( r^2 k_V \frac{\partial T_V}{\partial r} \right) + \frac{\mathrm{d}P_V}{\mathrm{d}t}. \tag{2.18}$$

Here,  $\gamma_V$  stands for the ratio of specific heats for vapor, and  $C_p$  is specific heat at constant pressure. The vapor properties of  $\gamma_V$  and  $C_{pV}$  are assumed to be constants as their variation was found to be unimportant for the working conditions used in the study. Thermal conductivity of vapor  $k_V$  is evaluated as a function of interface temperature  $T_{\Gamma}(t)$ . Using the

interfacial jump condition for mass balance given by

$$u_{V,\Gamma} = \dot{R} - \frac{\dot{m}''}{\rho_V},\tag{2.19}$$

the boundary condition at r = R(t) for vapor velocity (Eq. 2.17) yields an expression for vapor pressure,

$$\frac{R}{3\gamma_V}\frac{\mathrm{d}P_V}{\mathrm{d}t} = \left(1 - \frac{1}{\gamma_V}\right)k_V\left(\frac{\partial T_V}{\partial r}\right)_{\Gamma} - P_V u_{V,\Gamma}.\tag{2.20}$$

The ideal gas equation of state is employed to obtain density of vapor phase as,

$$\rho_V(r,t) = \frac{P_V(t)}{R_V T_V(r,t)},$$
(2.21)

where  $R_V$  is the gas constant of the vapor phase.

On the liquid side, As compressibility effects are unimportant for the relevant working conditions the continuity equation is simply  $\nabla \cdot u_L = 0$ . It is integrated along the radial coordinate, and the mass jump condition given by Eq. (2.8) is employed to yield the equation

$$u_L(r,t) = \frac{R^2}{r^2} \left( \dot{R} - \frac{\dot{m}''}{\rho_L} \right). \tag{2.22}$$

This expression is substituted in the radially-integrated liquid-phase momentum equation (Eq. (2.6)), where the viscous contribution cancels due to incompressibility. The resulting expression is further reduced by substituting liquid pressure at the interface from the momentum jump condition (Eq. (2.9)) and by neglecting the bulk viscosity contribution from

the vapor phase. This yields

$$\underbrace{R\ddot{R}}_{\text{Acceleration Term}} = \underbrace{\frac{P_V(t) - P_{\infty}}{\rho_L}}_{\text{Pressure Term}} \underbrace{-\frac{3}{2}\dot{R}^2}_{\text{Inertia Term}} \underbrace{-\frac{2\sigma}{R\rho_L}}_{\text{Surface Tension Term}} \underbrace{-\frac{4\nu_L}{R}\left(\dot{R} - \frac{\dot{m}''}{\rho_L}\right)}_{\text{Viscosity Term}} \underbrace{+\frac{\dot{m}''}{\rho_L}\dot{R}}_{\text{Mass Flux Term}} - \underbrace{\frac{4\nu_L}{R}\left(\dot{R} - \frac{\dot{m}''}{\rho_L}\right)}_{\text{Viscosity Term}} \underbrace{-\frac{\dot{m}''}{\rho_L}\dot{R}}_{\text{Mass Flux Term}} - \underbrace{\frac{\dot{m}''}{\rho_L}\dot{R}}_{\text{Mass Flux Term}} - \underbrace{\frac{\dot$$

Here  $\nu$  is the kinematic viscosity of the fluid. Last three terms in Eq. (2.23) are associated with mass flux due to phase change, which are often ignored in the common uses of the Rayleigh-Plesset equation due to their small magnitude. These terms will be referred to as Mass flux term - 1, 2 and 3, respectively in the subsequent discussion.

The remaining unknown variable on the liquid side of the bubble surface is temperature, which is evaluated from the solution of the liquid energy equation,

$$\rho_L \left( \frac{\partial \left( C_{pL} T_L \right)}{\partial t} + C_{pL} \frac{1}{r^2} \frac{\partial \left( r^2 T_L u_L \right)}{\partial r} \right) = k_L \frac{1}{r^2} \frac{\partial}{\partial r} \left( r^2 \frac{\partial T_L}{\partial r} \right), \tag{2.24}$$

where liquid thermal conductivity  $(k_L)$ , and specific heat  $(C_{pL})$  are evaluated at a film temperature, defined as  $T_{film} = (T_{\Gamma}(t) + T_{\infty})/2$ .

Finally, at the interface, mass flux due to phase change is governed by the energy balance [60] given by Eq. (2.10) rewritten here with a brief description of individual terms,

$$\underbrace{\dot{m}'' h_{LV}}_{\text{Latent Heat Term}} = \underbrace{k_L \left(\frac{\partial T_L}{\partial r}\right)_{\Gamma}}_{\text{Liquid Heat Transfer Term}} - \underbrace{k_V \left(\frac{\partial T_V}{\partial r}\right)_{\Gamma}}_{\text{Vapor Heat Transfer Term}}.$$
(2.25)

Similar to the interface property of surface tension, latent heat is also evaluated as a function of interface temperature,  $T_{\Gamma}(t)$ . In this complete description of bubble dynamics, the key governing equations are Eq. (2.23) and Eq. (2.10), which are used to evaluate the rate of collapse, and the rate of condensation, respectively.

### 2.3.2 Numerical Solution

Our model consists of two partial differential equations for vapor temperature  $(T_V(r,t))$  Eq. 2.18) and liquid temperature  $(T_L(r,t))$  Eq. 2.24), three ordinary differential equations, for vapor pressure  $(P_V(t))$  Eq. 2.20), bubble radius (R(t)) Eq. 2.11), and interface speed (R) Eq. 2.23), and three algebraic equations for vapor velocity  $(u_V(r,t))$  Eq. 2.17), vapor density  $(\rho_V(r,t))$  Eq. 2.21), and mass flux due to phase change (m'''(t)) Eq. 2.25), respectively. The main difference in the CVSI model with respect to previous collapse studies [20, 48, 80] lies in the solution methodology employed to solve the two PDE's and the use of an adaptive time stepping scheme that significantly reduces the computational burden, which is necessary for the extensive categorization analysis done in §(2.5). Note that for the current focus, collapse calculations are not performed to the extent when bubble radius approaches the value of zero, where the above-mentioned assumptions may prove to be limiting.

The initial conditions for this system of equations are given by

$$R(t=0) = R_o,$$
 (2.26a)  $P_V(t=0) = P_{sat}(T_\infty),$  (2.27a)

$$\dot{R}(t=0) = 0,$$
 (2.26b)  $u_V(r \in [0, R_o], t = 0) = 0,$  (2.27b)

$$\dot{m}''(t=0) = 0,$$
 (2.26c)  $T_V(r \in [0, R_o], t=0) = T_{\infty},$  (2.27c)

$$T_L(r \in (R_o, r_\infty), t = 0) = T_\infty, \text{ and } \rho_V(r \in [0, R_o], t = 0) = \frac{P_{sat}(T_\infty)}{R_V T_\infty}.$$

$$(2.26d)$$

The relevant boundary conditions are

$$\frac{\partial T_V}{\partial r}(r=0,t) = 0,$$
 (2.28a)  $T_L(R(t),t) = T_{\Gamma}(t),$  (2.29a)

$$T_V(R(t), t) = T_{\Gamma}(t), \text{ and } (2.28b)$$
  $T_L(r_{\infty}, t) = T_{\infty},$  (2.29b)

where  $T_{\Gamma}(t)$  is obtained from the Clausius-Clapeyron equation, namely

$$\frac{\mathrm{d}P_V(t)}{\mathrm{d}T_\Gamma(t)} = \frac{\rho_V(R(t), t)h_{LV}(T_\Gamma(t))}{T_\Gamma(t)},\tag{2.30}$$

under the stipulation that the interface remains at thermodynamic equilibrium. The expression on the left-hand-side (LHS) of the equation is approximated numerically by the solution of  $P_V$  and  $T_{\Gamma}$ . Above conditions reflect a system for bubble collapse, but it is instructive to point out that the CVSI solution can also be used to study bubble growth by making relevant changes to initial and boundary conditions, as is done in chapter 3. The governing equations solved are equally applicable to both bubble collapse or growth.

Liquid temperature field is solved using an Arbitrary Lagrangian-Eulerian (ALE), which

has been modified from the work of Ryddner and Trujillo [2], where it was used for droplet evaporation. The liquid domain,  $\Omega_L$ , spans from the bubble radius, R(t), to an external radius,  $r_{\infty}(t)$ , and is discretized into spherical shell volumes, which are temporal displaced at some arbitrary velocity. The radial location of these shell boundaries is given by

$$r_{L,i} = R(t) + R_o \times (\zeta - 1) \left( \frac{e^{\left(\frac{i-1}{n_L} \times s_L\right)} - 1}{e^{s_L} - 1} \right), \quad i \in \{1, 2, 3, ..., n_L + 1\}.$$
 (2.31)

In this expression,  $n_L$  is the total number of spherical shell volumes and i=1 corresponds to the innermost shell whose internal boundary coincides with the bubble surface. As noted previously, the extent of the liquid domain is given by  $r_{\infty} = R(t) + R_o \times (\zeta - 1)$ , where  $\zeta$  determines the extent of the liquid domain and  $s_L$  is a parameter that is employed to locally refine the grid near R(t). Using  $s_L > 0$ , these shells are clustered around the bubble surface for adequate resolution of the thermal boundary layer. The rate of displacement of each of these element boundaries is then given by

$$\dot{r}_{j}^{n} = \dot{R}(t^{n}) \left( 1 + (\xi - 1) \left( \frac{e^{\lambda \frac{j}{M}} - 1}{e^{\lambda} - 1} \right) \right), \quad \text{where } j = 0, 1, 2, ..., (M - 1).$$
 (2.32)

Inside the bubble, the vapor temperature equation is solved using a finite difference approach used by [78] but with a non-uniform grid spacing. The radial coordinates are transformed to a non-dimensional form,  $\eta = r/R(t)$ . The non-uniform spatial discretization is again leveraged to improve the resolution of the thermal boundary layer close to the bubble

surface. The locations of the boundaries of the computational volumes are given by

$$r_{V,j} = R(t) \times \left(\frac{e^{\left(-\frac{j-1}{n_V} \times s_V\right)} - 1}{e^{-s_V} - 1}\right), \quad j \in \{1, 2, 3, ..., n_V + 1, \}$$
 (2.33)

where  $n_V$  is the number of nodes in the vapor phase, and  $j = n_V + 1$  corresponds to the bubble surface. Similar to the parameter  $s_L$  in Eq. (2.31),  $s_V$  sets the density of points close to the interface inside the bubble.

Besides the liquid and vapor temperature equations, the remaining differential equations are integrated using the Euler scheme, and the algebraic equations are employed throughout the solution. The entire system of equations is solved using an adaptive time stepping scheme, where the time step size is determined such that 0.1 < CFL < 0.4, where

$$CFL = \frac{\dot{R} \times \Delta t}{\min\left(\min\left(\Delta r_{L,i}\right), \min\left(\Delta r_{V,i}\right)\right)}, \quad and \quad (2.34)$$

$$\Delta r_{L,i} = r_{L,i+1} - r_{L,i}$$
 ;  $\Delta r_{V,j} = r_{V,j+1} - r_{V,j}$ , (2.35)

for  $i \in \{1, 2, 3, ..., n_L\}$  and  $j \in \{1, 2, 3, ..., n_V\}$ . The time step size is  $\Delta t$ , thickness of  $i^{th}$  shell in liquid domain is  $\Delta r_{L,i}$  and the distance between consecutive radial points in the discretized vapor domain is  $\Delta r_{V,j}$ .

In appendix A, a numerical sensitivity analysis is reported leading to the conclusion that with parameters  $\zeta = 2$ ,  $s_L = 5$ ,  $s_V = 5$ ,  $n_L = 100$ , and  $n_V = 100$ , grid convergent results are obtained. Hence, in the bubble collapse calculations, these are the numerical parameters that are employed.

#### 2.3.3 Validation of the CVSI Model

To validate the CVSI model, six different bubble collapse cases are considered. The system conditions for these cases are given in table 2.1 and are obtained from previously published experimental studies. To quantify the degree of agreement, the following error metric is employed

$$E_{mean} = \frac{1}{N_{ref}} \sum_{i=1}^{N_{ref}} \left| \frac{R_{CVSI}(t_i)}{R_o} - \frac{R_{ref}(t_i)}{R_o} \right|, \qquad i \in \{1, 2, 3, ..., N_{ref}, \}$$
 (2.36)

where  $R_{ref}(t_i)$  is the bubble radii obtained from the reference study,  $N_{ref}$  is the number of data points obtained from those studies, and  $R_{CVSI}(t_i)$  are the corresponding bubble radius computed from the CVSI model.

Case # and	Fluid	Subcooling	System pressure	Pressure rise time	Initial radius	$\psi$	$B_{eff}$	$t_{ref}$	Mean error
Ref.		(in K), $\Delta T_s$	(in atm), $P_{\infty}^{max}$	(in ms), $t_{rise}$	(in mm), $R_o$		Eq. $(2.1)$	(in ms)	$E_{mean}$
1 [20]	Water	12.20	0.987	2.50	3.66	1.04	0.02	.53	7.2 %
2 [ <b>28</b> ]	Water	29.80	1.000	0.20	11.80	1.16	0.05	1.4	5.9 %
3 [28]	Water	33.90	1.000	0.20	13.80	1.18	0.06	1.6	5.0 %
4 [28]	Water	39.50	1.000	0.20	12.70	1.22	0.10	1.4	3.0 %
5 [28]	Water	53.40	1.000	0.20	11.80	1.30	0.32	1.2	6.3 %
6 [29]	Water	70.40	0.7025	$1 \times 10^{-6}$	1.00	1.41	27.62	.12	2.2 %

Table 2.1: Description of published vapor bubble collapse cases used for validation of the CVSI method. Here,  $\psi = 2/(\Delta T_s \Delta P^*) \int_{T_\infty}^{T_{sat}(P_\infty^{max})} \left(P_\infty^{max} - P_{sat}(T)\right) dT$ , is used in the evaluation of  $B_{eff}$ .

The range of  $B_{eff}$  values in table 2.1 suggests that the cases considered in this validation span all three categories of collapse. In each plot, the bubble radius is non-dimensionalized using initial bubble radius as a reference, and time is non-dimensionalized using the characteristic time for the inertial effects [20], namely,

$$t_{ref} = R_o \sqrt{\frac{\rho_L}{\Delta P^*}}. (2.37)$$

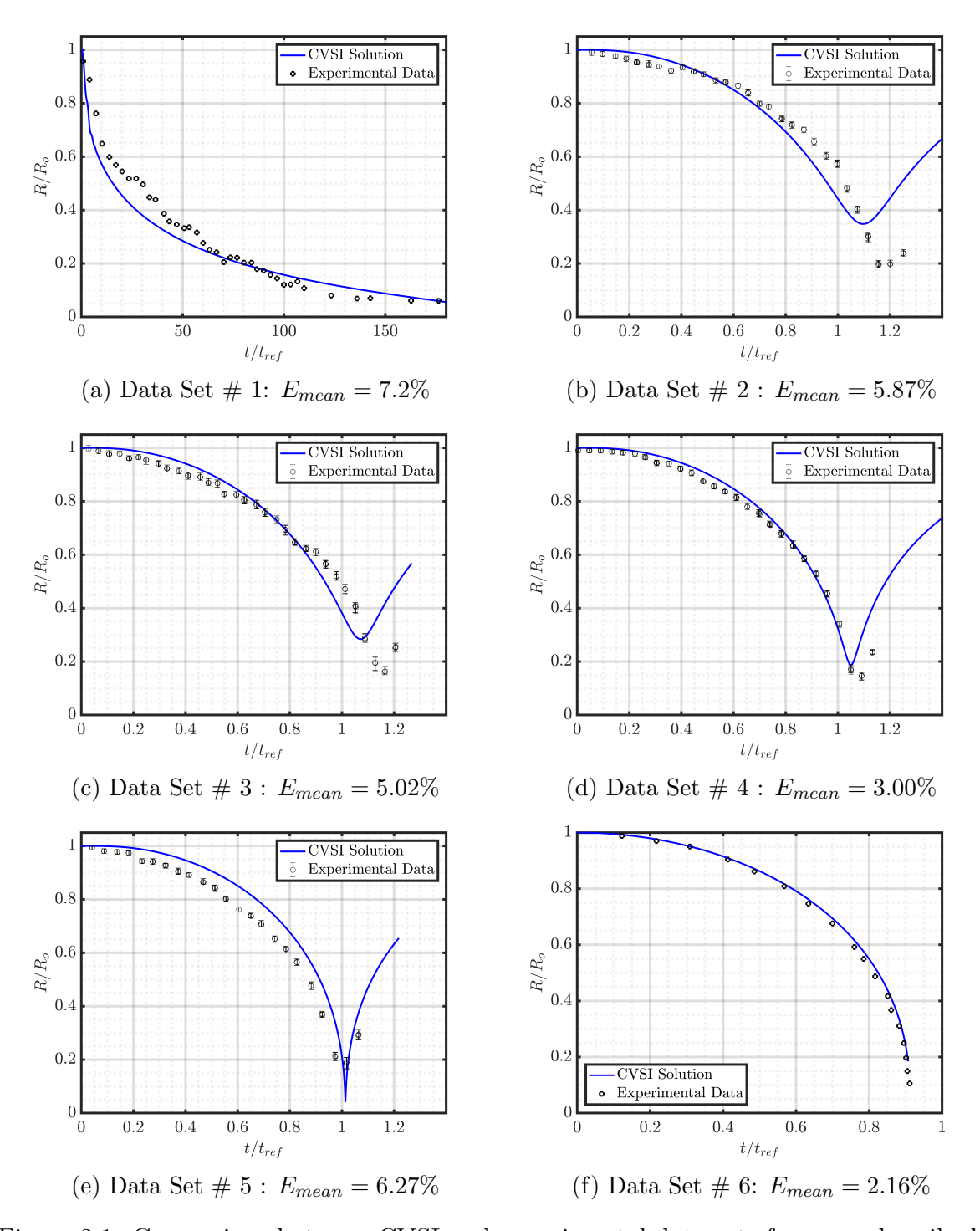


Figure 2.1: Comparison between CVSI and experimental data sets for cases described in table 2.1 along with mean error values.

Results from figure 2.1 show that the CVSI solution matches experimental results for a range of cases for bubble collapse. Case # 1 represents a thermal collapse and its bubble radius trend is shown in figure 2.1a. This collapse has a gradual and decelerating rate of motion as expected for a thermally-dominated process. Experimental data for the following four cases shown in figure 2.1b - figure 2.1e are obtained from Board and Klimpton [28] and pertain to the intermediate category of collapse. All four collapses are captured quite well with most of the error originating from model predictions close to the minimum radius. Finally, for figure 2.1f, the result shows an inertial collapse for which the bubble radius time history from the CVSI method has an excellent agreement with the experimental data. Across all the six cases, the CVSI model predicts the bubble radius with a mean error,  $E_{mean} < 7.5\%$ , where most of the discrepancy occurs when the bubble has reached a smaller size. For the thermal collapse, the reason for the discrepancy may be attributed to the bulk motion of bubble 20, which may occur after an initial time period of acceleration due to buoyant forces. For the intermediate cases, experimental measurements by Board and Klimpton [28] were reported to be affected by the presence of vessel walls close to the bubble, whereas the CVSI model corresponds to a stationary spherical vapor bubble collapse. Notwithstanding, for all six validation cases the error is within a reasonable magnitude.

#### 2.4 Intermediate Bubble Collapse

To analyze the key features of intermediate collapse, Case # 2 described in table 2.1 is employed as a representative case. For all of the following calculations, CVSI model has been employed up to a final time equal to the time required for the bubble to collapse to 5%

of its initial volume. This has been done to strike a balance between the time needed for the dominating characteristics of a collapse to be evident and to avoid working with very small bubble sizes, which are difficult to study in practical systems [20, 28, 41, 61].

At first, a comparison of the time history of the Rayleigh-Plesset terms defined in Eq. (2.23) are presented in figure 2.2, where the intermediate collapse is represented by figure 2.2a. To contrast its characteristics with the more established thermal and inertial regimes [20, 48, 62, 74], the temporal variation of the Rayleigh-Plesset terms for a typical thermal and inertial collapse is also shown in figure 2.2b and figure 2.2c, respectively. The terms are non-dimensionalized using  $R_o^2/t_{ref}^2$ , where  $t_{ref}$  is given by Eq. (2.37). Also, over the entire collapse period shown for the three cases, the dominant terms that contribute to the acceleration of the bubble radius are pressure and inertial terms. Surface tension, viscous, and mass flux terms remain negligible for the entire period.

Before presenting a more detailed description about the intermediate collapse and its unique transient behavior, we would like to note that the oscillation of pressure and acceleration terms for the thermal collapse in figure 2.2b is not an anomaly. It has been observed in previous studies [20, 31, 80, 81] as well. Hao and Prosperetti [81] provide a more detailed explanation for this phenomenon and relate it to the imbalance between the increasing system pressure  $(P_{\infty}(t))$ , and vapor pressurization  $(P_V(t))$  due to a sudden, rapid collapse. This initial transient period for thermal collapse can usually be ignored as those acceleration values are small in magnitude and only last for a small duration in comparison to the overall collapse period.

For the intermediate collapse represented by figure 2.2a, initially the system pressure,  $P_{\infty}(t)$ , increases at a constant rate for a period corresponding to  $t_{rise}$  (introduced in Eq. (2.16)),

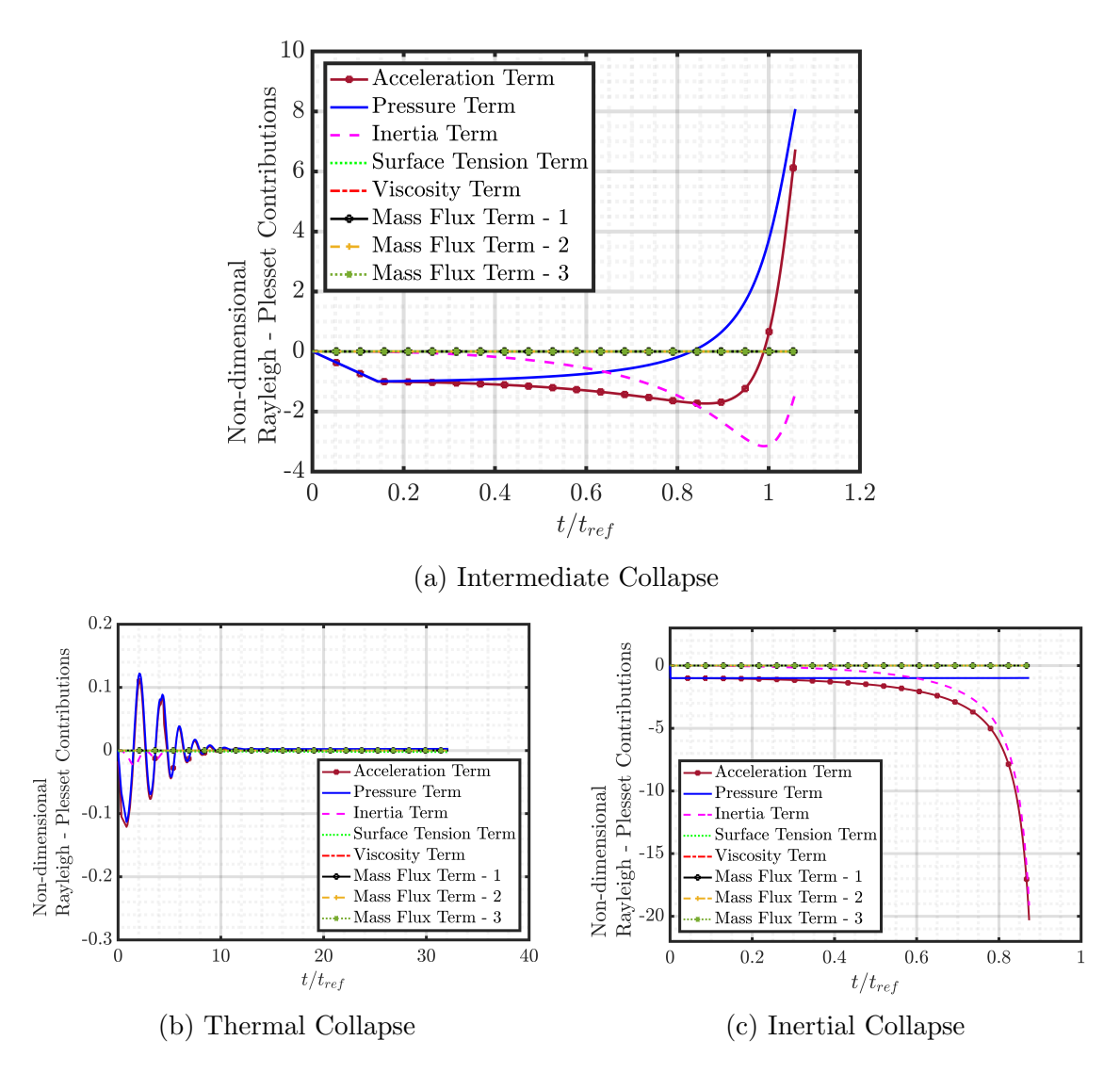


Figure 2.2: Transient variation of individual terms in generalized Rayleigh-Plesset equation for (a) Case # 2, (b) Case # 1, and (c) Case # 6 from table 2.1. Figure (b) and (c) are provided for reference from the more established thermal and inertial categories of collapse. Entries for all three plots in the legend are in the same order as the order of terms in Eq. (2.23), starting with the acceleration term  $(R\ddot{R})$ .

which is depicted by a nearly linear decrease in the pressure term. Due to the negative value of the pressure difference, the bubble begins to collapse. After  $t_{rise}$ , the system pressure  $(P_{\infty}(t > t_{rise}) = P_{\infty}^{max})$  remains constant but the pressure term magnitude decreases due to an increasing vapor pressure  $(P_V)$ . Eventually, vapor pressure inside the bubble becomes larger than the system pressure, which reverses the sign of the pressure term and begins

to act as a decelerating force for bubble collapse. This behavior is unlike a thermal collapse where, after an initial transient of vapor pressure, its magnitude stabilizes at a constant value as shown in figure 2.2b. Also, it is unlike an inertial collapse, where the vapor pressure is known to remain nearly constant at its initial value for most of the collapse period, precisely as found in our calculations shown in figure 2.2c.

The initial acceleration for the intermediate collapse shown in figure 2.2a triggers the manifestation of the inertia term, which always remains negative and promotes the contraction of the bubble. After its initial gradual increase, the magnitude of liquid inertia becomes the dominant term in the Rayleigh-Plesset equation. This dominance is only sustained for a short period after which the collapse begins to decelerate under the influence of a stronger, positive pressure term. Such a time variation of the inertia term is unique to an intermediate collapse. Otherwise, inertia term either remains insignificant for a thermally-dominated collapse as shown in figure 2.2b or it gradually increases and then sustains its dominance in case of an inertially-dominated collapse as shown in figure 2.2c.

With respect to the energy balance at the interface (Eq. 2.10), the time history of each of the terms for the intermediate collapse is shown in figure 2.3a along with similar plots for a thermal, figure 2.3b and inertial collapse, figure 2.3c, for reference. Again, we observe a short time period of initial oscillation of different energy terms for the thermal collapse in figure 2.3b. Similar to the description for figure 2.2b, the pressure imbalance [81] also affects the temperature difference that exists in the liquid phase, causing these oscillations. Barring this short initial transient period, the remaining behavior of thermal collapse is not affected by those oscillations.

The energy terms in all the plots are normalized by  $|k_L \Delta T_s/\sqrt{\alpha_L t_{ref}}|$ , which is a measure

of the liquid heat flux given by the degree of sub-cooling  $(\Delta T_s)$  and a reference boundary layer thickness  $(\sqrt{\alpha_L t_{ref}})$ . Evidently, from figure 2.3, the rate of heat transfer is nearly balanced

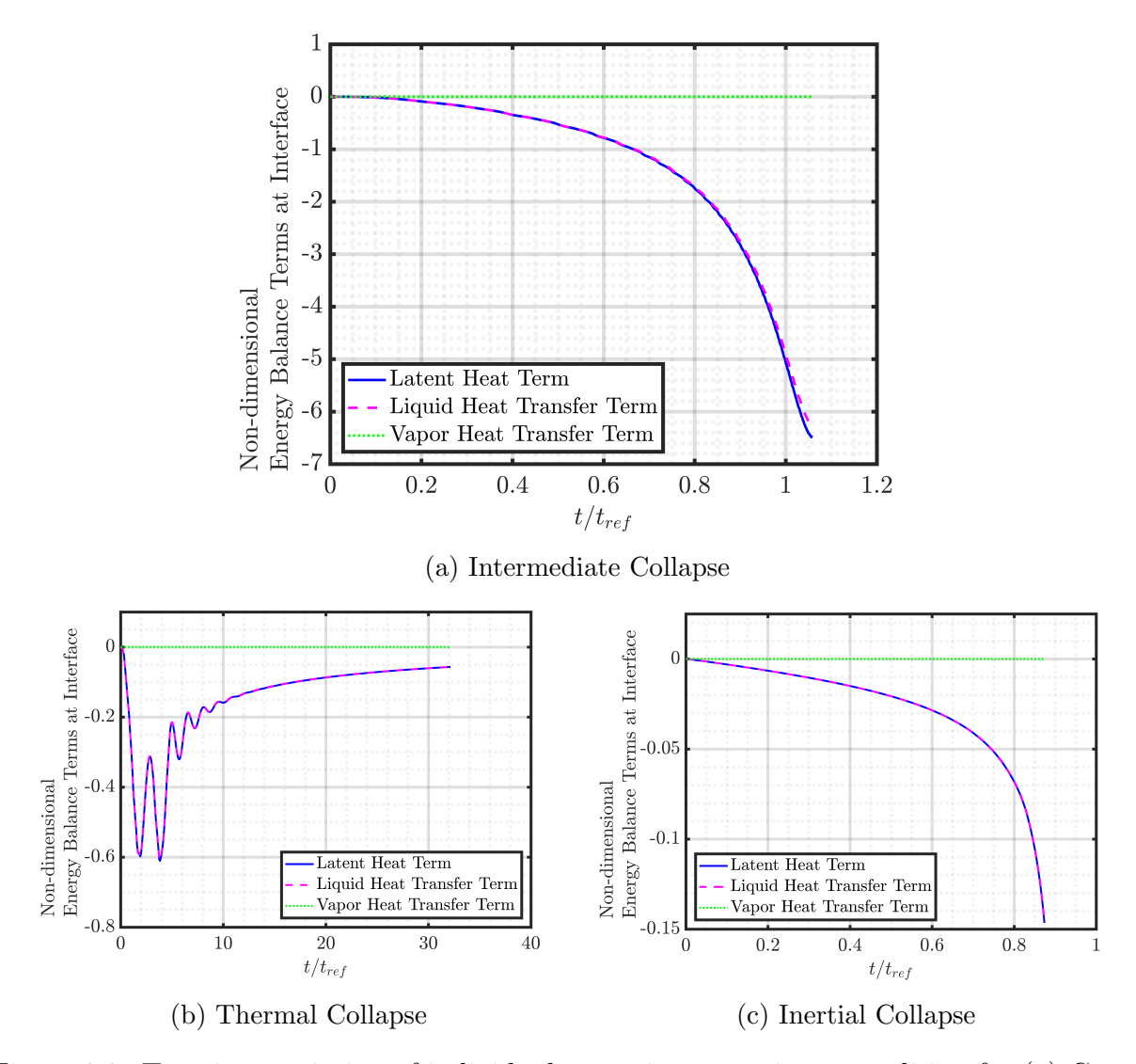


Figure 2.3: Transient variation of individual terms in energy jump condition for (a) Case # 2, (b) Case # 1, and (c) Case # 6 from table 2.1. Figure (b) and (c) are provided for reference from the more established thermal and inertial categories of collapse. Entries for all three plots in the legend are in the same order as the order of terms in Eq. (2.10), starting with the latent heat term  $(\dot{m}''h_{LV})$ .

by the latent heat term for the entire time period for all three categories of collapse. It suggests that heat released during condensation is almost entirely transferred to the liquid phase, while heat transfer in the vapor phase is negligible.

Focusing on the intermediate collapse shown in figure 2.3a, as the collapse unfolds, bubble temperature increases, which results in the initial increase in liquid heat transfer. While the temperature difference between bubble surface and far-field liquid increases, diffusion of heat also leads to the growth of thermal boundary layer thickness ( $\delta_L$ ). These competing factors result in a complex transient system for intermediate collapse, where both these effects are equally important. In comparison, for a thermal collapse, the boundary layer growth is more dominant and the process is characterized by an asymptotically decreasing rate of liquid heat transfer evident from figure 2.3b. On the other hand, the inertial collapse in figure 2.3c shows a similar behavior of energy balance as the intermediate collapse with a continuously increasing rate of liquid heat transfer as well as condensation.

## 2.4.1 Explaining the Different Characteristics of Intermediate Collapse

In the preceding discussion, the main distinctive trait of an intermediate collapse is the continuous variation of vapor pressure and inertia term in the Rayleigh-Plesset equation. Since the pressure term plays a dominant role in the dynamics, we consider the contributing factors to the rate of change of  $P_V$ . These are given in Eq. (2.20) and consist of a heat transfer contribution,  $(1 - 1/\gamma_V) k_V(\partial T_V/\partial r)_{\Gamma}$  and pressure work,  $P_V u_{V,\Gamma}$ .

The time histories of these contributing factors for the intermediate collapse are plotted in figure 2.4a, non-dimensionalized by  $R_o \Delta P^*/t_{ref}$  along with similar plots for a thermal, figure 2.4b and inertial collapse, figure 2.4c, for reference. The reason behind oscillations for thermal collapse in figure 2.4b is the same as described in the discussion for figure 2.2b and

figure 2.3b above.

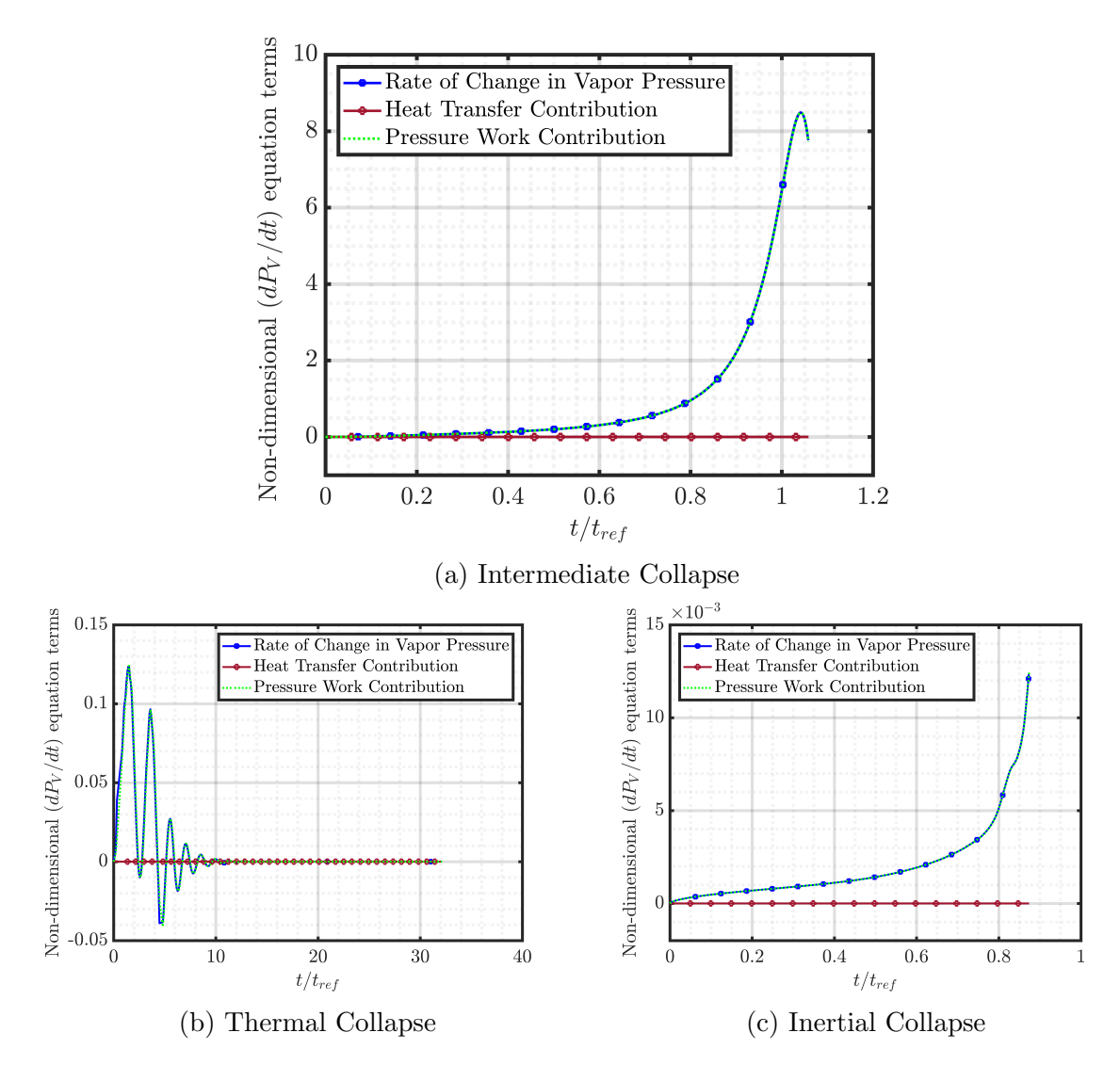


Figure 2.4: Time histories of terms in the vapor pressure rate of change equation (Eq. (2.20)) corresponding to (a) Case # 2, (b) Case # 1, and (c) Case # 6 from table 2.1. The rate of change of vapor pressure is given by  $[1/\gamma R(t) dP_V/dt]/[R_o \Delta P^*/t_{ref}]$ , the heat transfer by  $[(1-1/\gamma_V) k_V(\partial T_V/\partial r)_{\Gamma}]/[R_o \Delta P^*/t_{ref}]$ , and pressure work by  $[P_V u_{V,\Gamma}]/[R_o \Delta P^*/t_{ref}]$ .

Results from figure 2.4 show that any change in vapor pressure is a result of the pressure work contribution with a negligible role from the gas-side heat flux on the interface. The magnitude of pressure work and the resulting pressure variation are significant for the entire collapse period in the intermediate regime as shown in figure 2.4a. In contrast, these

terms remain essentially negligible for a thermal collapse as shown in figure 2.4b. For inertial collapse shown in figure 2.4c the pressure work and change in vapor pressure has an increasing trend, but the values are 3 orders of magnitude lower than what is observed for the intermediate collapse, rendering the pressure variation as insignificant for most of the inertial regime. This is also corroborated from a nearly constant pressure difference term in figure 2.2c, above.

In intermediate collapse, the reason for the importance of pressure work term  $(P_V u_{V, \Gamma})$  can be traced back to the expression for interfacial vapor velocity given by Eq. (4.35b), i.e.  $u_{V, \Gamma} = \dot{R} - \dot{m}''/\rho_V$ . This equation can be interpreted in terms of expressing  $u_{V, \Gamma}$  as an imbalance between the rate of bubble collapse  $(\dot{R})$  and the rate of condensation  $(\dot{m}''/\rho_V)$ . To analyze its magnitude, the time histories of  $\dot{R}$  and  $u_{V, \Gamma}$  for a typical intermediate collapse are plotted in figure 2.5a, non-dimensionalized by  $R_o/t_{ref}$  along with similar plots for thermal (figure 2.5b) and inertial (figure 2.5c) types of bubble collapse.

An inspection of the results in figure 2.5a reveals that the magnitude of the interfacial vapor velocity is of the same order as the speed of the bubble interface for the entire collapse period for an intermediate collapse. This implies that for an intermediate collapse,  $\dot{R}$  is not matched by an equal rate of condensation  $(\dot{m}''/\rho_V)$ . As a result, the contraction of the bubble is additionally balanced by bulk motion of the vapor inside the bubble, i.e.  $u_{V, \Gamma}$ , which contributes to a continuous change in vapor pressure as shown in figure 2.4a. This is in clear contrast with a thermal or inertial collapse [20], where vapor velocity is justifiably ignored as shown by its small magnitude in figure 2.5b and figure 2.5c, which in turn means that  $\dot{R} \cong \dot{m}''/\rho_V$  for those two regimes of collapse.

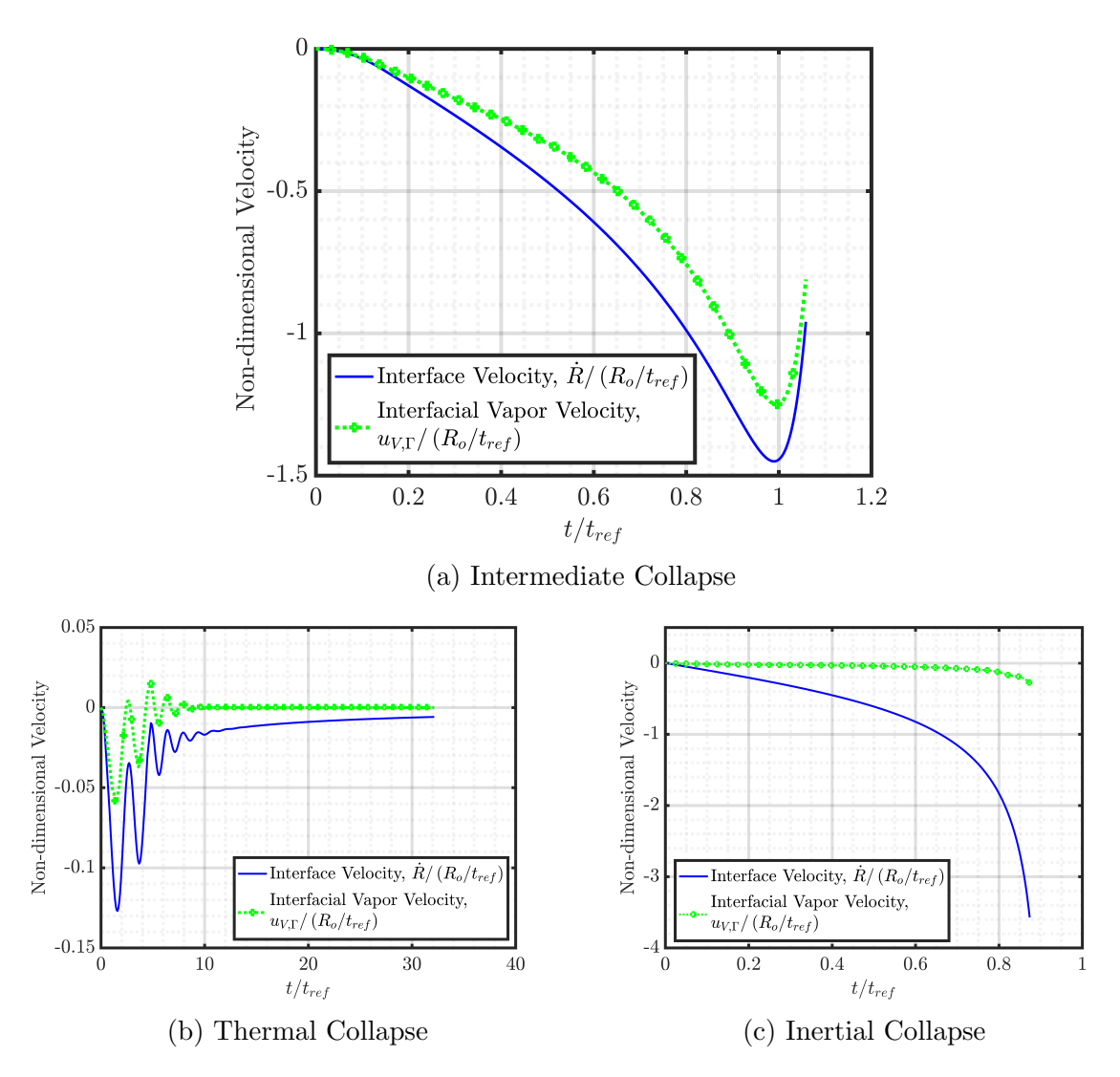


Figure 2.5: Time histories for interfacial velocities corresponding to (a) Case # 2, (b) Case # 1, and (c) Case # 6 from table 2.1.

#### 2.5 Vapor Bubble Collapse Categorization

As mentioned in the introduction, one of the main goals of this study is to define a generalized metric to categorize vapor bubble collapse over a variety of system conditions and working fluids beyond an earlier categorization [20], which was solely based on  $B_{eff}$ . Specifically, collapse is bound to depend on the time taken to change the system pressure given by  $t_{rise}$ , which is ignored in prior work. A detailed description of the significance of  $t_{rise}$  is

given below through a non-dimensional analysis of the generalized Rayleigh-Plesset equation (Eq. (2.23)). To clarify the presentation of results, the definition of the relevant variables are included in table 2.2.

Time, 
$$\tau = \frac{t}{t_{ref}}$$

Bubble radius,  $\gamma(\tau) = \frac{R(\tau)}{R_o}$ 

Radial coordinate,  $\eta = \frac{r - R(t)}{\delta_L}$ 

Liquid thermal boundary layer,  $\delta_L = C_1 \sqrt{\alpha_L t_{ref}}$ 

( $C_1$  is a constant of proportionality)

Temperature,  $\theta(\eta,\tau) = \frac{T(\eta,\tau) - T_{\infty}}{\Delta T_s}$ 

Vapor density,  $\epsilon_V(\tau) = \frac{\rho_V(R(t),t)}{\rho_V^t}$ 

Time Scale Ratio,  $\xi = \frac{R_o}{t_{rise}} \sqrt{\frac{\rho_L}{\Delta P^*}}$ 

Reference vapor density,  $\rho_V^* = \rho_{V,sat} \left(T_{sat} \left(P_{\infty}^{max}\right)\right)$ 

Vapor pressure,  $\pi_V(t) = \frac{P_{\infty}^{max} - P_V(t)}{\Delta P^*}$ 

Vapor pressure,  $\pi_{\infty}(t) = \frac{P_{\infty}^{max} - P_{\infty}(t)}{\Delta P^*}$ 

Latent heat,  $\omega = \frac{h_{LV}}{h_{LV}^*}$ 

Reference latent heat,  $h_{LV}^* = h_{LV} \left(T_{sat} \left(P_{\infty}^{max}\right)\right)$ 

Vapor velocity,  $u_V^*(\eta,\tau) = \frac{u_V(\eta,\tau)}{\dot{R}_{ref}}$ 

Jakob number,  $Ja = \frac{\rho_L C_L \Delta T_s}{\rho_V^* h_{LV}^*}$ 

Categorization Parameter,  $B_{sat} = Ja^2 \frac{\alpha_L}{R_o} \sqrt{\frac{\rho_L}{\Delta P^*}}$ 

Table 2.2: Non-dimensional form of key variables for bubble dynamics equations.

From the results in  $\S(2.4)$ , the dominant terms in the generalized Rayleigh-Plesset equa-

tion are the acceleration, pressure, and inertia terms. Considering these leading order terms, the Rayleigh-Plesset equation is

$$R\ddot{R} + \frac{3}{2}\dot{R}^2 = \frac{P_V(t) - P_\infty(t)}{\rho_L}.$$
 (2.38)

This expression can be manipulated to yield,

$$R\ddot{R} + \frac{3}{2}\dot{R}^2 = \frac{-(P_{\infty}^{max} - P_V(t)) + (P_{\infty}^{max} - P_{\infty}(t))}{\rho_L}.$$
 (2.39)

Using the non-dimensional variables for time, bubble radius, vapor pressure and system pressure defined in table 2.2, this equation can be rewritten in its non-dimensional form as

$$\frac{R_o^2}{t_{ref}^2} \left( \gamma \ddot{\gamma} + \frac{3}{2} \dot{\gamma}^2 \right) = \frac{\Delta P^*}{\rho_L} \left( -\pi_V(\tau) + \frac{P_\infty^{max} - P_\infty(t)}{\Delta P^*} \right). \tag{2.40}$$

From the expression for  $t_{ref}$  defined in Eq. (2.37), the coefficients  $R_o^2/t_{ref}^2$  and  $\Delta P^*/\rho_L$  cancel out. On substituting  $P_{\infty}(t)$  from Eq. (2.16), we obtain

$$\gamma \ddot{\gamma} + \frac{3}{2} \dot{\gamma}^2 = -\pi_V(\tau) + \frac{P_{\infty}^{max} - min\left[P_{\infty}^{max}, P_{sat}\left(T_{\infty}\right) + \frac{\Delta P^*}{t_{rise}}t\right]}{\Delta P^*}.$$
 (2.41)

Combining the  $P_{\infty}^{max}$  and the terms inside the min() function and using the expression for  $\Delta P^* = (P_{\infty}^{max} - P_{sat}(T_{\infty}))$  (defined in Eq. (2.3)), this expression is further reduced to

$$\gamma \ddot{\gamma} + \frac{3}{2} \dot{\gamma}^2 = -\pi_V(\tau) + \frac{max \left[ 0, \ \Delta P^* - t \ \frac{\Delta P^*}{t_{rise}} \right]}{\Delta P^*}. \tag{2.42}$$

Expressing time, t as  $\tau t_{ref}$ , a final equation for the momentum dynamics is obtained, namely

$$\gamma \ddot{\gamma} + \frac{3}{2} \dot{\gamma}^2 = -\pi_V(\tau) + \max[0, 1 - \xi \tau]$$
 where (2.43)

$$\xi = \frac{t_{ref}}{t_{rise}} = \frac{R_o}{t_{rise}} \sqrt{\frac{\rho_L}{\Delta P^*}}.$$
 (2.44)

Specifically, for  $t \leq t_{rise}$ , which may be a large fraction of the total collapse time, the momentum is given by

$$\gamma \ddot{\gamma} + \frac{3}{2} \dot{\gamma}^2 = 1 - \pi_V(\tau) - \frac{t}{t_{rise}},$$
 (2.45)

and for  $t > t_{rise}$ 

$$\gamma \ddot{\gamma} + \frac{3}{2} \dot{\gamma}^2 = -\pi_V(\tau). \tag{2.46}$$

In previous studies on bubble collapse [20, 48, 74], it is tacitly assumed that the system pressure rise occurs extremely fast. In the framework of this analysis, this situation is equivalent to  $t_{rise}$  being very small such that  $\xi \gg 1$ . Consequently, this leads to  $max [1 - \xi \tau, 0] \cong 0$ , and the momentum dynamics reduces to Eq. (2.46). Hence, under the established treatment of momentum in the literature, the role of varying system pressure is absent in the mathematical framework.

To complete the description of the dynamics, the energy jump condition is considered

(Eq. (2.10)) and rewritten here accounting only for the leading order terms. This gives

$$k_L \left(\frac{\partial T_L}{\partial r}\right)_{\Gamma} = \rho_V \left(\dot{R} - u_{V,\Gamma}\right) h_{LV},$$
 (2.47)

where the negligible heat flux from the gas side has been omitted. Note, this omission is valid in all collapse regimes.

Introducing the non-dimensional form for liquid temperature, radial coordinate, vapor density, interface speed, vapor velocity, and latent heat from table 2.2, yields

$$\frac{k_L \Delta T_s}{\delta_L} \left( \frac{\partial \theta_L}{\partial \eta} \right)_{\Gamma} = (\rho_{V,sat} \epsilon_V) \left[ \left( \dot{\gamma} - u_{V,\Gamma}^* \right) \frac{R_o}{t_{ref}} \right] (\omega h_{LV}^*). \tag{2.48}$$

Rearranging these terms to obtain an explicit expression for the liquid side heat flux gives

$$\left(\frac{\partial \theta_L}{\partial \eta}\right)_{\eta=0} = \frac{C_1}{\sqrt{B_{sat}}} \epsilon_V \omega \left[\dot{\gamma} - u_V^* \left(\eta = 0, \tau\right)\right], \quad \text{where} \tag{2.49}$$

$$B_{sat} = Ja^2 \frac{\alpha_L}{R_o} \sqrt{\frac{\rho_L}{\Delta P^*}}.$$
 (2.50)

The above analysis summarized by Eq. (2.43) and Eq. (2.49), shows that the bubble dynamics are categorized by two parameters,  $\xi$ , and  $B_{sat}$ . The transient nature of the pressure change that is used to induce a bubble collapse is dictated by  $\xi$ , and and the dependence of collapse behavior on fluid properties and liquid sub-cooling is represented by  $B_{sat}$ . This categorization sets apart the present work from the earlier categorization advanced in [20], which is only based on  $B_{eff}$  or essentially  $B_{sat}$ . An analysis of the non-dimensional form of the auxiliary equations in the CVSI model defined in §(2.3.1) that are used to evaluate variables,  $\pi_V$  and

 $\theta_L$  in Eq. (2.43) and Eq. (2.49) was also done. It revealed that non-dimensional quantities obtained from those equations use the same physical properties as  $\xi$  and  $B_{sat}$  and do not introduce any new parameter, except the ratio of vapor specific heats ( $\gamma_V = C_{pV}/C_{vV}$ ).

The value of  $\gamma_V$  affects the rate of change in vapor pressure (Eq. (2.20)) during bubble collapse. To ascertain its importance for this categorization, in §(2.5.2), we have shown cases for R113 and Water; two fluids with distinct values of  $\gamma_V$ . Tests were conducted for similar values of  $B_{sat}$  and  $\xi$  with both fluids. The thermal, inertial and intermediate regions on the map overlapped even with these different values of  $\gamma_V$ . Changing the fluid affects all thermophysical properties and isolating the effect of  $\gamma_V$  from the variation of other fluid properties  $(\rho_L, \rho_V, h_{LV}, k_L, C_{pL})$  that are included in the mathematical form of  $B_{sat}$  has been left for investigation in a future study.

Now, to determine the corresponding collapse regimes pertaining to specific values for each pair  $\{\xi, B_{sat}\}$ , we compute a large set of calculations as described in the following sections.

#### 2.5.1 Metric for Bubble Collapse

We refer to the discussion in  $\S(2.1)$  and  $\S(2.4)$ , where it was highlighted that the time variation of interface temperature  $(T_{\Gamma}(t))$  has different characteristics across all three categories. Hence, to identify collapse regimes, we compare the trend of interface temperature for collapse with the expected behavior if the collapse was a purely thermal or a purely inertial collapse. First, to establish the baseline behavior with respect to the limiting cases of purely thermal or inertial collapse, we have the following:

• (Purely Thermal Collapse) Bubble remains at a mechanical equilibrium  $(P_V(t) = P_\infty(t))$  and interface temperature is always equal to the corresponding saturation value [20]  $T_\Gamma(t) = T_{sat}(P_\infty(t))$ . In its non-dimensional form, the interface temperature for this collapse is given by

$$\theta_{Therm}(\eta = 0, t) = \frac{T_{sat}(P_{\infty}(t)) - T_{\infty}}{\Delta T_s}.$$
(2.51)

• (Purely Inertial Collapse) The rate of collapse is adequately balanced by condensation, resulting in little to no mass accumulation inside the bubble and constant pressure. Hence,  $T_{\Gamma}(t)$  can be adequately approximated by  $T_{\infty}$  [8, 20], and the theoretical expression for non-dimensional interface temperature for such a case is

$$\theta_{Iner}(\eta = 0, t) = 0. \tag{2.52}$$

Although any practical setup would deviate from these limiting behaviors, it is reasonable to expect that a non-dimensional interface temperature,  $\theta_{\Gamma}$ , defined as

$$\theta_{\Gamma}(t) = \frac{T_{\Gamma}(t) - T_{\infty}}{T_{sat}(P_{\infty}^{max}) - T_{\infty}}$$
(2.53)

will resemble the trend of  $\theta_{Therm}$  for a thermal collapse, while an inertial collapse will have  $\theta_{\Gamma}(t) \cong \theta_{Iner}$ . In contrast, an intermediate collapse has a large variation of bubble pressure and interface temperature during the collapse, and the corresponding  $\theta_{\Gamma}$  trend will significantly deviate from both  $\theta_{Therm}$  and  $\theta_{Iner}$ . Therefore, the deviation of  $\theta_{\Gamma}$  from these

corresponding values can be used in the metrics for defining the collapse regimes. In the present work, these metrics are obtained in a time integrable sense, namely,

$$\Delta_{Therm} = \frac{1}{\tau_T} \int_0^{\tau_T} |\theta_{Therm}(\tau) - \theta_{\Gamma}(\tau)| d\tau, \quad \text{and}$$
 (2.54a)

$$\Delta_{Iner} = \frac{1}{\tau_T} \int_0^{\tau_T} |\theta_{Iner}(\tau) - \theta_{\Gamma}(\tau)| d\tau = \frac{1}{\tau_T} \int_0^{\tau_T} |\theta_{\Gamma}(\tau)| d\tau.$$
 (2.54b)

Here,  $\Delta_{Therm}$  gives the average difference of a given collapse case from purely thermal behavior,  $\Delta_{Iner}$  gives the same difference from a purely inertial collapse, and  $\tau_T$  represents a threshold time until which the differences are computed. Keeping in line with the computations done in this study and as described in §(2.4), we employ a value of  $\tau_T$  equal to the time required for the bubble to collapse to 5% of its initial volume.

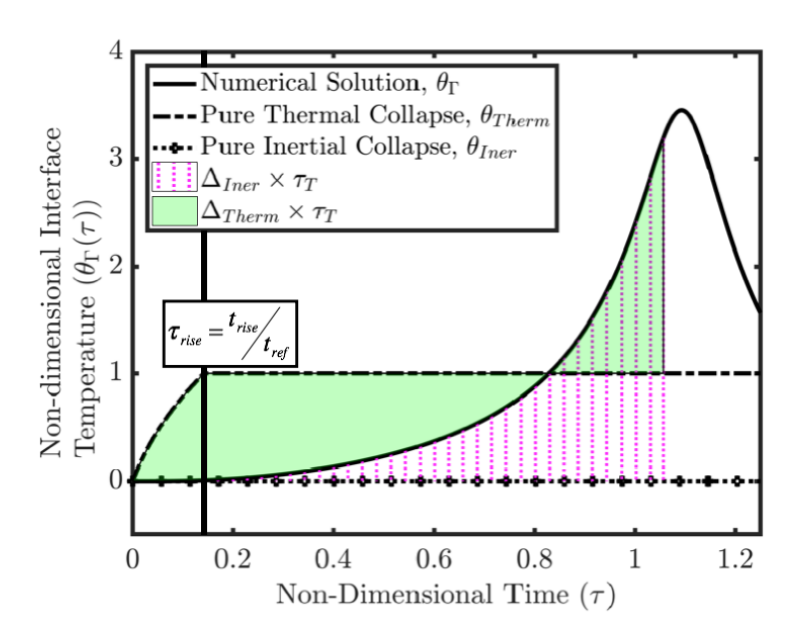


Figure 2.6: Comparison of transient variation of interface temperature for Case # 2 of table 3.1 with  $\theta_{Therm}$  and  $\theta_{Iner}$ .

To explain the use of the categorization metrics, we first give a graphical representation

of  $\theta_{\Gamma}$  with respect to  $\theta_{Iner}$  and  $\theta_{Therm}$  in figure 2.6. The shaded area represents the integrated difference of  $\theta_{\Gamma}$  from pure inertia or pure thermal behavior, which is respectively equal to  $\Delta_{Iner} \times \tau_T$  and  $\Delta_{Therm} \times \tau_T$ . To clearly define the similarity of a bubble collapse towards either thermal or inertial collapse, the categorization is given by

$$\Delta_{Therm}/\Delta_{Iner} \leq 0.1$$
 Thermal Collapse
$$0.1 < \Delta_{Therm}/\Delta_{Iner} < 10$$
 Intermediate Collapse
$$\Delta_{Therm}/\Delta_{Iner} \geq 10$$
 Inertial Collapse

where this ratio can be explicitly written as

$$\frac{\Delta_{Therm}}{\Delta_{Iner}} = \frac{\int_{0}^{\tau_{5\%}} |\theta_{Therm}(\tau) - \theta_{\Gamma}(\tau)| d\tau}{\int_{0}^{\tau_{5\%}} |\theta_{\Gamma}(\tau)| d\tau} = \frac{\int_{0}^{t_{5\%}} |T_{Therm}(t) - T_{\Gamma}(t)| dt}{\int_{0}^{t_{5\%}} |T_{\Gamma} - T_{\infty}(t)| dt}.$$
 (2.56)

With reference to the specific thresholds used in Eq. (2.55), the value of 0.1 represents that the difference of collapse behavior from a purely thermal case is less than 10% of the difference from purely inertial case. On the other hand, the value of 10 represents that the difference from a purely inertial behavior is less than 10% of the difference from purely thermal behavior. These thresholds were found to reasonably predict the category of a range of test cases described in  $\S(2.5.2)$  and also the experimental cases used in numerical validation in  $\S(2.3.3)$ .

#### 2.5.2 Categorization Map

To visualize the new collapse categorization, 558 different collapse calculations using the CVSI model were performed for which,  $B_{sat} \in [1 \times 10^{-3}, 1.4 \times 10^{3}]$  and  $\xi \in [1.3 \times 10^{-2}, 1.6 \times 10^{-2}]$ 

 $10^6$ ]. These calculations were done across two different fluids, namely, water and R113, different maximum system pressures  $(P_{\infty}^{max})$ , different length of system transient period  $(t_{rise})$ , and different superheats  $(\Delta T_s)$ . The results are shown in terms of a generalized

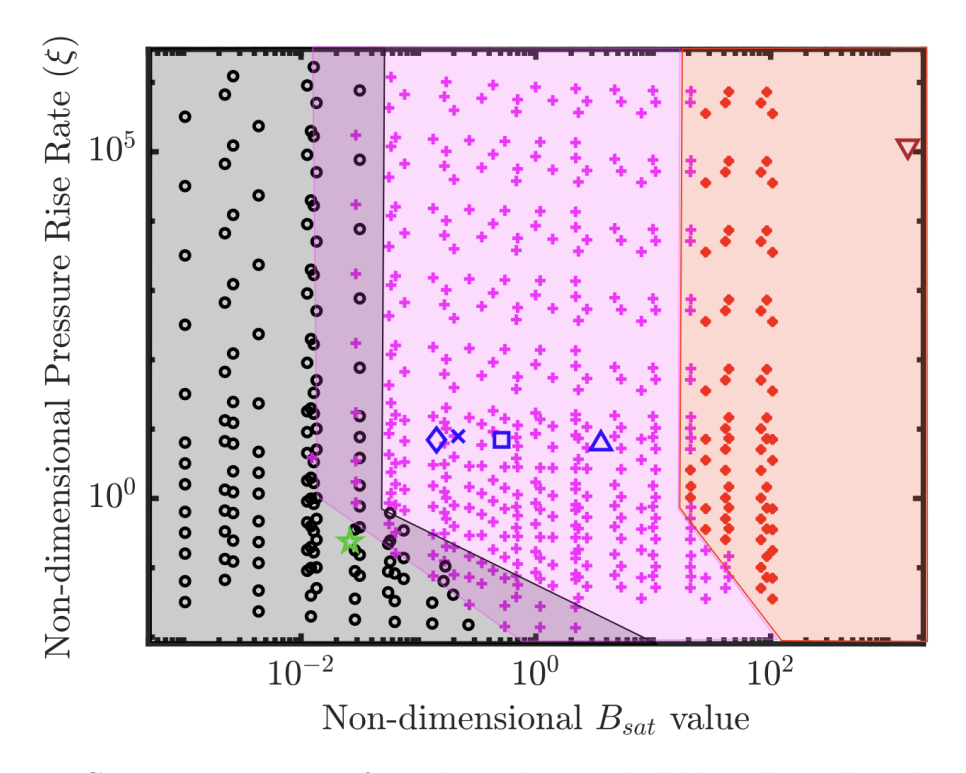


Figure 2.7: Categorization map for spherical vapor bubble collapse based on  $B_{sat}$  and  $\xi$  values. Collapse categories: Thermal ( $\circ$ ), intermediate (+), and inertial (\*). Table 2.1 cases are also marked in the map: Case # 1 -  $\star$ ; Case # 2 -  $\diamond$ ; Case # 3 -  $\times$ ; Case # 4 -  $\square$ ; Case # 5 -  $\Delta$ ; Case # 6 -  $\nabla$ .

collapse map presented in figure 2.7, where each point in the map represents an individual collapse event, i.e. a single calculation. Each event is categorized based on the metric defined by Eq. (2.55). Additionally, all six experimental cases described in table 2.1 are included and it is reassuring to see that the category for each case matches the one obtained with the new collapse categorization.

Starting from the top portion of the map, for a value of  $\xi > 1$ , the regime identification is essentially independent of the specific value of  $\xi$  and only dependent on  $B_{sat}$ . For such

large values of  $\xi$ , the far-field pressure rise rate is quick, matching the conditions that have been employed in the earlier categorization [20]. Therefore, our results corroborate previous findings where  $B_{sat}$  is the key category-identifying parameter. The only slight difference is that a sharp distinction between the intermediate and thermal collapse is lacking. The present results indicate more of a gradual transition between these two categories of collapse.

For  $\xi < 1$ , however, the regime map becomes much richer and the regime distinction deviates from this  $B_{sat}$  only categorization. Looking at the transition from thermal to intermediate collapse, the mapping from figure 2.7 indicates that as the value of  $\xi$  decreases below 1, we observe a slower collapse resembling thermal regime behavior even for larger  $B_{sat}$  values. The deviation continues to increase with decreasing values of  $\xi$  to such an extent that even with  $B_{sat}$  as large as 1, the behavior is representative of thermal collapse. This represents two orders of magnitude deviation from the threshold observed for  $\xi > 1$ . Similar deviations are observed for intermediate-inertial regime boundary, where cases with  $\xi < 1$  are found to behave like an intermediate collapse even for large  $B_{sat}$  values of  $\sim 100$ . The authors would like to note that in some cases, where  $\xi < 1$ , the system pressure  $(P_{\infty}(t))$ realized in far-field liquid until the bubble reaches 5% of its initial volume  $(P_{\infty}(t_{5\%}))$  is smaller than the maximum prescribed value of  $P_{\infty}^{max}$ . This choice of maximum system pressure, which is used in evaluating  $\Delta P^*$  only affects the value of  $\xi$  and  $B_{sat}$ , i.e., position of a specific point on the collapse map. Hence, for clarity of representation the values of  $\xi$  and  $B_{sat}$  are always evaluated using  $\Delta P^*$  as defined in Eq. (2.3) in this study. In cases where  $P_{\infty}^{max}$  is not realized,  $\Delta P^*$  serves as a notional pressure difference.

This tendency towards a milder collapse is expected for small values of  $\xi$ . It represents a slower rate of increase in system pressure (larger  $t_{rise}$ ), which implies that the effective pres-

sure difference forcing the bubble collapse remains much smaller than the possible maximum,  $(P_{\infty}(t) - P_V(t) < \Delta P^*)$ . Moreover, this gradual change in system pressure allows more heat diffusion in liquid before the system reaches its maximum pressure. It results in a larger thermal boundary layer, which limits the rate of heat transfer and hence, condensation. Therefore, even when  $B_{sat} > 0.01$ , we may observe a slow and gradual collapse if  $t_{rise}$  is large or equivalently,  $\xi$  is small. Slow system pressure rise allows time to establish a mechanical equilibrium across the bubble surface, which resembles a thermal collapse. Similarly, at the intermediate-inertial boundary, even if  $B_{sat} > 30$ , a slow rise in the system pressure allows time for thermal boundary thickness to increase around the bubble. Slow liquid heat transfer starts to limit the rate of condensation resulting in an imbalance between collapse rate and condensation rate described in §(2.4.1). Consequently, the resulting process falls in the category of an intermediate collapse.

#### 2.6 Summary

This chapter revisits the dynamics of a vapor bubble collapsing in a homogeneous surrounding liquid phase. It has been presented into two parts, where first the dynamics of an intermediate type of collapse are analyzed and explained, and second, a generalized framework for categorizing bubble collapse is introduced.

With respect to the first aspect of the work, an analysis of intermediate collapse, where both heat transfer and liquid inertia are important, reveals that it is characterized by a continuous change in interface temperature and vapor pressure. This distinguishes the intermediate regime from thermal or inertia-dominated collapse. The fundamental reason for the pressure and temperature variation is found to be caused by a substantial interfacial vapor velocity, which can be interpreted as an imbalance between the bubble surface regression rate and the rate of condensation.

In the second part of this work, it is mathematically shown that the behavior of bubble collapse is not solely dependent on the fluid properties and liquid sub-cooling, but also on the rate of increase in system pressure that initiates the collapse. It is shown that at the same level of liquid sub-cooling, the behavior of bubble collapse can be modified by changing the rate of change of system pressure by adjusting  $t_{rise}$ . For more gradual changes in the system pressure, the thermal mechanism of bubble collapse increases in importance. These findings are quantified by creating a generalized categorization map shown in figure 2.7, where the parameter space is defined by the following two non-dimensional quantities, namely,

$$\xi = \frac{R_o}{t_{rise}} \sqrt{\frac{\rho_L}{P_{\infty}^{max} - P_{sat}(T_{\infty})}}, \quad \text{and} \quad B_{sat} = Ja^2 \frac{\alpha_L}{R_o} \sqrt{\frac{\rho_L}{P_{\infty}^{max} - P_{sat}(T_{\infty})}}.$$

The resulting map divides the bubble collapse process into three regimes representing thermal, intermediate, and inertial dominated collapse. For values of  $\xi$  exceeding one, it is observed that the influence of this parameter is negligible in the distinction of collapse regimes reducing the categorization to the traditional given by  $B_{sat}$  [20]. However, for values  $\xi$  below one, this parameter along with  $B_{sat}$  play an active role in identifying the bubble collapse regime. As such, this study shows that the rate of change in system pressure can be effectively used to alter the behavior of vapor bubble collapse.

### Chapter 3

Assessing the Physical Validity of

Highly Resolved Simulation

Benchmark Tests for Flows

## **Undergoing Phase Change**

A more versatile method for studying bubble dynamics is by performing three-dimensional Highly Resolved Simulations. Such a simulation for a vapor bubble needs to solve a general three-dimensional two phase flow with a continuously deforming interface, and capture the interfacial process of phase change. Development of such methods for two phase flows that can handle the phase change phenomenon by directly implementing the interfacial conditions has been a subject of wide interest in the past few years [50, 54, 58–60, 82–97]. These studies can be categorized based on the underlying scheme used for the advection of the liquid-

vapor interface, namely, Volume of Fluid (VoF) [83, 89, 90, 92, 93, 95, 96], Level Set (LS) [54, 58, 85–88], coupled LS-VoF [50, 91], or Front-Tracking (FT) [82, 84, 97]. In the course of developing these numerical methods to handle the interfacial jump conditions, certain physical assumptions have become almost universally adopted [50, 54, 58, 60, 83, 85–96]. These assumptions are:

- i) Incompressibility in both the liquid and vapor phases (except at the interface), implying respectively that the liquid and vapor densities are constant.
- ii) A constant interface temperature equal to the saturation temperature corresponding to far-field pressure, namely  $T_{\Gamma}(t) = T_{sat}(P_{\infty})$ .

The above assumptions will be referred to as the underlying HRS assumptions in this study.

A key validation exercise found in many HRS studies consists of the growth of a bubble immersed in a superheated liquid domain. This test case represents a fundamental and necessary step in the confident application of a numerical technique to more general phase change problems. In the aforementioned simulation papers [54, 84, 85, 90, 92–94, 96], none of them have thoroughly inspected the physical characteristics of bubble growth and in that context examined the validity of the underlying HRS assumptions. Hence, before diving deeper into the development of such an in-house simulation tool, we leverage the CVSI model developed in chapter 2 to better understand the limitation of the HRS assumptions.

In this chapter, we use the canonical bubble growth test case to demonstrate the extent to which the incompressibility and constant interfacial temperature assumptions hold under pertinent phase change conditions. Solving for bubble growth using the CVSI model allows for temporal changes in the interface temperature, vapor pressure, and vapor density inside the bubble. This makes the CVSI model, physically more general for spherically symmetric bubble dynamics than existing HRS solution methods [50, 54, 58, 60, 83, 85–96], and hence, it offers the necessary benchmark information from which to analyze the applicability of the underlying assumptions for phase change HRS methods. In §(3.1), the results are compared with experimental data to show that the CVSI predicts bubble growth accurately, similar to the collapse validation presented in §(2.3.3). This is followed by a comparison of CVSI and HRS results in §(3.2), as well as commonly used analytical solutions, which lead to the finding that the discrepancy with HRS lies in the initial inertial-controlled bubble growth stage. The identification of this initial period under variable operating conditions is done in a closed analytical form in §(3.2.1). Finally, in §(3.3), a summary of this chapter is presented.

#### 3.1 Validating the CVSI Solution

The first step in critically analyzing the underlying HRS assumptions is to ascertain that the physically more accurate CVSI model for spherical vapor bubble growth performs as well as it does for a collapse as discussed in chapter 2. With this goal in mind, CVSI results are compared to six different experimental datasets of bubble growth. The parameters of these experiments are provided in table 3.1. An important system parameter is related to the liquid superheat that governs the process of bubble growth. Here, it is denoted by  $\Delta T_{sh} = -\Delta T_s$ , where  $\Delta T_s$  is defined in Eq. (2.2). Note that unlike the previous study on collapse, the far-field pressure is assumed to remain a constant. Hence,  $P_{\infty}^{max}$  is simply equal to  $P_{\infty}$ . Additionally, an analytical solution for bubble radius given by Scriven [35] is also plotted in the experiment vs CVSI comparison. This analytical solution is often used in validating HRS approaches. It

Case # and	Fluid	Superheat	System Pressure	Initial Radius	Jakob Number
Refs.		(in K), $\Delta T_{sh}$	(in atm), $P_{\infty}$	(in mm), $R_o$	Ja
1a,b [25]	Water	2.9	1.00	0.021	8.68
2 [24]	Water	10.5	1.19	0.004	26.70
3 [26]	Water	9	0.38	0.014	65.11
4 [27]	Water	20.3	0.318	0.007	128.55
5 [26]	Water	7.34	0.132	0.025	142.16
6 [30]	R113	34.11	0.083	0.005	413.98

Table 3.1: Description of experimental datasets used for validation of the CVSI method.

is based on a saturated vapor state for the bubble contents that is constant in time; hence, it directly implies constant vapor density and interfacial temperature, i.e. the assumptions under scrutiny in the present work. The analytical expression for bubble radius given by Scriven [35] is

$$R(t) = 2\beta \sqrt{\alpha_L t}$$
 or  $\dot{R}(t) = \beta \sqrt{\frac{\alpha_L}{t}}$ , (3.1)

where  $\beta$  is evaluated from the following transcendental equation

$$2\beta^{2} \int_{0}^{1} e^{\left(-\beta^{2}\left((1-\zeta)^{-2}-2\left(1-\frac{\rho_{V}}{\rho_{L}}\right)\zeta-1\right)\right)} d\zeta = \frac{\rho_{L}C_{pL}\Delta T_{sh}}{\rho_{V}\left(h_{LV}+\left(C_{pL}-C_{pV}\right)\Delta T_{sh}\right)}$$

$$= \frac{Ja}{\left(1+\frac{\left(C_{pL}-C_{pV}\right)\Delta T_{sh}}{h_{LV}}\right)}.$$
(3.2)

Here,  $C_{pL}$  and  $C_{pV}$  are the respective liquid and vapor specific heats at constant pressure, and Ja is the Jakob number defined as

$$Ja = \frac{\rho_L C_{pL} \Delta T_{sh}}{\rho_V h_{LV}}. (3.3)$$

The Jakob number is evaluated using the liquid properties  $\rho_L$  and  $C_{pL}$  obtained at  $T_{\infty}$ ; while,  $\rho_V$  and  $h_{LV}$  are evaluated at  $T_{sat}(P_{\infty})$ .

The comparison between the bubble radius time histories obtained from experimental data, analytical solution, and CVSI predictions are shown in figure 3.1 for the six different cases described in table 3.1. The bubbles observed in these experiments were not entirely spherical as described in those papers. Even then, the equivalent radius obtained in those studies from the oblate or prolate shapes of the bubbles matches well with the radius vs. time predictions from the CVSI solution. For datasets #1 and #2, the agreement among the CVSI and analytical predictions, as well as the experimental data, is good. The only minor difference between analytical and CVSI result is at early times. For Ja = 65.11, 128.55, 142.16, and 413.98, the CVSI results match the experiments quite well over the entire time period, while the analytical solutions show a noticeable deviation, which is particularly pronounced at earlier times. The explanation for this discrepancy is postponed until after the comparison to HRS results is presented in the next section, since the discussion shares some of the same issues faced by HRS.

# 3.2 Departure from Physically Accurate Behavior in Published HRS Results

The validated CVSI method is used in this section to simulate three distinct systems of bubble growth that have been previously used as test cases in HRS studies [54, 90, 93, 94, 96]. The comparison is shown in figure 3.2 and the operating parameters for these cases are given

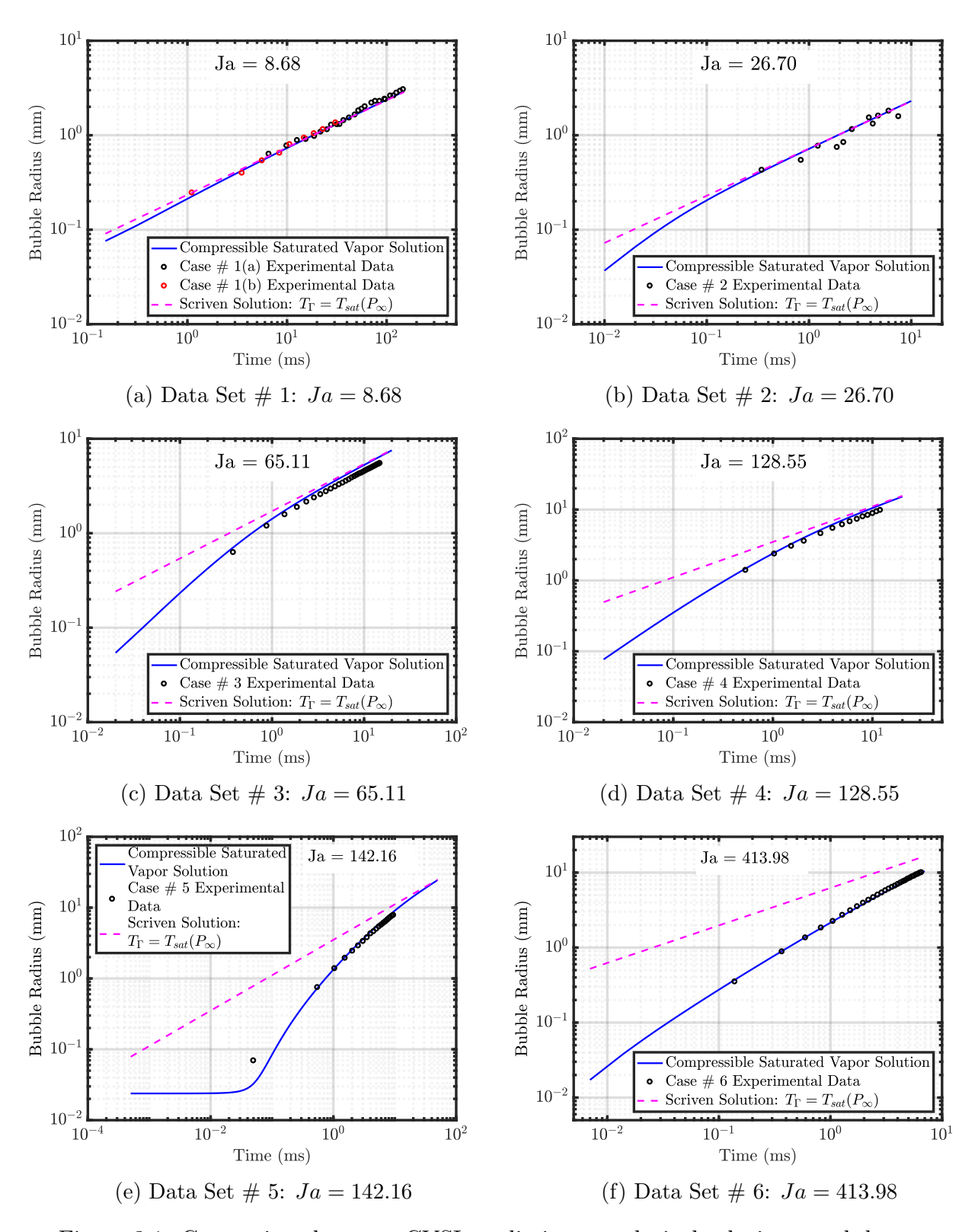


Figure 3.1: Comparison between CVSI predictions, analytical solutions, and datasets presented in table 3.1

in table 3.2. These HRS studies used the Scriven solution (Eq. (3.1)) as a reference, and hence, it is also included in figure 3.2.

At Ja = 9.88, over the time period shown, the CVSI solution nearly overlaps with both the Scriven solution and the HRS results. At Ja = 14.95, a clear difference is noted between the CVSI solution and both, the Scriven and the HRS predictions. For this particular case (shown in figure 3.2b), the time period corresponds to the early phase of bubble growth, where the time window ranges from  $10^{-3}$  to  $10^{-1}$  ms, as opposed to the case for Ja = 9.88, where the time range is  $10^{0}$  to  $10^{2}$  ms. For the larger Ja case (Ja = 27.92), the comparison between all three bubble radius calculations is shown for the latter part of the bubble growth period, namely between  $2 \times 10^{-1}$  and  $3 \times 10^{0}$  ms. And in this period the agreement between CVSI, Scriven, and HRS is fairly good. However, at earlier times a noticeable discrepancy is noted between the Scriven and CVSI solutions in a similar fashion as the results presented in figure 3.1.

Based on the comparison presented in figure 3.2, it appears that the Scriven and HRS results are in close agreement for all cases presented. This is not entirely surprising since both formulations use a constant interface temperature and vapor density. In contrast, with respect to the CVSI solution, it is observed that during the early phase of bubble growth, the

Case # and	Fluid	Superheat	System Pressure	Initial Radius	Jakob Number
References					
		(in K), $\Delta T_{sh}$	(in atm), $P_{\infty}$	(in mm), $R_o$	Ja
1 [54]	Water	3.30	1.00	0.018	9.88
2 [90, 93, 94,	Water	5.00	1.00	0.006	14.95
96]					
3 [90]	HFE-7100	10.00	0.493	0.002	27.92

Table 3.2: Description of cases used in HRS studies.

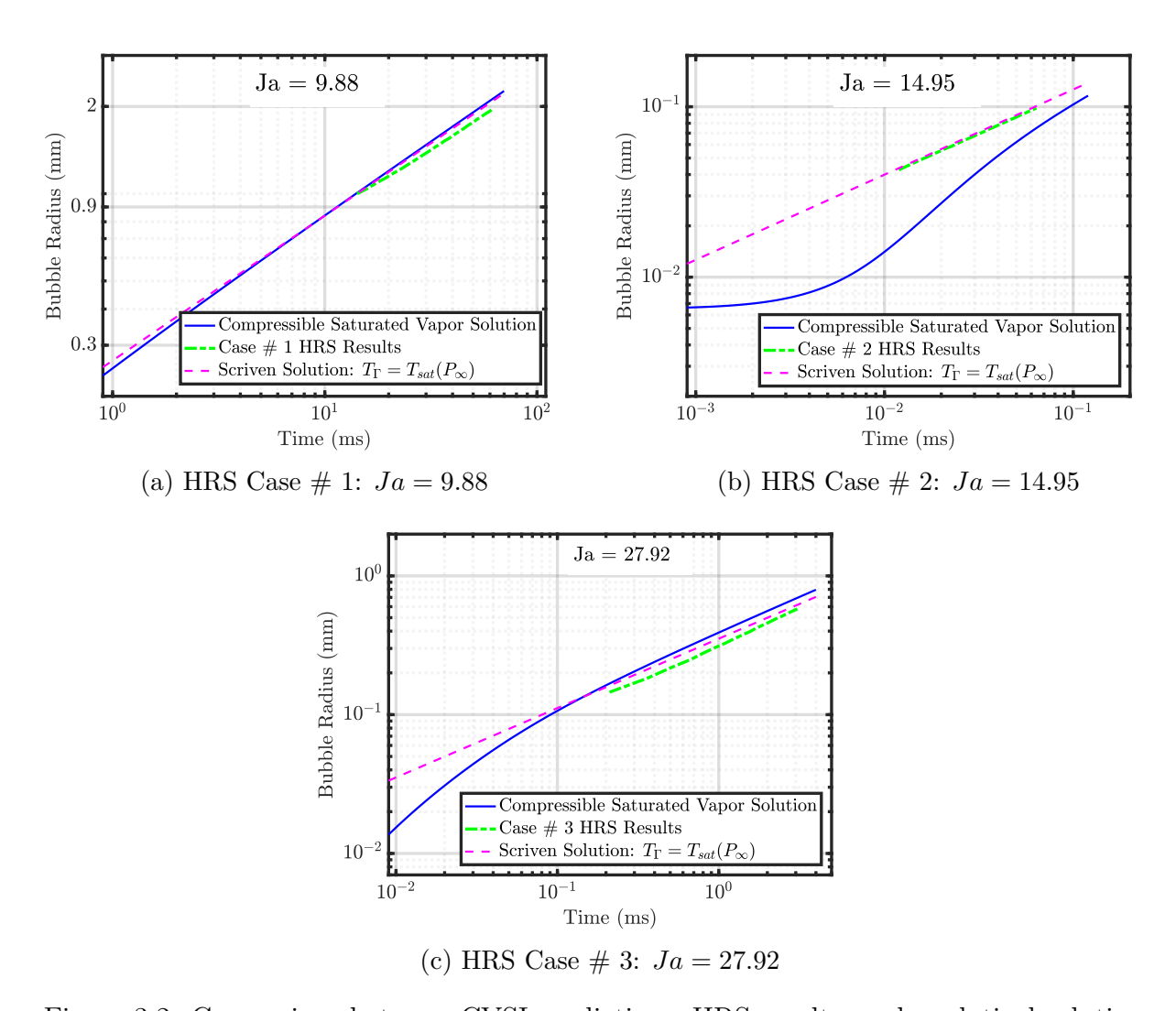


Figure 3.2: Comparison between CVSI predictions, HRS results, and analytical solutions pertaining to the cases included in table 3.2

discrepancy between the CVSI results and the results obtained with both Scriven and HRS is noticeable. We interpret this difference as an error in the HRS predictions. To examine this error in more detail and to investigate the role of constant interface temperature and

vapor density, these quantities are first put in non-dimensional form, namely

Non-Dimensional Interface Temperature, 
$$\theta_T = \frac{T_{\Gamma}(t) - T_{sat}(P_{\infty})}{T_{\infty} - T_{sat}(P_{\infty})},$$
 (3.4)

Non-Dimensional Vapor Density at Interface, 
$$\theta_{\rho} = \frac{\rho_{V,\Gamma}(t) - \rho_{sat}(T_{sat}(P_{\infty}))}{\rho_{sat}(T_{\infty}) - \rho_{sat}(T_{sat}(P_{\infty}))},$$
 (3.5)

Non-Dimensional Time, 
$$\tau = \frac{t}{t^*} = \frac{Ja^2\alpha_L}{R_o^2}t.$$
 (3.6)

Note that the non-dimensional time used for this work is different from the one defined in table 2.2. Here, the reference time,  $t^*$ , comes from the time required to achieve the initial bubble radius nucleus,  $R_o$ , based on Scriven's solutions (Eq. (3.1)). Namely,  $t^* = R_o^2/(\alpha_L J a^2)$ , where  $\beta$  value of the Scriven solution has been approximated by Ja, which is an excellent approximation when  $\rho_V \ll \rho_L$  and  $(C_{pL}\Delta T_{sh}/h_{LV}) \gtrsim 0.01$ . The reference denominator values used to obtain non-dimensional interface temperature and vapor density, in Eq. (3.4) and Eq. (3.5) are the maximum variation these quantities can theoretically experience.

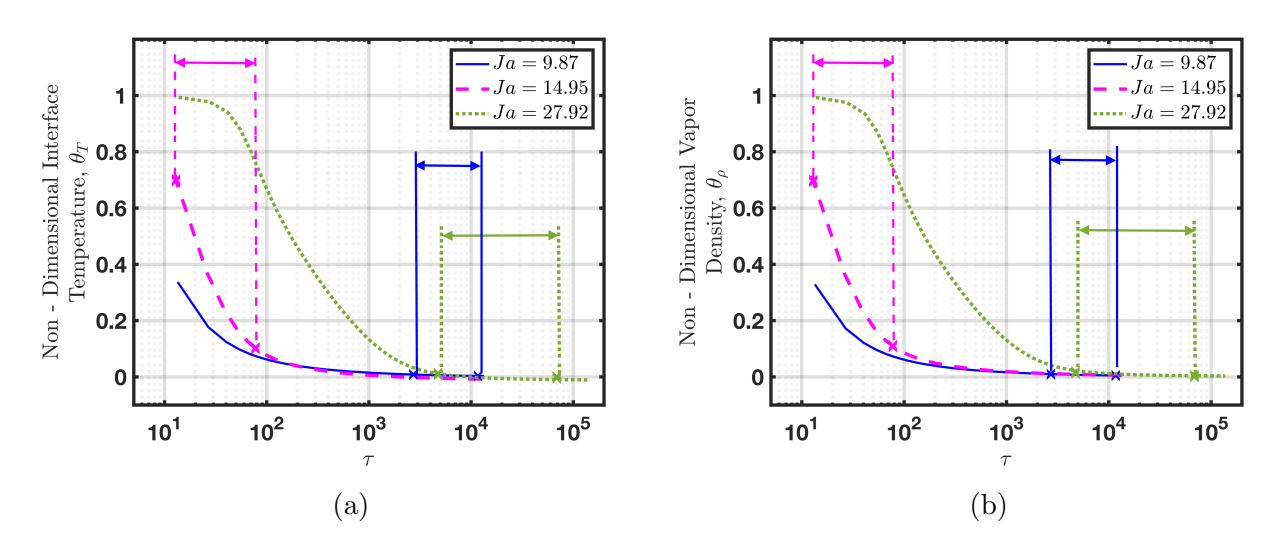


Figure 3.3: Non-dimensional interface temperature (left) and vapor density (right) as a function of time for the cases described in table 3.2. The arrows mark the time period for which HRS results have been reported [54, 90, 93, 94, 96].

The time histories for non-dimensional temperatures and densities are plotted in figure 3.3 showing a monotonic decrease to zero from an initial finite value. Superimposed on these curves are the time periods over which the HRS results were reported in various studies [54, 90, 93, 94, 96]. Clearly, the error in HRS occurs precisely before  $\theta_T$  and  $\theta_\rho$  have approached their asymptotic values of 0. During the initial transient period both the interfacial temperature,  $T_{\Gamma}(t)$  and density  $(=\rho_{V,sat}(T_{\Gamma}(t)))$  are changing in time. Hence, the discrepancy or error in HRS results stems directly from the fact that this time evolution of vapor contents is not taken into account.

Considering the literature on the subject of bubble growth, particularly the work of Plesset and Zwick [33], Prosperetti [41], Robinson and Judd [49], Plesset and Prosperetti [98], we find that the initial transient period corresponds to the inertial bubble growth phase. During this period, the bubble vapor pressure undergoes significant changes, and depending on the Jakob number, various terms in the Rayleigh-Plesset equation become active. Beyond this inertia-controlled time period, we enter into the heat-transfer dominated stage, which is characterized by a nearly constant interface temperature, vapor pressure, and vapor density. Basically, the two underlying HRS assumptions are valid during this latter stage of bubble growth. Hence, the key to avoiding issues associated with the violation of the underlying assumptions in HRS lies in identifying apriori the heat transfer dominated regime. This is elaborated in the following subsection.

## 3.2.1 Identifying Apriori Conditions Favorable to the Current HRS Treatment

A previous attempt at quantifying the threshold time beyond which the bubble growth can be assumed to be in the heat transfer dominated period of growth was reported by Lee and Merte Jr. [45]. The basis was comparing a semi-empirical solution, i.e. the MRG solution [36], which holds over both inertial and heat transfer stages to a solution derived by Plesset and Zwick [33] for exclusive use in the heat transfer dominated stage. Lee and Merte Jr. [45] indicated that beyond a threshold time, given by

$$50 \times \tau_{ref} = 50 \times \frac{18Ja^2}{\pi} \frac{\rho_L T_{sat} \alpha_L}{h_{LV} \rho_V \Delta T_{sh}},\tag{3.7}$$

the difference in the bubble radius predictions from the two solutions is less than 10%, and hence, it can be interpreted that beyond  $t = 50\tau_{ref}$ , the bubble has entered the heat-transfer dominated stage. In this expression, all thermophysical properties are evaluated at the saturation temperature,  $T_{sat}(P_{\infty})$ .

To examine the accuracy of Eq. (3.7), we employ predictions generated by the CVSI numerical procedure, which are more accurate than the MRG solution, and compare these predictions to the Scriven solution [35]. Our rationale is that the Scriven solution, which holds in the heat-transfer regime, does not make additional assumptions concerning the thickness of the boundary layer ( $\delta_L \ll R$ ) as opposed to the expression given by Lee and Merte Jr. [45]. Hence, it is interpreted as being more accurate. We can subsequently compare the CVSI and Scriven's predictions to determine the threshold time when both of these predictions agree

within 10%. The results show that for Ja = 8.68, this threshold time begins at  $t \approx 236 \times \tau_{ref}$ ; while, for Ja = 413.98, this same reference time begins at  $t \approx 13 \times \tau_{ref}$ . For all of the other cases, the results lie between this range demonstrating an undesirable level of variability in the prediction of threshold time using Eq. (3.7). To address this problem we develop an alternative approach.

We begin with simplifying the Rayleigh-Plesset equation (Eq. (2.23)) to its most dominant terms [10] during the bubble growth process, namely

$$R\ddot{R} + \frac{3}{2}\dot{R}^2 + \frac{2\sigma}{R\rho_L} = \frac{P_V(t) - P_\infty}{\rho_L}.$$
 (3.8)

The RHS of Eq. (3.8) can be written in terms of temperature by using a first order approximation of Clausius-Clapeyron equation given by

$$\frac{P_V(t) - P_\infty}{T_\Gamma(t) - T_{sat}(P_\infty)} = \frac{\rho_{V,sat}(T_{sat}(P_\infty))h_{LV}}{T_{sat}(P_\infty)}.$$
(3.9)

On substituting Eq. (3.9) into Eq. (3.8) we get

$$R\ddot{R} + \frac{3}{2}\dot{R}^2 + \frac{2\sigma}{R\rho_L} = \frac{\rho_V h_{LV}}{T_{sat}(P_\infty)} \left(\frac{T_\Gamma(t) - T_{sat}(P_\infty)}{\rho_L}\right) = \frac{\rho_V h_{LV}}{\rho_L T_{sat}(P_\infty)} \theta_T(t) \Delta T_{sh}, \qquad (3.10)$$

where  $\rho_V$ ,  $h_{LV}$ , and  $\rho_L$ , correspond to saturation properties at  $P_{\infty}$  and the temperature difference on the RHS is rewritten in non-dimensional form (Eq. (3.4)).

In the heat transfer controlled regime, we can express R(t) as  $2\beta\sqrt{\alpha_L t}$  (Eq. (3.1)) from

the Scriven solution. This can be substituted directly into Eq. (3.10), yielding

$$\left(2\beta\sqrt{\alpha_L t}\right) \frac{\mathrm{d}^2\left(2\beta\sqrt{\alpha_L t}\right)}{\mathrm{d}t^2} + \frac{3}{2} \left(\frac{\mathrm{d}\left(2\beta\sqrt{\alpha_L t}\right)}{\mathrm{d}t}\right)^2 + \frac{2\sigma}{\left(2\beta\sqrt{\alpha_L t}\right)\rho_L} = \frac{\rho_V h_{LV}}{\rho_L T_{sat}(P_\infty)} \theta_T(t) \Delta T_{sh}.$$
(3.11)

This expression only holds in the heat transfer controlled-regime, where it is expected that  $\theta_T \ll 1$ . Denoting  $\chi = \sqrt{t}$ , the above expression can be rearranged to give the following quadratic expression for  $\chi$ ,

$$\left(2\theta_T \frac{\rho_V h_{LV}}{\rho_L T_{sat}(P_\infty)} \Delta T_{sh}\right) \chi^2 - \left(\frac{2\sigma}{\beta \rho_L \sqrt{\alpha_L}}\right) \chi - \beta^2 \alpha_L = 0,$$
(3.12)

where the thermo-physical properties are evaluated at  $T_{sat}(P_{\infty})$ . To compute the extent of the initial transient period or threshold time,  $t_{threshold}$ , for a given bubble growth case, we directly solve Eq. (3.12) using a suitably small value of  $\theta_T$ . This gives us

$$t_{threshold} = \left( \left[ \frac{4\theta_T \rho_V h_{LV} \Delta T_{sh}}{\rho_L T_{sat}(P_{\infty})} \right]^{-1} \left\{ \frac{2\sigma}{\beta \rho_L \sqrt{\alpha_L}} + \sqrt{\left( \frac{2\sigma}{\beta \rho_L \sqrt{\alpha_L}} \right)^2 + \left( \frac{8\theta_T \rho_V h_{LV}}{\rho_L T_{sat}(P_{\infty})} \right) \beta^2 \alpha_L \Delta T_{sh}} \right\} \right)^2,$$
(3.13)

where the largest root is chosen, since it coincides with the physically relevant situation of being situated within the heat-transfer dominated period.

For  $\theta_T = 0.1$ , we found that the difference in bubble radius predicted by the Scriven

solution, and CVSI solution, given by

$$\epsilon_R = \frac{|R_{CVSI}(t_{threshold}) - R_{Scriven}(t_{threshold})|}{R_{CVSI}(t_{threshold})} \times 100, \tag{3.14}$$

was less than 10% for all the cases presented in this work. This is shown in table 3.3. Values of  $\theta_T$  larger than 0.1 place the solution either within the inertial range or close to it thereby increasing the error,  $\epsilon_R$ . For  $\theta_T \ll 0.1$ , unreasonably large values of  $t_{threshold}$  can be predicted. Although this would ensure that the bubble growth is more accurately predicted by the Scriven solution, such a conservative estimate is not found to be necessary because even at  $\theta_T = 0.1$ ,  $\epsilon_R$  is already sufficiently low. Hence, the value of  $\theta_T = 0.1$  provides a reasonable approximation for  $t_{threshold}$ , beyond which the HRS assumptions remain valid.

Case	$t_{threshold}$ from	$\epsilon_R$	
Description	Eq. (3.13) for $\theta_T = 0.10$	from Eq. (3.14)	
# 1  from table  3.1	$2.01 \mathrm{\ ms}$	7.55 %	
# 2  from table  3.1	$0.38 \mathrm{\ ms}$	1.53~%	
# 3 from table 3.1	2.85  ms	3.34 %	
# 4 from table 3.1	$9.10 \mathrm{\ ms}$	0.97~%	
# 5 from table 3.1	$26.21 \mathrm{\ ms}$	6.31~%	
# 6 from table 3.1	171.97  ms	6.41~%	
# 1  from table  3.2	1.59  ms	5.31~%	
# 2 from table 3.2	$0.79 \mathrm{\ ms}$	0.49~%	
# 3 from table 3.2	$0.30~\mathrm{ms}$	5.60 %	

Table 3.3: Prediction of threshold times for achieving solutions in the heat-transfer-dominated regime and the associated error with respect to the CVSI solution.

HRS based on incompressibility and constant interface treatment should initialize bubbles with a radius given by  $R_{initial} > 2\beta\sqrt{\alpha_L t_{threshold}}$ , where  $t_{threshold}$  is given in Eq. (3.13). This should be combined with a Scriven temperature profile [35]. Adopting these measures would ensure that the underlying HRS assumptions would not be violated during the bubble growth

process.

#### 3.2.1.1 Departure from sphericity

In various applications, the vapor bubble may depart from spherical symmetry due to translation under the effect of buoyancy. For the analysis presented in the paper to remain applicable, the bubble must be nearly spherical up to at least the threshold time described by Eq. (3.13). Following the line of reasoning provided by Brennen [61], a significant deviation from sphericity would happen if the viscous force, which is of the form  $\mu W_{\infty}D$  is comparable to the characteristic force maintaining sphericity,  $\sigma D$ , for a Reynolds number  $(Re = \rho W_{\infty}D/\mu)$  range such that  $Re \ll 1$ . In this viscous dominated regime the ratio of destabilizing and stabilizing forces can be shown to be given by We/Re, where We is the Weber number  $(\rho W_{\infty}^2 D/\sigma)$ . In the opposite extreme, for  $Re \gg 1$ , the destabilizing force would be  $\rho W_{\infty}^2 D^2$ , and the aforementioned ratio becomes simply We. Thus, over the full range of Re, we can interpret max(We/Re, Re) as the ratio of destabilizing over stabilizing forces. When this ratio reaches the limit of one, we expect departures from sphericity to become significant. In the above expressions  $\mu$ ,  $W_{\infty}$ ,  $\sigma$ ,  $\rho$ , and D, are respectively the dynamic viscosity, terminal bubble velocity, surface tension coefficient, liquid density, and diameter. The terminal velocity, which is required in the calculation of the pertinent non-dimensional quantities is given by [61]

$$W_{\infty} = \left(\frac{4Dg}{3C_D}\right)^{1/2},\tag{3.15}$$

where the drag coefficient can be obtained over a broad range of Re from the work of Mikhailov and Freire [99] (Equation 8 in their paper). This allows for the direct calculation of max(We/Re, Re) as a function of bubble diameter as shown in figure 3.4.

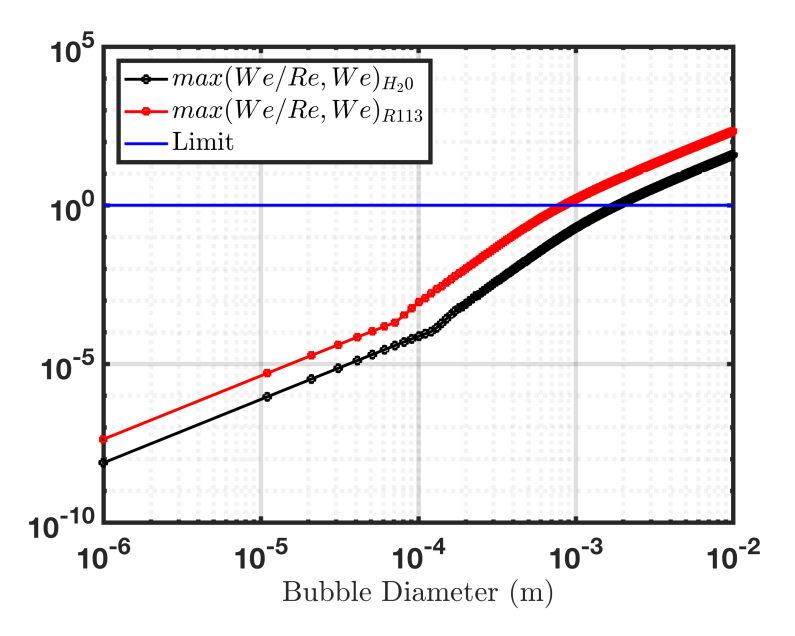


Figure 3.4: Ratio of destabilizing over stabilizing forces (max(We/Re, Re)) for the preservation of bubble sphericity as function of diameter for water and R113 systems.

The results in figure 3.4 indicate that significant departures from sphericity are not expected to occur until the bubble diameter reaches a threshold size of approximately 1 mm. At this point, the ratio reaches a critical value of 1 indicated in the plot by the blue limit line. Results using water and R113 properties are relatively close and lead to a similar threshold size for the bubble. For most practical fluids, the Haberman-Morton Number,  $Hm = g\mu^4/(\rho\sigma^3)$ , is  $Hm < 10^{-10}$ , and in this Hm range similar values for the threshold bubble size are obtained.

Considering the various CVSI to experimental data set comparisons included in figure 3.1 of the present paper, the most significant deviations from the incompressibility and constant interface temperature assumptions (HRS assumptions) take place when the bubble is sub-

stantially smaller than 1 mm. In fact, once the bubble reaches the 1 mm size for cases where the Ja is less than  $\mathcal{O}(100)$ , the deviations from the HRS assumptions are negligible. This means that HRS can be performed under the current assumptions with no problem. For cases where Ja is  $\mathcal{O}(100)$  or greater, serious deviations from the HRS assumptions are recorded at a bubble size of 1 mm. However, under these demanding conditions, the HRS would face additional formidable numerical challenges imposed by stringent requirements of numerical resolution at large values of Ja.

## 3.3 Summary

Bubble growth process is well-known to be comprised of an initial inertia-controlled phase followed by a heat-transfer controlled phase. The HRS methods are shown here to be inaccurate in the inertia-controlled stage of the growth process. The reason for this inaccuracy is the inability of these methods to capture the time variation of the interface temperature, and its coupling with the bubble pressure. Usually, HRS methods are judged against the Scriven solution [35], which by construction only holds in the heat-transfer-dominated regime; hence, the initial discrepancy associated with the inertial-controlled growth stage cannot be tested accurately if the reference solution is invalid. Furthermore, this initial transient period becomes more dominant with increasing Jakob (Ja) number. Beyond this initial transient, once the bubble enters the heat transfer dominated regime, the underlying HRS assumptions of incompressibility and constant interface temperature hold remarkably well.

The work presented in this chapter provides a theoretical framework for specifying appropriate initial set of conditions, which hold under incompressibility and constant interface temperature, since most of the methods operate under these assumptions. It does not propose a change in HRS simulation methodology but establishes the time period during which such methods are physically valid. This is accomplished in this work by first determining the time required for a bubble to enter the heat transfer dominated regime using a reduced form of the Rayleigh-Plesset equation along with Scriven solution for bubble radius. This results in an analytical closed form expression for this time, denoted as the  $t_{threshold}$  (Eq. (3.13)), which can be subsequently employed to calculate the corresponding bubble radius, namely  $2\beta\sqrt{\alpha_L t_{threshold}}$ . This bubble radius can be combined with the Scriven temperature profile [35] to provide the appropriate initial conditions. Even for aspherical bubbles found in a variety of applications, it is reasonable to infer that simulations should only deal with bubble sizes that have an equivalent bubble radius greater than  $2\beta\sqrt{\alpha_L t_{threshold}}$ , if the numerical methodology uses the underlying HRS assumptions.

# Chapter 4

# Numerical Method Development for

# Two-Phase Flows With Phase Change

In the previous chapter, we have reported about the limitations of the constant interface temperature and vapor density assumptions used in previously published phase change simulation methods [50, 54, 58–60, 82–97]. However, the usefulness of those methods was also noted and we prescribed the conditions for the fundamental case of bubble growth that can be solved without relaxing the HRS assumptions. Based on the literature review presented in §(4.1) and through the work of Ryddner [100] & Anumolu [101] within our research group, it was identified that a physically correct, easy to implement, robust and scalable implementation of phase change is not readily available. Moreover, as identified in chapter 1, such a solver is a natural extension to the theoretical work on vapor bubble dynamics presented in chapter 2 and chapter 3. It will lead to the development of a necessary capability to study more complex vapor bubble systems for specific applications.

The phase change solver developed in this thesis describes the numerical solution for the

continuity and momentum equations, but leaves the solution of energy equation as part of future work. It includes a procedure to capture the deformation of an interface due to phase change in addition to the bulk flow and also describes a novel method to capture the velocity and pressure gradient discontinuities in a finite-volume framework. Importantly, the pressure gradient discontinuity is often ignored in previous studies. An analytical expression for the jump in pressure gradient has been derived as part of this thesis, its physical relevance is validated, and it has been included in the numerical discretization through the Pressure-Poisson equation.

The chapter is divided into four sections. The existing phase change HRS methods are first reviewed in  $\S(4.1)$ . This is followed by  $\S(4.2)$ , which provides a description of an incompressible two-phase flow solver without the capability of phase change, which is used as the basic solver for further development. Then the numerical method for interface advection and pressure-velocity solution related to phase change is presented in  $\S(4.3)$ . Finally, the coding algorithm and relevant tests are presented in  $\S(4.4)$ .

## 4.1 A Review of Phase Change Simulation Methods

A large part of the discussion related to phase change methods is on the correct implementation of the interfacial conditions, hence, at first these equations are established here [60],

$$\dot{m}'' = \rho_L \left( \mathbf{u}_{L,\Gamma} - \dot{\mathbf{x}}_{\Gamma} \right) \cdot \mathbf{n}_{\Gamma} = \rho_V \left( \mathbf{u}_{V,\Gamma} - \dot{\mathbf{x}}_{\Gamma} \right) \cdot \mathbf{n}_{\Gamma}, \tag{4.1a}$$

$$\llbracket p_d \rrbracket = (2\mu \llbracket \mathbf{E} \rrbracket) \cdot \mathbf{n}_{\Gamma} - \dot{m}'' \llbracket \mathbf{u} \rrbracket \cdot \mathbf{n}_{\Gamma} - \sigma \kappa_{\Gamma} + \llbracket \rho \rrbracket (\mathbf{g} \cdot \mathbf{x}), \quad \text{and}$$
 (4.1b)

$$h_{LV}\dot{m}'' = [\![k\nabla T]\!] \cdot \mathbf{n}_{\Gamma}. \tag{4.1c}$$

Here,  $\dot{\mathbf{x}}_{\Gamma}$  is the local rate of change in interface position,  $\mathbf{n}_{\Gamma}$  is the normal directed from liquid to vapor phase at the interface,  $\dot{m}''$  is the mass flux due to phase change,  $\llbracket \phi \rrbracket = \phi_{V,\Gamma} - \phi_{L,\Gamma}$  represents the difference between the two phases at the interface for any quantity  $\phi$ ,  $\mathbf{E}$  is the strain tensor given by  $(\nabla \mathbf{u} + \nabla \mathbf{u}^T)/2$ , and  $\kappa_{\Gamma}$  is the local curvature of the interface. Also,  $p_d = p - \rho(\mathbf{g} \cdot \mathbf{x})$  refers to the dynamic pressure, where  $\mathbf{g}$  refers to the gravitational acceleration or more generally, acceleration due to body forces. Note that the expressions in Eq. (4.1) are the generalized form of Eq. (2.8), Eq. (2.9), and Eq. (2.10), which were specialized for a spherically symmetric system of vapor bubble.

A correct phase change numerical method should satisfy Eq. (4.1), and evaluate property gradients ( $\nabla T$  and  $\nabla \mathbf{u}$ ) near the interface, while accounting for those jump conditions [60]. Several such computational methods have been proposed in the literature. For succinctness, these can be categorized based on the underlying scheme used for the advection of the liquid-vapor interface, broadly, Volume of Fluid (VoF) [83, 89, 90, 92, 93, 95, 96], Level Set (LS) [54, 58, 85–88], or Front-Tracking (FT) [82, 84, 97].

Among the early works on numerical simulations for phase change, Welch [44], and Son and Dhir [102] presented Lagrangian approaches to track the interface, but such methods

could not be scaled in cases of large deformations. Consequently, the focus shifted to the Eulerian based approach for phase change problem, and the first work in this regard may be attributed to Juric and Tryggvason [82]. They proposed a front-tracking method, where the interface is marked by several points. Its deformation is tracked by advecting and re-adjusting those points. Source terms were added to the underlying Eulerian fluid equations to simulate phase change. This method is known to be very complicated in terms of implementation and handling the rearrangement of the interface markers in cases of topological changes. Recent work by Irfan and Muradoglu [97] has extended the front-tracking phase change method to include cases where the mass transfer is due to species gradient. This is done by using the Clausius-Clapeyron equilibrium relation to evaluate vapor mass fraction near an interface and subsequently evaluating the resulting rate of mass flux.

Another early work on phase-change was published by Son and Dhir [103], who proposed a level-set based approach. In a level-set method, the interface is treated as a zero-level contour of a smooth, differentiable function defined over the entire domain. This function is taken to be a signed distance function, which is advected with the fluid flow. The discontinuous step change in the fluid velocity at the interface was handled by smoothing this change over several computational cells near the interface. This concept of smearing introduced by Son and Dhir [103] was contrary to the concept of the sharp interface [60] but due to the numerical stability obtained from this approach, several other authors have continued to use the 'smearing' concept [89, 90, 92, 104] to account for phase change. More recently, a number of level-set based phase change methods [54, 60, 105] have instead used a method called the Ghost Fluid Method to sharply capture interfacial discontinuities. As this method is used in the current work, it is discussed in more detail later in this section.

The third category of phase change methods has used the volume of fluid (VoF) method for the interface advection. The first VoF based phase change method was proposed by Welch and Wilson [83]. In VoF, phases are distinguished based on the fluid volume fraction  $(\alpha)$  in every computational cell. We follow the convention that  $\alpha=1$  for liquid and  $\alpha=0$  for vapor. For an interfacial cell,  $\alpha$  assumes a value in the range (0,1). The  $\alpha$  value changes sharply near the interface from a value of 0 to 1. In the solution of the momentum equation, the discontinuity of the velocity field, the velocity gradients, and the viscosity due to phase change were treated in [83] by smearing the change over several computational cells. A recent methodology based on the interface reconstruction using an iso-surface of  $\alpha=0.5$  was developed by Tsui and Lin [95] to solve for phase change. In this method, while density and viscosity were still treated as smeared variables, thermal properties were treated sharply and one-sided temperature gradients were obtained to evaluate the rate of mass flux due to phase change.

An algebraic method similar to VoF was used by Sato and Ničeno [93] to propose a phase change solver, where they used a color function  $(0 \le c \le 1)$  to advect the interface (c = 0.5) using the constrained interpolation profile (CIP) method [106]. The method used a source term to account for the motion of interface due to phase change, and in the energy equation. In their work, they combine a finite volume formulation for the bulk fluids and finite-difference formulation close to the interface for the temperature equation. While it was noted that the velocity jump is handled sharply, the method used to capture this jump through the pressure-velocity coupling using the Chorin projection [107] method was not explicitly explained. This method has been used by the same authors for studying nucleate boiling [108], pool boiling [109], and flow boiling [110] problems.

Prominently, two methods have been used in previous literature to account for the discontinuities at the liquid-vapor interface: smoothing/smearing, or Ghost Fluid Method. The latter is physically more accurate and its implementation has been extensively discussed for the finite-difference formulation of the Navier - Stokes equations, which are used in the level-set methods. However, the extension of level set methodologies to more realistic non-orthogonal grids is very challenging. Instead, finite volume methods such as the VoF technique can be extended more easily. The OpenFOAM solver, which will be used in this thesis also has existing VoF based solvers that can be further developed to include the capability for phase change. Hence, this thesis describes the development of the Ghost Fluid Method for a finite volume method of phase change. Before proceeding, the following sub-section reviews the important pieces of literature related to GFM.

#### Review of Ghost fluid method

This method was first introduced in the work of Fedkiw et al. [111] within a Level-Set based fluid flow solver to sharply capture material discontinuities exhibited at the liquid-vapor phase interface. The initial development was motivated by a need to eliminate spurious currents that arose due to the smearing of the interface discontinuities. In this method, the liquid phase is assumed to extend beyond the interface into the vapor phase as a ghost fluid. Liquid values are populated in this ghost region by some form of extrapolation, either using a normal-wise constant extrapolation approach or by Taylor series expansion that accounts for the discontinuities. Similarly, ghost vapor is also defined for liquid points in the domain. Such an extension leads to two continuous fields in the domain, one pertaining to the liquid

phase and the other related to the vapor phase. Consequently, the phase-specific gradients that need to be calculated close to the interface can be evaluated directly.

While this method has been used extensively in finite-difference methods, finite volume techniques have only recently begun to apply GFM. A recent work by Vukčević et al. [112] used GFM to capture the dynamic pressure  $(p_d)$  discontinuity related to gravitational forces. The implementation was done within an algebraic VoF solver within the OpenFOAM framework. It delineated the fundamental idea that all cells (including mixture cells with  $0 < \alpha < 1$ ) are treated either as a pure liquid or vapor cell when writing the discrete form of the momentum equation. In doing so, the pressure gradients evaluated at the faces of interfacial computational cells have to be corrected to include the appropriate pressure jump using the ghost fluid approach. Similarly, another study that was published as a short note by Haghshenas et al. [113] implemented GFM to capture the pressure jump related to surface tension. This was done within a Coupled Level Set-Volume of Fluid framework (CLSVoF), where the value of curvature was determined from the level set.

For phase change problems, which is the focus of this thesis, the first use of GFM was in the work of Nguyen et al. [56], where they extended the capture of material discontinuities at the interface to the jump in velocity field at the interface. Interestingly, to obtain a relation between vapor and liquid pressure gradients near the interface, they used the nonconservative form of the momentum equation to argue that the momentum equation remains continuous across the interface even with phase change, without sufficient justification. This assumption led to the following relation for liquid and vapor pressure gradients near the interface,

$$\left(\frac{\nabla p_L}{\rho_L}\right)_{\Gamma} \cdot \mathbf{n}_{\Gamma} = \left(\frac{\nabla p_V}{\rho_V}\right)_{\Gamma} \cdot \mathbf{n}_{\Gamma}. \tag{4.2}$$

This relation along with Eq. (4.1b) served as the interfacial conditions for pressure to develop the ghost fluid extrapolation across the interface based on the work of Liu et al. [114]. Following [56], phase change methods that employed Ghost Fluid method to handle interface discontinuity [54, 57–60] continued the use of Eq. (4.2) in the solution of the Poisson equation for pressure. These methods largely focused on improvements in the ghost fluid extension of velocity and the use of improved advection schemes.

However, the velocity discontinuity observed due to phase change at the interface breaks the continuity of the momentum equation and Eq. (4.2) no longer holds. Even for a simple case of spherical vapor bubble, using the well-known analytical expression for  $p_L(\mathbf{x},t)$ ,  $p_V(\mathbf{x},t)$ ,  $\mathbf{u}_L(\mathbf{x},t)$ , and  $\mathbf{u}_V(\mathbf{x},t)$  [8, 10], it can be shown that pressure gradient suffers a jump along the radial coordinate at the bubble surface (shown in §(B.3)). This shortcoming of existing phase change methods is overcome in §(4.3.2) by incorporating a jump in pressure gradient at the interface due to phase change and implementing the concept of Ghost Fluid Method in a finite volume scheme, similar to the aforementioned work of Vukčević et al. [112].

## 4.2 Framework for Phase Change Solver Development

For this work, the open-source framework of OpenFOAM v1706+ [115] was chosen for its coding-friendly paradigms, plenty of online resources, and extensive in-house experience with these libraries [116, 117]. The *interIsoFoam* solver within this version of OpenFOAM is used as the base two-phase solver for the development of phase change capability within it. Comprehensive testing done for *interIsoFoam* is presented below.

### Testing the performance of base solver: interIsoFoam

For assessing the performance of, interIsoFoam, several tests are presented in this section. Its results are compared against the more widely used interFoam solver, which has been in use within our group for over a decade and has been thoroughly tested for its accuracy and robustness [118]. The fundamental difference between the two solvers is related to the advection of liquid volume fraction,  $\alpha$ , which implicitly tracks the deformation of the interface.

The *interIsoFoam* solver [119] is based on a geometric VoF methodology that explicitly performs a geometric reconstruction of the interface and tracks its motion over time to evaluate the advection of liquid volume across the boundaries of a computational cell. In contrast, the *interFoam* solver incorporates an algebraic manipulation in the advection equation for  $\alpha$  that serves to limit the diffusion of  $\alpha$  field close to the interface and somewhat preserve the sharpness of a liquid-vapor interface. While it results in a stable and easily scalable algorithm, a major drawback with the *interFoam* solver is the absence of a sharp location of the interface (available in the *interIsoFoam* algorithm), which is substituted with an interfacial region that spans over several computational cells.

In the following comparison, results from interFoam will be referred to as aVoF, which stands for algebraic volume of fluid method, and results from interIsoFoam will be referred to as gVoF which stands for geometric volume of fluid method.

### 4.2.1 Advection Tests

In this section, we exclusively analyze the performance of the liquid volume fraction advection equation given by,

$$\frac{\partial \alpha}{\partial t} + \int_{\partial \Omega_i} \mathbb{I} \left( \mathbf{u} \cdot \mathbf{n} \right) dS = 0. \tag{4.3}$$

Here,  $\mathbf{u}$  represents the velocity,  $\mathbf{n}$  represents the normal pointing outwards from the control volume, and  $\mathbb{I}$  represents the indicator function, given by,

$$\mathbb{I}(\mathbf{x},t) = \begin{cases}
1 & \mathbf{x} \in \text{Liquid} \\
0 & \mathbf{x} \in \text{Vapor}
\end{cases}
\Rightarrow \chi(\mathbf{x},t) = \chi_L \mathbb{I}(\mathbf{x},t) + \chi_V (1 - \mathbb{I}(\mathbf{x},t)), \qquad (4.4)$$

where  $\chi$  represents any physical quantity.

The problem with solving a hyperbolic equation such as Eq. (4.3) lies in the evaluation of the second term on the left-hand side of the equation referred to as the advection term. As briefly explained above, this evaluation of liquid flux through a computational volume is done in *interIsoFoam* by first approximating a geometric reconstruction of the sub-grid interface, and then subsequently tracing its sub-grid movement at the computational volume boundaries during a time step. Conceptually, this method is similar to the popular PLIC geometric VoF scheme [120–123], but the reconstruction and time-evolution of the interface

slightly differ from the traditional method.

In PLIC, the interface is oriented using normals calculated from volume fraction gradient, and then located such that the cell liquid fraction is satisfied. The first step that includes the calculation of interface normal itself introduces error in the formulation. In the new method implemented in *interIsoFoam*, an interpolation of the  $\alpha$  field on each cell-edge is done to reconstruct an iso-surface that cuts the cell into liquid and vapor volumes that correspond with the volume fraction of the cell [119]. This reconstruction of iso-surface is independently done in each of the interfacial cells, without the need to orient the interface with respect to a separately calculated interface normal direction.

Tests on the implemented solution for Eq. (4.3) in *interIsoFoam* are shown in this section for simple geometries that undergo interface deformation under a prescribed velocity field. No velocity-pressure solutions are obtained in these tests. The velocity fields are prescribed such that the object should ideally retain its original position and shape at the end of simulation time. This provides an easy benchmark to compare the final volume fraction field with the initial state and find the error that is induced only due to the inaccuracy of the  $\alpha$  advection methodology.

#### Notched Disk: Pure Rotation

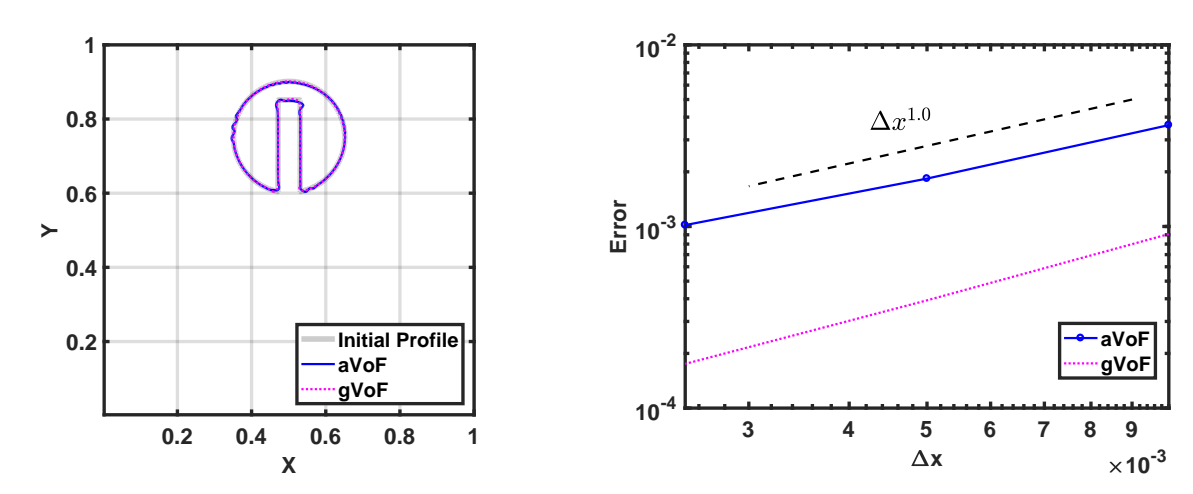
This is a popular case used in several other papers as the first test of their interface advection scheme. The initial geometry consists of a circular object in a square domain ( $[0,1] \times [0,1]$ ). The circular object has a rectangular notch and the shape is shown in figure 4.1a. The center of the circle is kept at (0.5, 0.75), and its radius is 0.15, while the notch width is 0.06, and the top-most edge of the notch is at y = 0.85. This disk undergoes a pure rotation around

the center of the domain and should ideally come back to its original position, where the prescribed velocity is given by,

X-Velocity, 
$$u = -\frac{\pi}{3.14} (y - 0.5)$$
, and (4.5a)

Y-Velocity, 
$$v = \frac{\pi}{3.14} (x - 0.5)$$
. (4.5b)

Error metric used for this test is given by,



(a) Comparison of  $\alpha = 0.5$  contour for grid size - (b) Error in the final  $\alpha$  field compared to initial  $400 \times 400$  setup as described in Eq. (4.6).

Figure 4.1: Results for Notched Disk Advection.

$$Error = \left(\sum_{i \in All \text{ cells}} A_i \left| \alpha_{i,final} - \alpha_{i,initial} \right| \right), \tag{4.6}$$

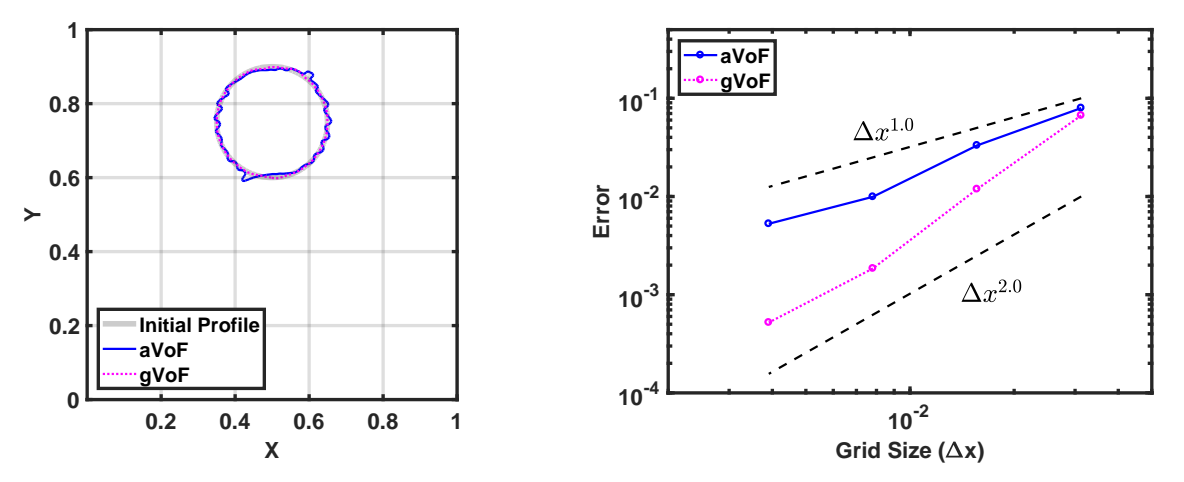
where error between the initial and final volume fraction field is integrated over the entire 2-D domain. Both the qualitative visual result in figure 4.1a and the quantitative error in figure 4.1b show that the performance of the *interIsoFoam* solver is superior when compared to the *interFoam* solver.

#### Two-Dimensional Vortex: Highly Deforming Interface

This test is designed to test advection performance where an interface severely deforms from an initial circular disk under a vortex field. After achieving maximum deformation the velocity field is reversed such that the object should attain its original position after one complete period. In a square domain ( $[0,1] \times [0,1]$ ) an initial circular disk of radius 0.15 is centered at (0.5, 0.75). The deformation velocity field is,

$$\mathbf{u} = (u, v) = \left(\sin^2(\pi x)\sin(2\pi y)\cos\left(\frac{\pi t}{8}\right), -\sin^2(\pi y)\sin(2\pi x)\cos\left(\frac{\pi t}{8}\right)\right). \tag{4.7}$$

The contour obtained from geometric VoF retains the original shape of the circle more



(a) Comparison of  $\alpha = 0.5$  contour for grid size (b) Er  $256 \times 256$ 

(b) Error in the final  $\alpha$  field compared to initial setup as described in Eq. (4.6).

Figure 4.2: Results for 2-D Vortex Deformation Advection.

accurately than the algebraic VoF as shown in figure 4.2a. Quantitatively, the error in the  $\alpha$  field decreases more significantly for the geometric VoF method on the refinement of the mesh.

### 4.2.2 Surface Tension and Pressure Velocity Coupling Tests

Momentum equation in a whole domain formulation of two phase flows is given by,

$$\int_{\Omega_{i}} \frac{\partial \rho \mathbf{u}}{\partial t} dV + \int_{\partial \Omega_{i}} \rho \mathbf{u} \left( \mathbf{u} \cdot \mathbf{n} \right) dS = -\int_{\Omega_{i}} \nabla p_{d} dV - \int_{\Omega_{i}} \left( \mathbf{g} \cdot \mathbf{x} \right) \nabla \rho dV + \int_{\Omega_{i}} \sigma \kappa \nabla \alpha dV \quad (4.8)$$

$$+ \int_{\partial \Omega_{i}} (\mu \nabla \mathbf{u}) \cdot \mathbf{n} dS + \int_{\partial \Omega_{i}} (\nabla \mathbf{u} \cdot \nabla \mu) dS,$$

The above equation is repeated from the work of Deshpande et al. [116].

The solution for Eq. (4.8) is performed by the Chorin projection method [124]. First, an intermediate velocity field is constructed without considering pressure term, and then the resulting velocity field is corrected using the Pressure Implicit with Splitting of Operators (PISO) [125] method. It is an implicit pressure correction procedure to time advance the pressure. The interested reader is referred to Deshpande et al. [116] for explicit numerical details of the method.

Both density and viscosity used in the solution of the momentum equation are given by,

$$\rho_i^n = \alpha_i^n \rho_L + (1 - \alpha_i^n) \rho_V, \quad \text{and}$$
(4.9)

$$\mu_i^n = \alpha_i^n \mu_L + (1 - \alpha_i^n) \mu_V, \tag{4.10}$$

where i refers to the computational cell index, and n refers to the time step-index. Equation (4.10) shows that the change in density and viscosity happens continuously over an interfacial region rather than discontinuously at the interface.

The surface tension term in Eq. (4.8) is calculated using the Continuum Surface Force

(CSF) model in both *interFoam* and *interIsoFoam* solvers, which is given by,

$$\mathbf{n} = \nabla \alpha, \tag{4.11}$$

$$\kappa_{\Gamma} = \nabla \cdot \mathbf{n} = \nabla \cdot \nabla \alpha, \quad \text{and}$$
 (4.12)

$$\Delta P = \sigma \left( \nabla \cdot \nabla \alpha \right). \tag{4.13}$$

Laplacian of the liquid volume fraction field in any VoF scheme will naturally result into non-zero values over several computational cells. Again, Eq. (4.13) suggests that a smoothed profile of change in pressure due to surface tension is implemented in the OpenFOAM framework.

Regarding the comparative study here, the key difference between the test solver *inter-IsoFoam* and the benchmark solver *interFoam* lies in the volume fraction field. The time evolution of  $\alpha$  from both methodologies is different, which will directly affect the evaluation of density & viscosity and consequently the pressure-velocity solution for momentum equation obtained from the PISO loop.

#### **Interfacial Curvature Calculation**

Here, an initial system is set up with a simple droplet of radius, R = 0.25 kept at the center of a square domain of span  $[0,1] \times [0,1]$ . The two phases have identical properties of  $\rho = 10^4$ , and  $\mu = 1$ , while the surface tension at the droplet interface is set at  $\sigma = 1$ . The curvature of a 2-D shape is simply given by 1/R, and hence, the analytical value of curvature is equal to 4. Correspondingly, the pressure jump across the surface should be equal to  $\sigma \kappa = 4$ . Comparison of this analytical value to the value computed from the *interIsoFoam* and

interFoam solvers is shown below.

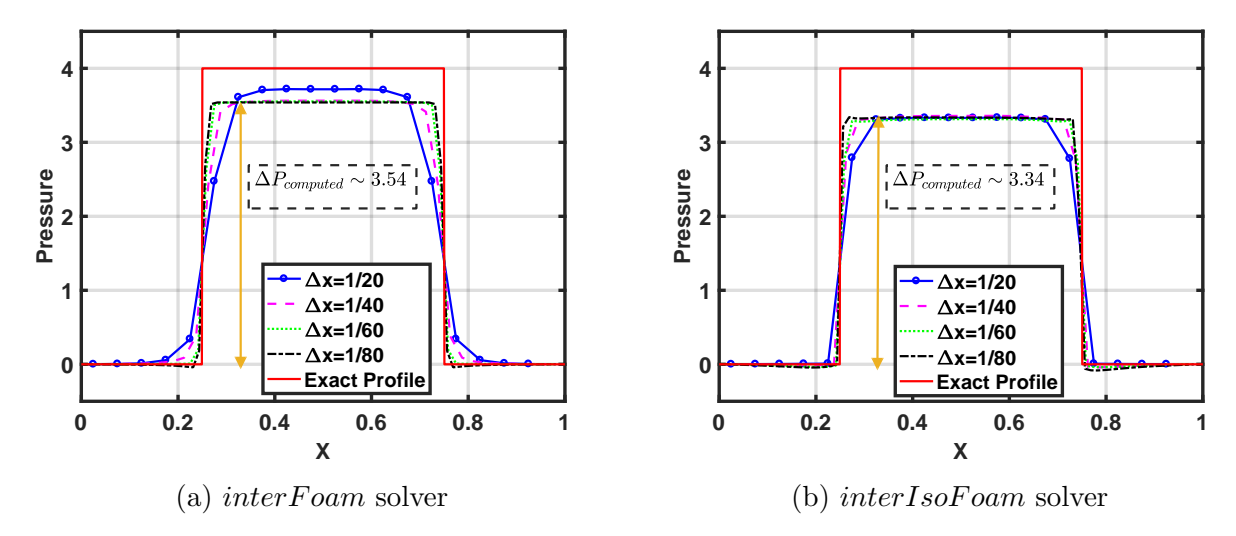


Figure 4.3: Evaluation of Pressure Jump from at different grid sizes.

In figure 4.3b, the pressure jump occurs across one cell for the *interIsoFoam* solver based on geometric VoF, while the pressure jump occurs over at least 2 cells in the *interFoam* results. The former is more in line with the sharper treatment of the interface as described in  $\S(4.1)$ . However, it is also evident that the computed pressure jump has a higher error in the geometric VoF method than the algebraic method. As the variation of  $\alpha$  in gVoF occurs more sharply, it results in greater error in calculating the divergence of its gradient used in Eq. (4.13).

#### Standing Capillary Wave

The two-phase setup for this case is shown in figure 4.4. The horizontal dimension of the domain is  $10^{-4}$  m and the vertical dimension is  $5 \times 10^{-4}$  m. As shown in the figure, an initial perturbation of wavelength  $\lambda = 10^{-4}$  is added to the liquid-gas interface, which has an amplitude,  $a = \lambda/20 = 0.05 \times 10^{-4}$ . Density of liquid and vapor phases are 1 kg/m<sup>3</sup> and 999 kg/m<sup>3</sup> respectively, while kinematic viscosity is equal to 0 and  $10^{-6}$  m<sup>2</sup>/s. The left and

right walls have a cyclic boundary condition as shown in figure 4.4, while the top and bottom sides are simply treated as constant pressure, and zero velocity gradients.

	aVoF		gVoF		
	$ au_{aVoF}$	$ \tau_{aVoF} - \tau_{osc} /\tau_{osc} \times 100$	$ au_{gVoF}$	$ \tau_{gVoF} - \tau_{osc} /\tau_{osc} \times 100$	
$\lambda/\Delta x = 5$	$3.702 \times 10^{-5}$	55.285%	$3.152 \times 10^{-5}$	32.201%	
$\lambda/\Delta x = 20$	$2.473 \times 10^{-5}$	3.747%	$2.487 \times 10^{-5}$	4.31%	
$\lambda/\Delta x = 30$	$2.444 \times 10^{-5}$	2.517%	$2.476 \times 10^{-5}$	3.859%	
$\lambda/\Delta x = 40$	$2.436 \times 10^{-5}$	2.181%	$2.453 \times 10^{-5}$	2.908%	

Table 4.1: Error in calculation of oscillation time period for standing capillary wave.

Due to the difference in densities, the interface undergoes periodic oscillations that are eventually damped out due to the liquid viscosity. The results are compared to the analytical solution as shown in the test cases of Deshpande et al. [118]. The analytical solution is given by,

$$\omega_{osc} = \sqrt{\frac{\sigma \kappa^3}{\rho_l + \rho_g}}, \text{ where } \kappa = \frac{2\pi}{\lambda}.$$
 (4.14)

For this case, analytical period of oscillation given by,

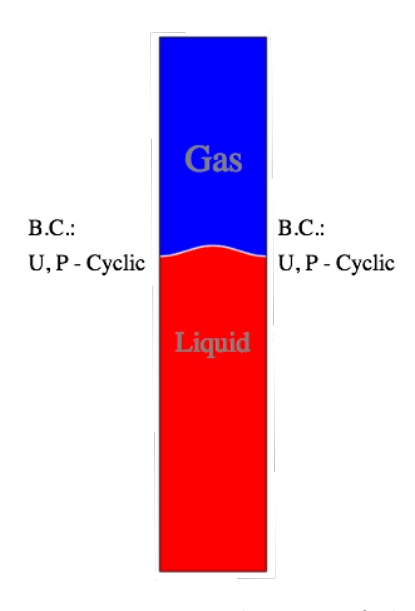


Figure 4.4: Initial setup of the standing capillary wave test.

$$\tau_{osc} = \frac{1}{2} \frac{2\pi}{\omega_{osc}} = 2.384 \times 10^{-5} \text{ s},$$
(4.15)

which is compared with the numerical period of oscillation obtained as an average of 10 cycles.

Results in table 4.1 show that for the coarsest grid of 5 grid cells across the wavelength,

both aVoF, and gVoF methods perform poorly, and the former has a higher magnitude of error. A significant improvement in the results is observed for  $\lambda/\Delta x = 20$  for both methodologies and the rate of decrease in error on further refinement of the grid is small. The test shows that the geometric volume of fluid implementation in interIsoFoam has a comparable performance compared to the well-established algebraic volume of fluid, interFoam solver for surface tension dominated dynamic test cases.

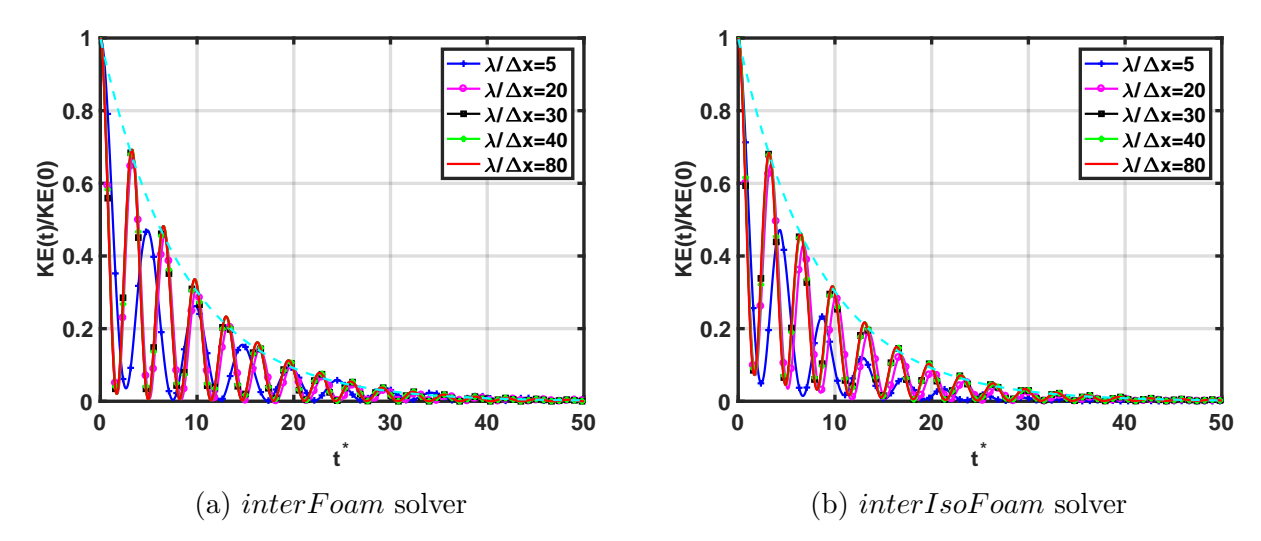


Figure 4.5: Time variation of kinetic energy in the domain for a standing capillary wave test case.

#### Rising Bubbles due to Buoyancy

Keeping in mind the final application intended for the *interIsoFoam* solver, the final test case is chosen to be directly related to bubble dynamics. The following tests are done for pressure-velocity coupling in case of rising gas bubble under the effect of buoyancy. Here, we present a comparison between the experimental results of Bhaga and Weber [126] and the numerical results obtained from the *interIsoFoam* solver for rising air bubbles in water-sugar solution column similar to previous numerical works [84, 106, 127–131]. The solution

concentration was varied to obtain different values of the following non-dimensional numbers [126],

Reynolds Number, 
$$Re = \frac{\rho DU}{\mu}$$
, (4.16a)

Eötvös Number, 
$$Eo = \frac{gD^2\rho}{\sigma}$$
, and (4.16b)

Morton Number, 
$$Mo = \frac{g\mu^4}{\rho\sigma^3}$$
. (4.16c)

				Present Work		Magnini [132] Results	
Case	Eo	Mo	$Re_{experimental}$	$Re_{calculated}$	$\Delta Re$	$Re_{calculated}$	$\Delta Re$
a	116	848	2.47	2.33	5.66 %	2.37	4 %
b	116	41.1	7.16	6.96	2.79 %	6.94	3.1 %
С	116	1.3	20.4	19.51	4.36 %	19.55	4.2 %
d	116	0.103	42.2	38.58	8.58 %	39	7.6 %

Table 4.2: Test cases for bubbles rising in liquid columns of different liquid properties.

The system setup is obtained from Magnini [132]. A gas bubble of diameter D is centered at [0, 2D] in an axisymmetric domain that spans  $[0, 4D] \times [0, 12D]$ . The grid size is kept fixed for all cases at  $80 \times 240$ . Density ratio between vapor and liquid was kept at 1000, and viscosity ratio as 100. Values of the Eo, and Mo were varied for different cases and the computed Re value of the bubble are logged in table 4.2. Difference of the computed values from experimental data are shown as  $\Delta Re$ .

Reynolds number obtained for the terminal velocity of the bubble from the present calculations are within 10% of the experimental values. Also, the results match very well with a similar numerical methology used by [132], where they use PLIC method of geometric reconstruction in the volume of fluid algorithm.

The results presented above show that *interIsoFoam* is a stable two phase flow solver

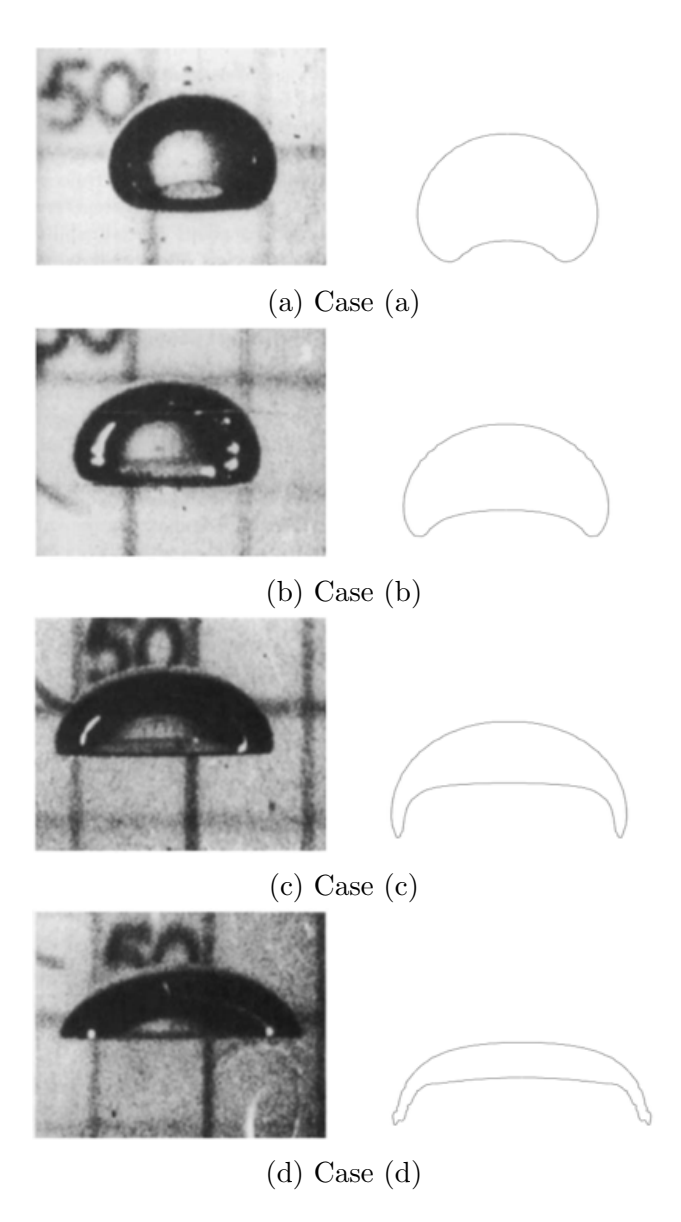


Figure 4.6: Test cases for bubbles rising in liquid columns of different liquid properties. Experimental pictures on the left [126] and results from interIsoFoam solver on the right.

with the ability to provide information about the sub-grid interface location. This property is useful in implementing the capability to handle phase change phenomenon, which results in velocity, pressure gradient and temperature gradient discontinuity at the interface.

## 4.3 Phase Change Numerical Method Development

To add the capability of phase change in the interIsoFoam solver, following equations must be modified or added to the solver:

- Interface advection:  $\alpha$  equation
- Momentum: Chorin projection and Pressure-Poisson equation
- Temperature: Energy equation
- Mass Flux: Rate of phase change at the interface evaluated from Eq. (4.1c)

In this thesis, methods related to the first two aspects of a phase change solver, namely, advection and momentum equations have been presented. It includes the critical component related to capturing the velocity discontinuity at the interface.

## 4.3.1 Alpha Equation

The liquid volume fraction advection equation given by Eq. (4.3) only accounts for the interface motion that occurs along with the bulk flow. This needs to be modified for a flow with phase change due to two reasons:

- 1. The velocity field has a discontinuity at the interface, which is absent in flows without phase change.
- 2. Besides interface advection with the flow, there is an additional motion of the interface due to the phase change process.

To derive a generalized equation for the advection of liquid volume fraction, we begin with the integral form of continuity equation given by Eq. (B.5), specialized for mass with  $\psi = \rho$ . This is given by,

$$\frac{\mathrm{d}}{\mathrm{d}t} \int_{\Omega} \rho dV = \frac{\mathrm{d}}{\mathrm{d}t} \int_{\Omega_i} \rho dV + \int_{\partial \Omega_i} \rho \mathbf{u} \cdot \mathbf{n} dS, \tag{4.17}$$

where the integral on left hand side represents the time rate of change in the mass of a material volume, first term on the right hand side represents the time rate of change in the mass for a control volume that coincides with the material volume at an instant of time t, and the last term represents the mass flux across the bounding surface. By definition, L.H.S. = 0 and the equation reduces to,

$$\frac{\mathrm{d}}{\mathrm{d}t} \int_{\Omega_i} \rho dV + \int_{\partial\Omega_i} \rho \mathbf{u} \cdot \mathbf{n} dS = 0. \tag{4.18}$$

Using the indicator function,  $\mathbb{I}$ , given by Eq. (4.4), density at any point,  $\mathbf{x}$ , in the domain can be expressed in terms of liquid and vapor densities. Rewriting Eq. (4.18) in terms of  $\rho_L$  and  $\rho_V$ , we get,

$$\frac{\mathrm{d}}{\mathrm{d}t} \int_{\Omega_{i}} \left( \rho_{L} \mathbb{I} + \rho_{V} \left( 1 - \mathbb{I} \right) \right) dV + \int_{\partial \Omega_{i}} \left( \rho_{L} \mathbb{I} + \rho_{V} \left( 1 - \mathbb{I} \right) \right) \mathbf{u} \cdot \mathbf{n} dS = 0. \tag{4.19}$$

Collecting the indicator function terms on one side, we get,

$$(\rho_L - \rho_V) \left( \frac{\mathrm{d}}{\mathrm{d}t} \int_{\Omega_i} \mathbb{I} dV + \int_{\partial \Omega_i} \mathbb{I} \mathbf{u} \cdot \mathbf{n} dS \right) = -\underbrace{\frac{\mathrm{d}}{\mathrm{d}t} \int_{\Omega_i} \rho_V dV}_{=0} - \underbrace{\int_{\partial \Omega_i} \rho_V dV}_{=0} - \underbrace{\int$$

Phase densities,  $\rho_V$  and  $\rho_L$  are assumed to remain constant in writing Eq. (4.20), which can be further rearranged as,

$$\frac{\mathrm{d}\alpha}{\mathrm{d}t} + \int_{\partial\Omega_i} \mathbb{I}\mathbf{u} \cdot \mathbf{n}dS = -\frac{\rho_V}{(\rho_L - \rho_V)} \int_{\partial\Omega_i} \mathbf{u} \cdot \mathbf{n}dS, \tag{4.21}$$

where,  $\alpha = \int_{\Omega_i} \mathbb{I} dV$ . For cases without phase change, the divergence of velocity on R.H.S. is zero even for interfacial cells. Equation (4.21) would be identical to Eq. (4.3) in that case. However, due to Eq. (4.1a), the divergence of velocity over a control volume is no longer zero for interfacial cells.

A derivation for the divergence of velocity for a control volume containing the interface in a flow with phase change was presented in §(B.2) and given by Eq. (B.12). Substituting Eq. (B.12), Eq. (4.21) can be rewritten as,

$$\frac{\mathrm{d}\alpha}{\mathrm{d}t} + \int_{\partial\Omega_i} \mathbb{I}\mathbf{u} \cdot \mathbf{n} dS = -\frac{\rho_V}{(\rho_L - \rho_V)} \left(\frac{1}{\rho_V} - \frac{1}{\rho_L}\right) \int_{\Gamma} \dot{m}'' dS. \tag{4.22}$$

Another important modification needed for  $\alpha$  advection with phase change is related to the velocity that is used to advect this quantity. The general variable  $\mathbf{u}$ , which remains continuous for cases without phase change no longer holds that property due to the velocity discontinuity in phase change problems. Rewriting,  $\mathbf{u}$  in terms of  $\mathbf{u}_L$  and  $\mathbf{u}_V$  using the indicator function distinctly identifies the vapor and liquid velocity, which is physically accurate at the interface. Using such a relation in Eq. (4.22) and simplifying R.H.S. gives,

$$\frac{\mathrm{d}\alpha}{\mathrm{d}t} + \int_{\partial\Omega_{\epsilon}} \mathbb{I}\left(\mathbf{u}_{L}\mathbb{I} + \mathbf{u}_{V}\left(1 - \mathbb{I}\right)\right) \cdot \mathbf{n}dS = -\frac{1}{\rho_{L}} \int_{\Gamma} \dot{m}'' dS. \tag{4.23}$$

Considering,  $\mathbb{I}(\mathbf{x},t)\mathbb{I}(\mathbf{x},t) = \mathbb{I}(\mathbf{x},t)$  and  $\mathbb{I}(\mathbf{x},t)(1-\mathbb{I}(\mathbf{x},t)) = 0$ , the final reduced form of this equation is given by,

$$\frac{\mathrm{d}\alpha}{\mathrm{d}t} + \int_{\partial\Omega_i} \mathbb{I}\left(\mathbf{u}_L \cdot \mathbf{n}\right) dS = -\frac{1}{\rho_L} \int_{\Gamma} \dot{m}'' dS. \tag{4.24}$$

Different from Eq. (4.3) used in the original solver without phase change, the advection of liquid volume fraction in this phase-change formulation is performed with the liquid velocity as it forgoes the notion of a general velocity that describes the entire domain. Also, the additional motion of interface due to phase change is included in the source term given by the right hand side of Eq. (4.24).

#### 4.3.1.1 Numerical Solution of Alpha Equation

In the implemented solver, Eq. (4.24) is written for each discrete computational cell as,

$$\alpha_i^{n+1} = \alpha_i^n + \sum_{f \in \text{Cell Faces}} \left( \frac{\phi_{L,f}^n}{|\mathbf{S}_f|} \int_t^{t+\Delta t} \int_f \mathbb{I} dS dt \right) - \frac{1}{\rho_L} \int_t^{t+\Delta t} \int_{\Gamma} \dot{m}'' dS dt. \tag{4.25}$$

Here, the superscript n refers to the previous time step for which the velocity, liquid volume fraction, and mass flux fields are known. The superscript n+1 refers to the time step for which  $\alpha$  needs to be evaluated through Eq. (4.25). In writing Eq. (4.25), we have assumed that face volume flux,  $\phi_{L,f} = \mathbf{u}_{L,f} \cdot \mathbf{S}_f$  remains a constant for the time step  $\Delta t$ . This assumption is similar to the solution taken without phase change in the *interIsoFoam* solver [119].

Using the same notation as used in [119], the advection integral can be written in terms of  $A_f = \int_f \mathbb{I} dS$ , which refers to the face area submerged in liquid at a given instant of time.

We can further assume that mass flux due to phase change for a given interfacial cell is uniform and constant for time step  $\Delta t$ . This reduces Eq. (4.25) to,

$$\alpha_i^{n+1} = \alpha_i^n + \sum_{f \in \text{Cell Faces}} \left( \frac{\phi_{L,f}^n}{|\mathbf{S}_f|} \int_t^{t+\Delta t} A_f dt \right) - \frac{(\dot{m}'')_i^n}{\rho_L} A_{\Gamma,i}^n \Delta t, \tag{4.26}$$

where  $A_{\Gamma,i}$  represents the area of the sub-grid reconstruction of the interface. The evaluation of  $A_f$  and its time integral remains unmodified from the solution of *interIsoFoam* as presented in detail in [119]. Equation (4.26) serves as the first step in the advection of  $\alpha$ .

The resultant  $\alpha$  field is not bounded, however. The source term in Eq. (4.26) allows the value of  $\alpha$  in some computational cells to overshoot its maximum value of 1 or undershoot the minimum value of 0. In the original implementation in *interIsoFoam*, this step of  $\alpha$  advection is handled by transferring the additional fluid volume to downwind cells by using the volume flux values at the faces. We employ a similar strategy, albeit, with some needed modifications. The flux values used for  $\alpha$  advection in Eq. (4.26) correspond with the liquid flux. These values do not reflect the additional volume that is generated due to phase change and only represent the bulk liquid flow.

Hence, for this step we reformulate the  $\alpha$  equation starting from Eq. (4.21). Here, instead of substituting Eq. (B.12) on the R.H.S., velocity on the R.H.S. is also written in terms of  $\mathbf{u}_L$  and  $\mathbf{u}_V$ . The resulting expression is given by,

$$\frac{\mathrm{d}\alpha}{\mathrm{d}t} + \int_{\partial\Omega_{i}} \mathbb{I}\left(\mathbf{u}_{L}\mathbb{I} + \mathbf{u}_{V}\left(1 - \mathbb{I}\right)\right) \cdot \mathbf{n}dS = -\frac{\rho_{V}}{(\rho_{L} - \rho_{V})} \int_{\partial\Omega_{i}} \left(\mathbf{u}_{L}\mathbb{I} + \mathbf{u}_{V}\left(1 - \mathbb{I}\right)\right) \cdot \mathbf{n}dS. \quad (4.27)$$

Combining  $\mathbf{u}_L$  terms and  $\mathbf{u}_V$  terms separately on the R.H.S., we get,

$$\frac{\mathrm{d}\alpha}{\mathrm{d}t} = -\left(1 + \frac{\rho_V}{\rho_L - \rho_V}\right) \int_{\partial\Omega_i} \mathbb{I}\left(\mathbf{u}_L \cdot \mathbf{n}\right) dS - \frac{\rho_V}{\rho_L - \rho_V} \int_{\partial\Omega_i} \mathbf{u}_V \cdot \mathbf{n} dS + \frac{\rho_V}{\rho_L - \rho_V} \int_{\partial\Omega_i} \mathbb{I}\mathbf{u}_V \cdot \mathbf{n} dS.$$

$$(4.28)$$

Second term on R.H.S. is equal to zero due to vapor incompressibility ( $\int_{\partial\Omega_i} \mathbf{u}_V \cdot \mathbf{n} dS = 0$ ). Note that this step assumes that vapor velocity is populated on faces of interfacial computational cells, which may be completely submerged in the liquid face. Hence, the assumption inherently implies that fictional values populated for vapor beyond the interface also follow the incompressibility condition. On further simplifying Eq. (4.28), it is reduced to,

$$\frac{\mathrm{d}\alpha}{\mathrm{d}t} = -\int_{\partial\Omega_i} \mathbb{I}\left(\underbrace{\left(\frac{\rho_L}{\rho_L - \rho_V} \mathbf{u}_L - \frac{\rho_V}{\rho_L - \rho_V} \mathbf{u}_V\right)}_{\text{Effective face velocity}} \cdot \mathbf{n}\right) dS. \tag{4.29}$$

Using this effective face velocity, we evaluate an effective face flux given as,

$$\phi_{Effective,f}^{n} = \left(\frac{\rho_{L}}{\rho_{L} - \rho_{V}} \mathbf{u}_{L,f}^{n} + \frac{\rho_{V}}{\rho_{L} - \rho_{V}} \mathbf{u}_{V,f}^{n}\right) \cdot \mathbf{n} \left|\mathbf{S}_{f}\right|, \tag{4.30}$$

which is used to advect the additional volume obtained from the overfill or underfill.

The author would like to note that Eq. (4.29) has been derived with no major assumptions besides bulk-phase incompressibility of liquid and vapor. Hence, Eq. (4.30) can ideally be used directly to advect  $\alpha$ . However, in practice,  $\phi_{Effective}$ , that employs the values of both  $\mathbf{u}_L$  and  $\mathbf{u}_V$ , is physically inconsistent for faces, which are completely submerged in liquid or vapor. Switching between  $\phi_L$  and  $\phi_{Effective}$  depending on the instantaneous state of a face

(completely submerged in liquid/vapor or intersected by the interface) requires complicated book-keeping. Hence, it is only invoked for cases where the computational cell overshoots or undershoots.

Finally, the evolution of  $\alpha$  is composed of two parts:

- 1. At first,  $\alpha$  is advected using Eq. (4.26). The flux value in advection term, represented by  $\phi_{L,f}$  refers to the volume flux associated with liquid bulk velocity.
- 2. The second step uses Eq. (4.30), which defines an effective volume flux, to transfer additional fluid volume from computational cells that have  $\alpha > 1$  or  $\alpha < 0$ .

## 4.3.2 Pressure - Velocity Coupling (Ghost Fluid Method)

After the interface advection, the density and viscosity values at cell centers is updated using the new values of  $\alpha$ . A whole-domain formulation is traditionally used for the solution of momentum equation in the base, interIsoFoam solver, which uses the volume averaged value of  $\rho$  and  $\mu$ . This formulation is not consistent with the velocity discontinuity, characteristic of a two-phase flow with phase change. To tackle this challenge, we present a hybrid approach below. Instead of treating cells with  $0 < \alpha < 1$  as mixture cells, we first categorize each computational cell as either liquid or vapor (even the interfacial cells) depending on the location of their cell centers relative to the interface as shown in figure 4.7. The geometric volume of fluid method for advection of liquid volume fraction ensures that the interfacial region is not diffused and a planar interface may be reconstructed from the  $\alpha$  field with a reasonable assumption that the interface curvature is larger than the grid size. Due to this planar nature of a sub-grid interface, the location of cell-center can be easily defined to reside

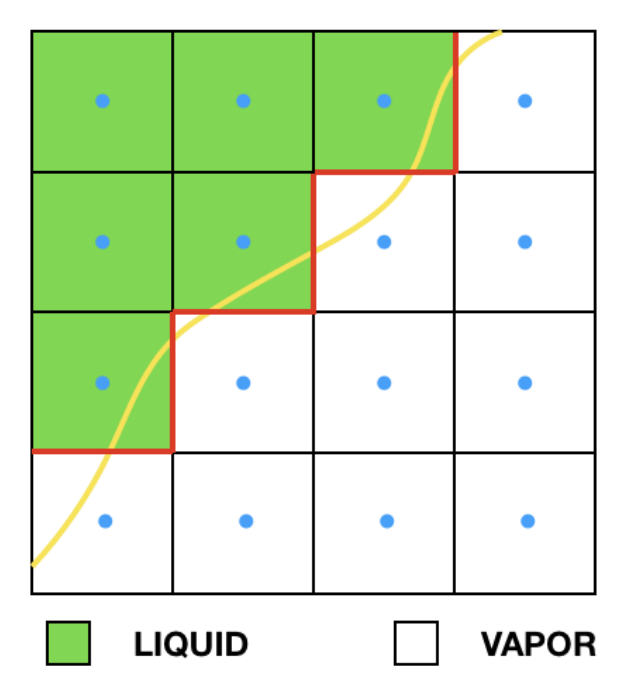


Figure 4.7: An instantiation of cells tagged as liquid or vapor to be treated as such in the solution of momentum equation. Cell faces shared by a liquid and vapor cell have been highlighted in red and are the interfacial faces, where the changes due to Ghost Fluid Method are directly implemented.

either in the liquid or vapor side based on the following expression,

$$\Xi_i^n = \begin{cases} \alpha_i^n \ge 0.5 & \text{Liquid Cells} \\ \alpha_i^n < 0.5 & \text{Vapor Cells} \end{cases} , \tag{4.31}$$

where  $\Xi$  identifies whether a computational cell is tagged as liquid or vapor. The definition is in-line with a prior GFM implementation in finite volume framework by Vukčević et al. [112], where they implemented the gravity force jump given in Eq. (4.1b).

Under this categorization, the momentum equation valid at each cell center is the single phase momentum equation instead of the whole domain formulation. Numerically, each cell assumes the density, and viscosity values that the cell-center is assigned based on Eq. (4.31). For incompressible flows and Newtonian fluids, the momentum equation for a single phase

can be written as,

$$\frac{\mathrm{d}}{\mathrm{d}t} \int_{\Omega_i} \mathbf{u} dV + \int_{\partial\Omega_i} \mathbf{u} \left( \mathbf{u} \cdot \mathbf{n} \right) dS = -\int_{\Omega_i} \frac{\nabla p_d}{\rho} dV + \int_{\partial\Omega_i} \nu \left( \nabla \mathbf{u} \cdot \mathbf{n} \right) dS. \tag{4.32}$$

In solving Eq. (4.32) for cells near the interface, the velocity flux, pressure gradient, and velocity gradient near the interface must be corrected to include the effect of jump conditions defined by Eq. (4.1a) and Eq. (4.1b). These corrections must be implemented at all the faces that lie between a liquid tagged cell and a vapor tagged cell, or mathematically represented by,

$$(\partial\Gamma)_{j}^{n} = \begin{cases} 1 & |\Xi_{P}^{n} - \Xi_{N}^{n}| > 0\\ 0 & |\Xi_{P}^{n} - \Xi_{N}^{n}| = 0 \end{cases}$$
 (4.33)

Here  $\partial\Gamma$  is used to refer the computational cell faces that are shared by a liquid and vapor cell (also referred as interfacial faces in the remaining text). A simple graphical representation of the proposed concept is shown in figure 4.8. On performing any surface integral that includes  $\partial\Gamma$  in figure 4.8, care has to be taken for using a liquid value for liquid cell, and vapor value for vapor cell. Hence, all interfacial faces must be populated with both liquid and vapor values of a variable, like volume flux  $(\phi_f)$ , or face normal pressure gradient  $(\nabla^{\perp}_f p_d)$ .

As the focus of this work is to capture the velocity discontinuity due to phase change at the interface, we relax the sharp treatment of some of the terms in Eq. (4.32) and jump conditions, Eq. (4.1a) and Eq. (4.1b), which converts the formulation into a hybrid approach. These relaxations are:

• Surface Tension Jump (treated smoothly): The jump in pressure due to surface ten-

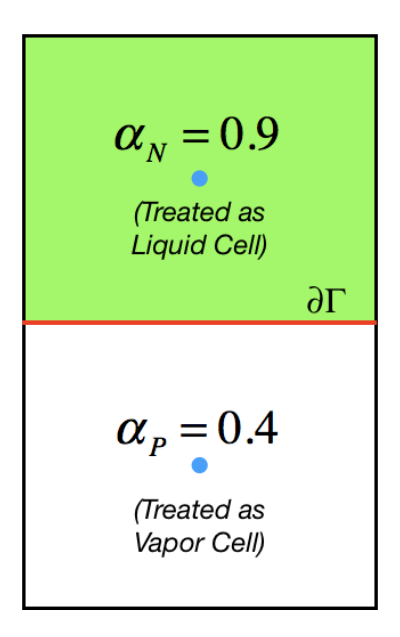


Figure 4.8: An example pair of cells showing them tagged as liquid and vapor, and highlighting the interfacial face between them.

sion given by  $\sigma\kappa$  is not treated sharply in this treatment. We continue to handle this interfacial discontinuity using the existing CSF formulation [133], where the capillary force pressure jump is smoothed close to the interface. The related expression given by Eq. (4.13) is added to Eq. (4.32) to reflect this jump in pressure.

- Viscous forces ( $\mu = 0$ ): Viscosity is assumed to be zero due to its relative unimportance for the intended bubble dynamics applications.
- Gravitational forces ( $\mathbf{g} = 0$ ): Dynamic pressure ( $p_d$ ) used in OpenFOAM calculations as a proxy for pressure has a jump in its value associated with gravitational forces as shown in Eq. (4.1b). For the present work, it is assumed to be zero.

The extension of surface tension pressure jump using Ghost Fluid method would require a more robust method of curvature calculation, which adds another dimension of complexity to the method. However, updates to the viscous and gravitational force calculations are straightforward. GFM Implementation of the gravitational jump for  $p_d$  in OpenFOAM has already been published by Vukčević et al. [112] and will be included in the solver at a later stage of development.

With above simplifications, the final momentum equation that must be solved in each computational cell is given by,

$$\frac{\mathrm{d}}{\mathrm{d}t} \int_{\Omega_i} \mathbf{u} dV + \int_{\partial \Omega_i} \mathbf{u} \left( \mathbf{u} \cdot \mathbf{n} \right) dS = -\int_{\Omega_i} \frac{\nabla p_d}{\rho} dV + \int_{\Omega_i} \sigma \kappa \nabla \alpha dV. \tag{4.34}$$

Along with this equation, the interfacial conditions that must be satisfied by velocity used in the momentum flux represented by the advection term is given by,

$$\mathbf{u}_{L,\Gamma} \cdot \mathbf{n}_{\Gamma} = \dot{\mathbf{x}}_{\Gamma} \cdot \mathbf{n}_{\Gamma} + \frac{\dot{m}''}{\rho_L}, \quad \text{and}$$
 (4.35a)

$$\mathbf{u}_{V,\Gamma} \cdot \mathbf{n}_{\Gamma} = \dot{\mathbf{x}}_{\Gamma} \cdot \mathbf{n}_{\Gamma} + \frac{\dot{m}''}{\rho_{V}}.$$
(4.35b)

Finally, the evaluation of pressure term must follow the following jump conditions,

$$p_{V,\Gamma} - p_{L,\Gamma} = \Delta p_{\Gamma} = -\dot{m}''^{2} \left( \frac{1}{\rho_{V}} + \frac{1}{\rho_{L}} \right), \quad \text{and} \quad (4.36a)$$

$$\left( \left( \frac{\nabla p}{\rho} \right)_{V,\Gamma} - \left( \frac{\nabla p}{\rho} \right)_{L,\Gamma} \right) \cdot \mathbf{n}_{\Gamma} = -\left( \frac{1}{\rho_V} - \frac{1}{\rho_L} \right) \frac{\mathrm{d}\dot{m}''}{\mathrm{d}t}.$$
(4.36b)

These jump conditions are imposed by using the Ghost fluid approach to evaluate the advection and pressure terms for liquid and vapor cells near an interface.

An important concept is introduced in Eq. (4.36b). In most previous formulations of

GFM, the R.H.S. of this equation is assumed to be zero as described in §(4.1). However, a detailed derivation to evaluate the jump in pressure gradient at the interface has been done as part of this work starting from the general conservation expression given by Eq. (B.5). For a good organization of the details related to this derivation, it has been presented in §(B.3) along with a suitable test case verifying the validity of the expression given in Eq. (4.36b).

#### Intermediate Velocity

Following the established projection method of Chorin [124] to solve the momentum equation, an intermediate velocity needs to be computed without contribution from the pressure term. In the finite volume framework, this is accomplished in two steps. At first, we only consider the temporal and advection terms from Eq. (4.34), which in its discretized form is given by,

$$\frac{\mathbf{u}_P^* - \mathbf{u}_P^n}{\Delta t} |\Omega_P| + \sum_{f \in \partial \Omega_P} \phi_f^n \mathbf{u}_f^{r'} = 0.$$
 (4.37)

Here, P refers to the computational cell for which the projection velocity  $(\mathbf{u}_P^*)$  is evaluated and  $\mathbf{u}_f^{r'}$  refers to an implicit calculation of face value that is described below.

To simplify the following discussion on implementation of the jump conditions, we consider the case of a liquid cell. Expanding Eq. (4.37) for a liquid cell, and writing the advection term as a sum of pure liquid faces and interfacial faces, it gives,

$$\frac{\mathbf{u}_{P}^{*} - (\mathbf{u}_{P})_{L}^{n}}{\Delta t} |\Omega_{P}| + \sum_{f \in \partial \Omega_{P}/\partial \Gamma} \phi_{Lf}^{n} \mathbf{u}_{f}^{r'} + \sum_{f \in \partial \Omega_{P} \cap \partial \Gamma} \phi_{Lf}^{n} \mathbf{u}_{Lf}^{r'} = 0.$$
(4.38)

Here,  $\partial \Omega_P \cap \partial \Gamma$  refers to the interfacial cell faces as defined in Eq. (4.33), and  $\partial \Omega_P / \partial \Gamma$  refers

to all other cell faces that circumscribe a computational cell. This distinction is graphically represented in figure 4.9. Also note that in the temporal term, the quantity that denotes the  $n^{th}$  time step has been specialized to have a liquid value. If a computational cell has changed from vapor to liquid due to interface motion over the current time step, the corresponding value from the previous time step must be updated.

The face velocity used to compute volume flux  $\phi_{L,f}$  (or  $\phi_{V,f}$  in case of vapor cell) are obtained by interpolation from the velocities stored at cell centers. Figure 4.9 depicts the values stored for a typical GFM computational cell grid. The interpolated velocity for  $f \in$ 

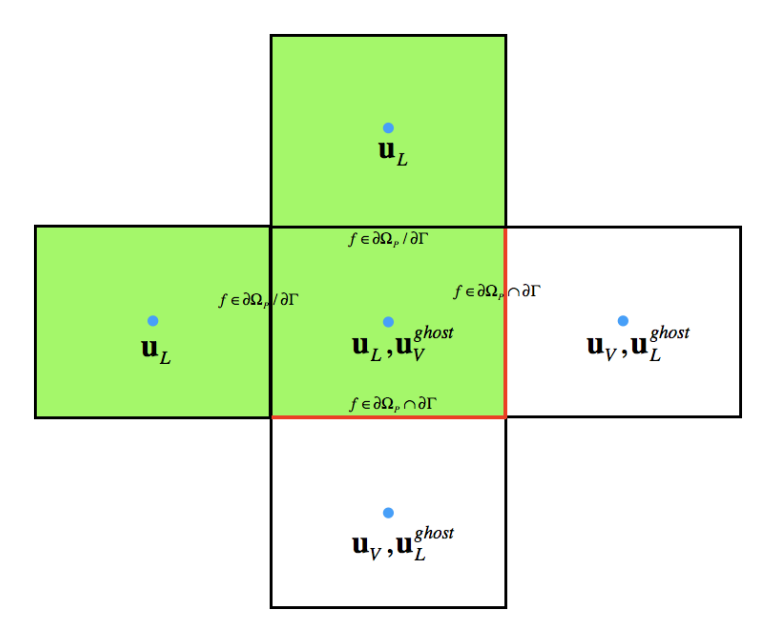


Figure 4.9: An example computational cell grid, where the green cells represent liquid cells and white cells represent vapor cells. The red highlighted cell boundaries are the interfacial faces. Cells sharing an interfacial face are populated with two velocity values, one corresponding to its original phase and another ghost value.

 $\partial \Omega_P / \partial \Gamma$  is simply given by,

$$u_f^{r'} = \frac{1 + \theta(f)w}{2} \mathbf{u}_P^* + \frac{1 - \theta(f)w}{2} \mathbf{u}_N^n, \tag{4.39}$$

where  $\theta(f)$  refers to the sign convention used in OpenFOAM related to the owner-neighbor relation of a cell with the face, and w refers to the interpolation weight calculated depending on the interpolation scheme used [116]. For interfacial faces  $(f \in \partial \Gamma)$ , the ghost liquid value of the neighbor cell must be employed to evaluate the face velocity, which is given by,

$$u_{L,f}^{r'} = \frac{1 + \theta(f)w}{2} \mathbf{u}_{P}^{*} + \frac{1 - \theta(f)w}{2} (\mathbf{u}_{N}^{n})_{L}^{ghost}.$$

$$u_{L,f}^{r'} = \frac{1 + \theta(f)w}{2} \mathbf{u}_{P}^{*} + \frac{1 - \theta(f)w}{2} \left( \mathbf{u}_{N}^{n} - (\dot{m}'')_{N}^{n} \left( \frac{1}{\rho_{V}} - \frac{1}{\rho_{L}} \right) \mathbf{n}_{\Gamma}^{n} \right). \tag{4.40}$$

Substituting Eq. (4.39) and Eq. (4.40) in Eq. (4.38) we get,

$$\frac{\mathbf{u}_{P}^{*} - (\mathbf{u}_{P})_{L}^{n}}{\Delta t} |\Omega_{P}| + \sum_{f \in \partial \Omega_{P}/\partial \Gamma} \left( \frac{1 + \theta(f)w}{2} \mathbf{u}_{P}^{*} + \frac{1 - \theta(f)w}{2} \mathbf{u}_{N}^{n} \right) \phi_{Lf}^{n} + \sum_{f \in \partial \Omega_{P} \cap \partial \Gamma} \left( \frac{1 + \theta(f)w}{2} \mathbf{u}_{P}^{*} + \frac{1 - \theta(f)w}{2} \left( \mathbf{u}_{N}^{n} - (\dot{m}'')_{N}^{n} \left( \frac{1}{\rho_{V}} - \frac{1}{\rho_{L}} \right) \mathbf{n}_{\Gamma}^{n} \right) \right) \phi_{Lf}^{n} = 0.$$
(4.41)

On rearranging all the terms, Eq. (4.41) can be written as,

$$\left(\frac{|\Omega_{P}|}{\Delta t} + \sum_{f \in \partial \Omega_{P}} \left(\frac{1 + \theta(f)w}{2}\right) \phi_{Lf}^{n}\right) \mathbf{u}_{P}^{*} = (\mathbf{u}_{P})_{L}^{n} \frac{|\Omega_{P}|}{\Delta t} - \sum_{f \in \partial \Omega_{P}} \left(\frac{1 - \theta(f)w}{2}\right) \mathbf{u}_{N}^{n} \phi_{Lf}^{n} + \sum_{f \in \partial \Omega_{P} \cap \partial \Gamma} \left(\frac{1 - \theta(f)w}{2}\right) (\dot{m}'')_{N}^{n} \left(\frac{1}{\rho_{V}} - \frac{1}{\rho_{L}}\right) \mathbf{n}_{\Gamma}^{n} \phi_{Lf}^{n}.$$

$$(4.42)$$

Succinctly, the coefficient of  $\mathbf{u}_P^*$  on the left hand side of the above equation is termed as  $A_P$  and the right hand side is termed  $H(\mathbf{u}^n)$ . Equation (4.42) represents the equation for a liquid cell. Compared to the solver without phase change, we have one additional component given by the last term that will be zero in the absence of phase change leading to a continuous

velocity field.

The expression defined in Eq. (4.42) was specialized for a liquid cell. For a vapor cell, it will have a similar form except that the velocity correction term for interfacial faces changes its sign, and the first step for a vapor cell looks like,

$$\left(\frac{|\Omega_{P}|}{\Delta t} + \sum_{f \in \partial \Omega_{P}} \left(\frac{1 + \theta(f)w}{2}\right) \phi_{Vf}^{n}\right) \mathbf{u}_{P}^{*} = (\mathbf{u}_{P})_{V}^{n} \frac{|\Omega_{P}|}{\Delta t} - \sum_{f \in \partial \Omega_{P}} \left(\frac{1 - \theta(f)w}{2}\right) \mathbf{u}_{N}^{n} \phi_{Vf}^{n} - \sum_{f \in \partial \Omega_{P} \cap \partial \Gamma} \left(\frac{1 - \theta(f)w}{2}\right) (\dot{m}'')_{N}^{n} \left(\frac{1}{\rho_{V}} - \frac{1}{\rho_{L}}\right) \mathbf{n}_{\Gamma}^{n} \phi_{Vf}^{n}.$$

$$(4.43)$$

For a liquid cell near the interface, the intermediate velocity corresponding to the liquid phase will be evaluated by Eq. (4.42). But in a finite volume framework, these values are interpolated at the faces before they are used in the Poisson equation. Hence,  $\mathbf{u}_P^*$  value in the adjacent vapor cell must be corrected to obtain a consistent liquid value at the faces. The same should be implemented for vapor cells. As a result, on the interpolation of these cell-centered projection velocities calculated from Eq. (4.42) and Eq. (4.43), each interfacial face will have two separate face values, each corresponding to a liquid and vapor phase.

The associated volume flux from these expressions of intermediate velocity can be mathematically written as,

$$\phi_f^* = \begin{cases} \left(\frac{H(\mathbf{u}^n)}{A_P}\right)_f \cdot \mathbf{S}_f & f \notin \partial \Gamma \\ \left(\frac{H(\mathbf{u}^n)}{A_P}\right)_f \cdot \mathbf{S}_f - \left(\frac{1-\theta(f)w}{2}\right) (\dot{m}'')_N^n \left(\frac{1}{\rho_V} - \frac{1}{\rho_L}\right) \mathbf{n}_{\Gamma}^n \cdot \mathbf{S}_f & f \in \partial \Gamma \text{ and solving for liquid cell } \cdot \\ \left(\frac{H(\mathbf{u}^n)}{A_P}\right)_f \cdot \mathbf{S}_f + \left(\frac{1-\theta(f)w}{2}\right) (\dot{m}'')_N^n \left(\frac{1}{\rho_V} - \frac{1}{\rho_L}\right) \mathbf{n}_{\Gamma}^n \cdot \mathbf{S}_f & f \in \partial \Gamma \text{ and solving for vapor cell} \end{cases}$$

$$(4.44)$$

Surface tension term from Eq. (4.34) is added to Eq. (4.44) to obtain the final projection velocity flux. The final expression is given by,

$$\phi_f^r = \phi_f^* + \left(\frac{1}{A_P}\right)_f (\sigma \kappa)_f^{n+1} \left(\nabla_f^{\perp} \alpha\right)^{n+1} |\mathbf{S}_f|$$
(4.45)

#### **Poisson Equation**

The contribution of pressure is added to correct Eq. (4.45) and obtain the final velocity flux given by,

$$\phi_f^{m+1} = \phi_f^r - \left(\frac{1}{A_P}\right)_f \frac{1}{\rho} \left(\nabla_f^{\perp} p_d\right)^{m+1} |\mathbf{S}_f|. \tag{4.46}$$

If the face is shared by computational cells of the same phase, the  $\phi$  values are the same for equations written for either cell. However, if f is an interfacial face,  $\phi$  values used at the face for liquid cell are different from the case when the face values are used for the sharing vapor cell as described in Eq. (4.44).

Taking a divergence based on these fluxes over all the faces of a computational cell gives,

$$\sum_{f \in \partial \Omega_P} \theta(f) \phi_f^{m+1} = \sum_{f \in \partial \Omega_P} \theta(f) \phi_f^r - \sum_{f \in \partial \Omega_P} \left(\frac{1}{A_P}\right)_f \frac{\theta(f)}{\rho} \left(\nabla_f^{\perp} p_d\right)^{m+1} |\mathbf{S}_f|,$$

which due to continuity of each cell (treated either as liquid or vapor) reduces to,

$$\sum_{f \in \partial \Omega_P} \theta(f) \left( \frac{1}{A_P} \right)_f \left( \frac{1}{\rho} \right) \left( \nabla_f^{\perp} p_d \right)^{m+1} |\mathbf{S}_f| = \sum_{f \in \partial \Omega_P} \theta(f) \phi_f^r. \tag{4.47}$$

While the R.H.S. in Eq. (4.47) is evaluated using Eq. (4.45), left hand side must be

corrected to evaluate the pressure gradient for either liquid or vapor phase at the interfacial cells. The corrections can be derived by substituting the pressure jump conditions, Eq. (4.36a) and Eq. (4.36b) in the corrections proposed using Ghost Fluid Method in  $\S(C.4)$ . At the interfacial cells, if face f is owned by a liquid cell,

$$\left(\frac{1}{A_P}\right)_f \left(\frac{1}{\rho_L}\right) \left(\nabla_f^{\perp} p_d\right)_L = \left(\frac{1}{A_P}\right)_f \frac{1}{\rho^*} \left(\frac{(p_d - \Delta p_{\Gamma})_N - (p_d)_P}{\Delta x} + \frac{\rho_L - \rho_V}{\rho_L} \frac{d\dot{m}''}{dt} (1 - \lambda_f)\right) |\mathbf{S}_f|, \quad \text{and}$$

$$\left(\frac{1}{A_P}\right)_f \left(\frac{1}{\rho_L}\right) \left(\nabla_f^{\perp} p_d\right)_V = \left(\frac{1}{A_P}\right)_f \frac{1}{\rho^*} \left(\frac{(p_d)_N - (p_d + \Delta p_{\Gamma})_P}{\Delta x} - \frac{\rho_L - \rho_V}{\rho_V} \frac{d\dot{m}''}{dt} \lambda_f\right) |\mathbf{S}_f|, \quad (4.48b)$$

where  $\lambda_f$  is a non-dimensional quantity representing an approximate distance of the interface from the cell centers given by Eq. (C.2). Similarly, if face f is owned by a vapor cell,

$$\left(\frac{1}{A_P}\right)_f \left(\frac{1}{\rho_L}\right) \left(\nabla_f^{\perp} p_d\right)_L = \left(\frac{1}{A_P}\right)_f \frac{1}{\rho^{**}} \left(\frac{(p_d)_N - (p_d - \Delta p_\Gamma)_P}{\Delta x} + \frac{\rho_L - \rho_V}{\rho_L} \frac{d\dot{m}''}{dt} \lambda_f\right) |\mathbf{S}_f|, \quad \text{and}$$

$$\left(\frac{1}{A_P}\right)_f \left(\frac{1}{\rho_L}\right) \left(\nabla_f^{\perp} p_d\right)_V = \left(\frac{1}{A_P}\right)_f \frac{1}{\rho^{**}} \left(\frac{(p_d + \Delta p_\Gamma)_N - (p_d)_P}{\Delta x} - \frac{\rho_L - \rho_V}{\rho_V} \frac{d\dot{m}''}{dt} (1 - \lambda_f)\right) |\mathbf{S}_f|. \tag{4.49b}$$

Using the updated gradient calculations in Eq. (4.47) results in a symmetric linear system of equations, which is solved using the preconditioned conjugate gradient (PCG) method. Note that Eq. (4.48) and Eq. (4.49) are used for the interfacial faces. The evaluated value for  $p_d$  is then used to calculate the pressure gradient flux at the cell faces needed to update the value of volume flux defined in Eq. (4.46). The corrected flux is reconstructed to get cell-centered velocity values as described in [116] and repeated here for completeness,

$$\mathbf{u}_{P}^{m+1} = \mathbf{u}_{P}^{*} + \left(\frac{1}{A_{P}}\right) \left(\sum_{f \in \partial \Omega_{P}} \frac{\mathbf{S}_{f} \otimes \mathbf{S}_{f}}{|\mathbf{S}_{f}|}\right)^{-1} \cdot \left(\sum_{f \in \partial \Omega_{P}} \left(\frac{\phi_{f}^{m+1} - \mathbf{u}_{f}^{*} \cdot \mathbf{S}_{f}}{\left(\frac{1}{A_{P}}\right)_{f}}\right) \frac{\mathbf{S}_{f}}{|\mathbf{S}_{f}|}\right). \tag{4.50}$$

At the interfacial faces, both  $\phi_f$  and  $\mathbf{u}_f^*$  will have two values corresponding to the liquid and vapor phase. These values are carefully used in the reconstruction of liquid or vapor cell-centered value near the interface, respectively.

#### 4.4 Solver Development: ghostFluidPhaseChangeFoam

A graphical work flow of the developed OpenFOAM code is presented below in figure 4.10.

#### 4.4.1 Phase Change Tests

Two tests are presented in this section. The first test pertains to the  $\alpha$  advection equation and assesses that the interface advection due to a source term is done correctly as defined in  $\S(4.3.1)$ . The second test is for the solution of pressure and velocity along with an advecting interface. It is a one-dimensional test called the Stefan-Flow problem, which assesses the implementation of the pressure-velocity coupling using the Ghost Fluid Method in the PISO iteration as defined in  $\S(4.3.2)$ .

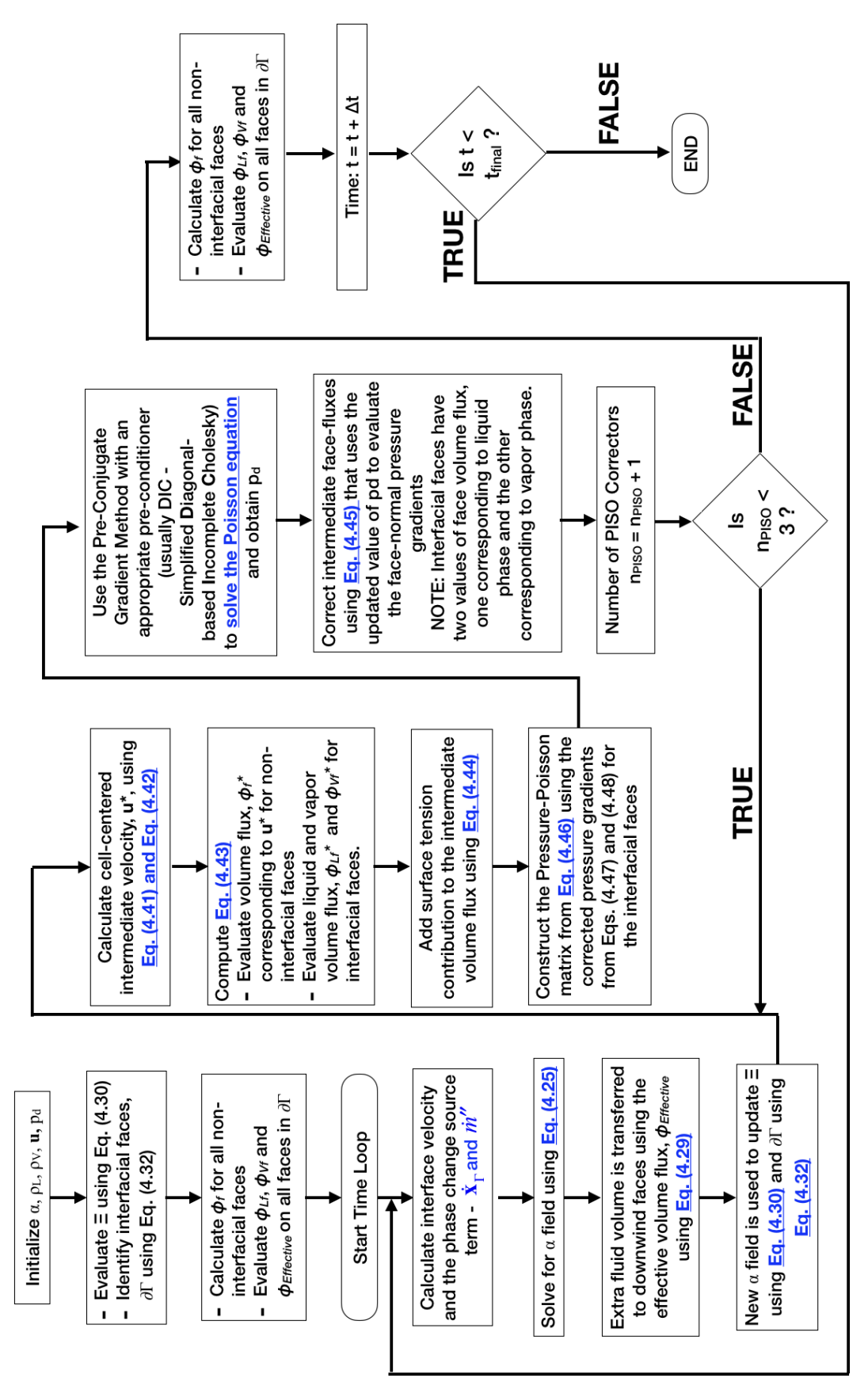


Figure 4.10: Algorithm for solution of interface advection and momentum equation for two-phase flow with phase change presented in this thesis.

#### Pure advection due to mass flux source at the interface

To test the correct implementation of  $\alpha$  advection under the effect of a source term, a simple test case is used. A two-dimensional domain of size ( $[0, 8 \times 10^{-3}]$ ,  $[0, 8 \times 10^{-3}]$ ) is initialized with a circular zone at the geometric center of the domain with radius  $R_o = 10^{-3}$ . This region is initialized with  $\alpha = 0$  and the rest of the domain with  $\alpha = 1$  as shown in figure 4.11 (a). The pressure and velocity solution is turned off. Both bulk fluids are assumed to remain stationary and simply a constant interface velocity is prescribed,  $\dot{\mathbf{x}}_{\Gamma} \cdot \mathbf{n}_{\Gamma} = -2 \times 10^{-3}$  that is used to move the interface. The negative sign is because of the interface normal pointing inwards ( $\mathbf{n}_{\Gamma} = -\hat{\mathbf{r}}$ , where  $\hat{\mathbf{r}}$  refers to the radial direction corresponding to the initialized circle). Bulk velocity inside the disk remains equal to zero, while a radial velocity is analytically prescribed outside the disk. In addition to advection in the  $\alpha = 1$  region due to the bulk flow, values of  $\alpha$  change due to the source term associated with the phase change process, and the information is transferred to other cells using the effective flux defined in §(4.3.1).

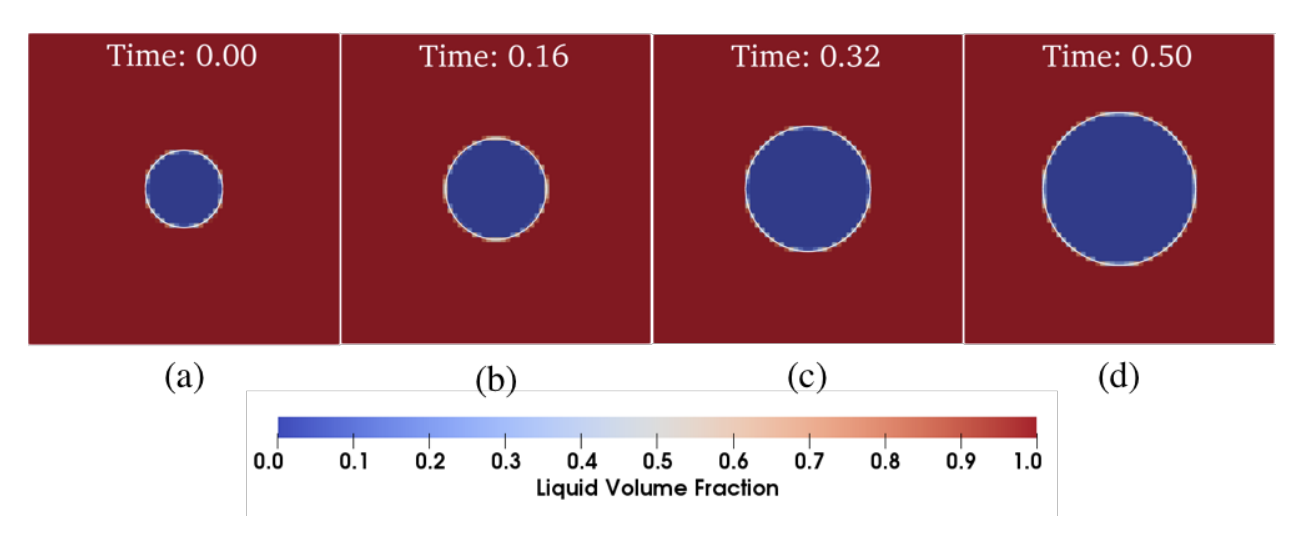


Figure 4.11: Alpha field with  $\alpha = 0.5$  contour (in white) for a circle growing purely due to a prescribed mass flux at the interface. Results shown for grid size  $64 \times 64$ .

Analytically, the circle should expand with the interface speed determining the rate of

change in the circle radius, i.e., the circle radius should increase linearly. This is correctly obtained in the results shown in figure 4.12. Here,  $N_x$  refers to the grid size in one direction,

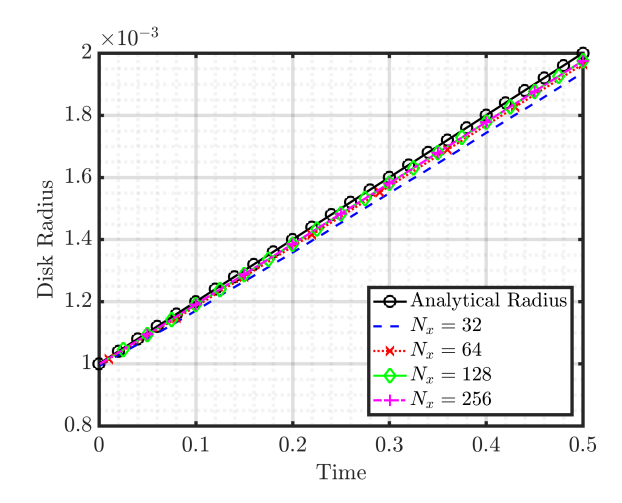


Figure 4.12: Circle radius growing purely due to a prescribed mass flux at the interface.

and the disk radius obtained from simulations is simply evaluated as,

$$R_{simulation} = \left(\sum_{i \in \text{All cells}} (1 - \alpha_i) \Omega_i\right)^{1/3}, \tag{4.51}$$

where  $\Omega_i$  is the  $i^{th}$  computational cell volume. Figure 4.12 clearly shows a converging trend of the bubble radius results and it affirms that the implementation of  $\alpha$  advection under the influence of interfacial source has been done correctly.

#### 1-D Stefan Flow

In this section, we present a 1-D test for phase change, which is commonly referred to as the Stefan Flow test [54, 60]. A graphical representation for this flow is shown in figure 4.13.

In this simple configuration, the vapor domain is near the wall and the liquid domain is closer to an outlet. Due to vaporization at the interface  $(\mathbf{x}_{\Gamma}(t))$ , the extent of the vapor

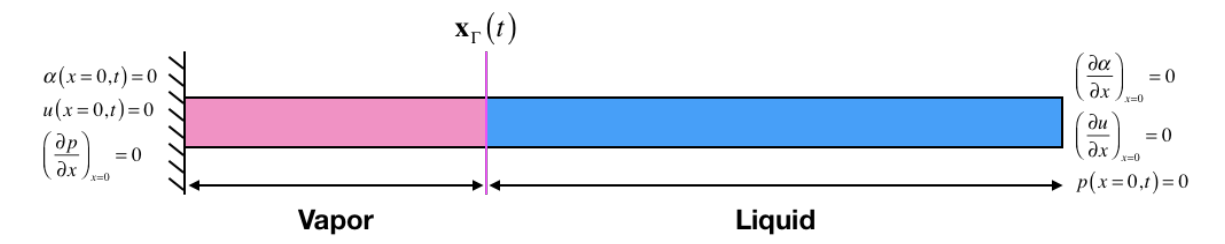


Figure 4.13: Representation of the liquid-vapor system in Stefan Flow.

domain increases. The vapor side remains stationary, while velocity jump results in an outward flow in the liquid phase (in this case a flow towards the right side of the domain). Physically, the vaporization occurs due to the temperature difference between the liquid and vapor phases. However, the current formulation has not been extended to solving the energy equation. Therefore, we simply include an analytical expression in the formulation that calculates the mass flux due to phase change  $(\dot{m}''(t))$  at the interface resulting in the ensuing flow. This mass flux is given by [134],

$$\dot{m}''(t) = \frac{k_V}{h_{LV}} \frac{\Delta T}{\sqrt{\pi \alpha_V t}} \operatorname{erf}(\varsigma) e^{-\varsigma^2}, \tag{4.52}$$

where  $h_{LV}$  refers to the latent heat of vaporization,  $k_V$  is the thermal conductivity of vapor phase,  $\Delta T = T_{wall} - T_{sat}$  is the temperature difference which causes the vaporization,  $\alpha_V$  is vapor thermal diffusivity, and  $\varsigma$  is obtained from the solution of a transcendental equation given by [134],

$$\varsigma \exp\left(\varsigma^2\right) \operatorname{erf}(\varsigma) = \frac{C_{pV}\Delta T}{\sqrt{\pi} h_{LV}}.$$
(4.53)

Here,  $C_{pV}$  refers to the specific heat of vapor at constant pressure. All the parameters defined for this case are tabulated in table 4.3.

Fluid	ρ	k	$C_p$	$\mu$	$\sigma$	$h_{LV}$
	$kg/m^3$	W/m-K	J/kg-K	Pa-s	N/m	J/kg
Vapor	0.597	0.025	2030	$1.26 \times 10^{-5}$	0.059	$2.26 \times 10^{6}$
Liquid	958.4	0.679	2030	$2.80 \times 10^{-4}$	-	-

Table 4.3: Thermophysical properties for Stefan Flow.

With  $T_{wall} = 383$  K and  $T_{sat} = 373$  K, the function for  $\dot{m}''(t)$ , which is directly implemented in the solution is given by,

$$\dot{m}''(t) = \frac{1.8144 \times 10^{-4}}{\sqrt{t}}. (4.54)$$

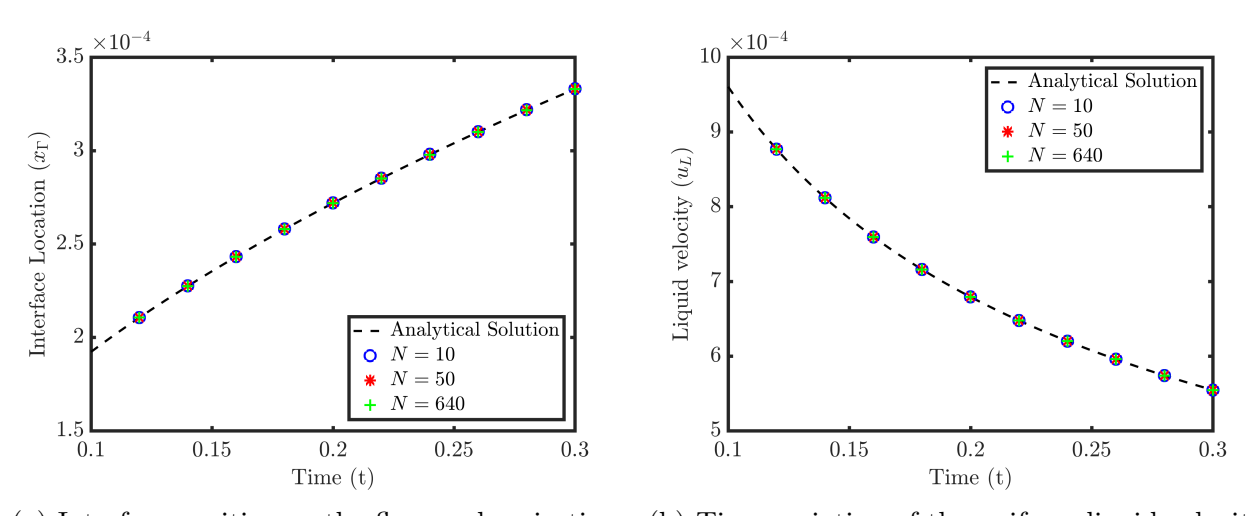
Also, the analytical expression for the location of interface, and liquid velocity as a function of time are given by,

$$x_{\Gamma}(t) = 6.0785 \times 10^{-4} \sqrt{t}, \quad \text{and}$$
 (4.55)

$$u_L(x \ge x_{\Gamma}, t) = \frac{3.0373 \times 10^{-4}}{\sqrt{t}}.$$
(4.56)

The system is initialized with values at t = 0.1. Interface position and liquid velocity values obtained in the simulation are compared with the analytical expressions defined in Eq. (4.55) and Eq. (4.56) for  $t \in [0.1, 0.3]$ .

The time series of interface location and liquid velocity in figure 4.15 shows that the advection of liquid volume fraction that implicitly captures the interface location, and the solution of the momentum equation using the Ghost Fluid method has been implemented accurately. The author would like to remind the reader that the energy equation and evaluation of mass flux are not incorporated in this solution and that Eq. (4.54) was used to

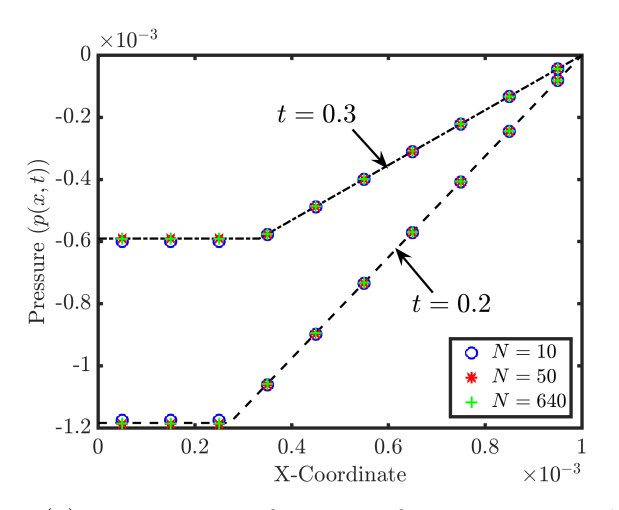


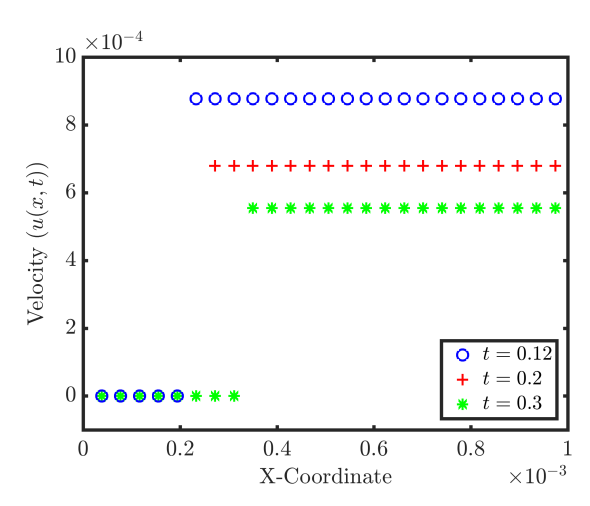
(a) Interface position as the flow evolves in time. (b) Time variation of the uniform liquid velocity,  $u_L(x,t) = u_L(t)$ .

Figure 4.14: Comparison of phase change solver solutions with analytical values for Stefan flow test case.

populate the mass flux values in the 1D domain.

An important distinction in the method proposed in §(4.3), compared to published phase change work, is the implementation of pressure gradient jump at the interface that occurs due to phase change. The pressure profile at two distinct times is presented in figure 4.15a. The analytical pressure profile matches quite well with the results from the pressure Poisson solution for the Stefan flow. The previous phase change methods [58, 60, 83, 89, 93, 97] that presented the results for Stefan flow have not provided the pressure profile obtained in the study. Furthermore, the method described here also captures the velocity discontinuity, sharply as shown in figure 4.15b. While the velocity profile is shown only for one case, the sharp profile remained consistent for all grid sizes tested in this work.





- (a) Pressure as a function of x at t = 0.2 and t = 0.3. Analytical pressure profile is shown with lines and the simulation values are shown with marker points in the plots.
- (b) Velocity profile of Stefan Flow at three distinct time points. Result is shown for N=640 case.

Figure 4.15: Spatial pressure and velocity variation capturing sharp changes at the interface.

### Chapter 5

## Summary & Future Work

The primary goal of this thesis was to provide a robust, theoretical model for simulation of single vapor bubbles, motivated by the growing use of controlled vapor bubble dynamics in improved heat transfer processes [14], medical technologies [18, 41], and reduced erosion damage [135]. Two different approaches for the bubble analysis were used. The first approach used a spherically-symmetric physical system that considerably simplifies the governing system of equations and the other approach aims to solve the complete three dimensional Navier - Stokes equations for a two-phase flow undergoing phase change through a highly resolved simulation (HRS) with only one main assumption that the bulk phases are incompressible. While the former approach is useful for a fundamental analysis of the bubble growth and collapse mechanisms [3, 10], the latter becomes necessary to capture the naturally occurring asymmetries in the system like presence of walls [11, 136], gravitational forces [23, 137], bulk liquid flow [92], or presence of multiple bubbles [138], which would almost inevitably be the case in any application.

Our approach and the findings from the 3-part analysis on vapor bubbles, liquid-vapor

phase change processes, and numerical simulations have been summarized below:

- First, we presented the development of a numerical model called Compressible Vapor Saturated Interface solution or CVSI solution for a spherically symmetric system of a collapsing bubble. This model was implemented and solved in MATLAB for different cases of single vapor bubble collapse in an initially uniform liquid environment. The study extended over a wide range of thermo-physical conditions for bubble collapse, which has traditionally been categorized into thermal, intermediate, and inertial types. An analysis was done on the less studied category of bubble collapse that undergoes a moderately fast process, i.e., intermediate collapse. Such a collapse was shown to exhibit large pressure and temperature variations during the entire collapse period, a characteristic unique to this intermediate range of conditions. This was found to be related to the bulk motion of vapor inside the bubble, which is often ignored in spherical bubble analysis. Additionally, a generalized framework to categorize different system conditions of bubble collapse was also provided, where the distinctions between a very slow collapse, intermediate collapse, and fast collapse were redrawn [3]. A key takeaway from this distinction was the notable effect of the rate of change in far-field pressure conditions that initiate a collapse on the ensuing rate of collapse.
- The next step in this thesis was to review existing HRS methods that have been used in the literature to study vapor bubbles. It was identified that the assumptions of vapor incompressibility and constant interface temperature, taken almost universally by such methods have not been verified by these studies. Prior experience with the CVSI model developed for bubble collapse had shown that even for bubble growth, variations in

interface temperature, and vapor density can be expected. Hence, the aforementioned HRS assumptions were assessed as a separate study by using the canonical case of bubble growth [1]. Even for a single growing spherical bubble, this assumption was found to be limiting for an initial period of the bubble lifetime. During the initial stages of bubble growth, vapor pressure, temperature, and density were found to exhibit noticeable variation in time, which cannot be ignored. Therefore, an analytical expression was derived that can approximate the extent of this initial period of bubble growth. This approximation can be used as a threshold beyond which the contemporary HRS assumption of incompressibility can be used. Moreover, it highlighted the necessity to reassess the assumptions used in HRS methods on a case-by-case basis.

• Through the review of HRS methods, it was also recognized that an easy to implement, and scalable framework to study phase change problems like vapor bubble dynamics, was not present. It also helped identify that the primary challenge of phase change methods is to capture the discontinuity of velocity observed close to an interface. A useful method implemented to capture this discontinuity is called the Ghost Fluid Method (GFM). Interestingly, we highlighted that the existing implementations of GFM assume that phase change does not cause a jump in the pressure gradient at the interface, which is shown to be inaccurate even for a spherical growing bubble in this work. Hence, we have proposed a new Finite-Volume based phase change HRS method implemented in the scalable environment of OpenFOAM. The capture of interface advection under bulk flow with phase change was improved by proposing a concept of effective flux that can be used for interfacial faces to transport the extra fluid generated

due to phase change. Secondly, the GFM approach for the pressure-velocity coupling of a two-phase flow was modified to capture the pressure gradient jump. A detailed derivation to obtain an expression for this jump has also been presented. One-dimensional tests has been conducted as a proof of concept, which have given promising results for further development.

While fundamental improvements to the phase change numerical solver development have already been proposed and implemented, the completion of such a solver is a massive undertaking and several future steps have been listed below to advance this development:

- Energy Equation: The GFM idea proposed for pressure solution in §(4.3) can be directly applied to solve the advection-diffusion equation for temperature in both liquid and vapor phases near the interface.
- Evaluation of Mass Flux: Due to the dependence of mass flux calculation at the interface on temperature profile Eq. (4.1c), and the evaluation of ghost temperature values on the calculation of mass flux, an iterative method must be implemented. An initial solution for the advanced value of temperature  $(T^{n+1})$  can be obtained using the temperature gradient jump defined from the mass flux value of the previous time step  $(\dot{m}'')^n$ . Using the updated values of T, and setting the interface temperature as  $T_{sat}$ , the new value of  $\dot{m}''$  can be evaluated and the energy equation solution re-evaluated.
- Populating Ghost Values: The value for mass flux due to phase change, which is only physically present at the interface, has to be populated in cell centers of interfacial and adjacent cells. This is needed to calculate ghost velocity values in those cells. This requires a constant-normal wise extrapolation of liquid temperature gradient at the

interface  $((\nabla T_L)_{\Gamma})$  on the vapor side, and vapor temperature gradient at the interface  $((\nabla T_V)_{\Gamma})$  on the liquid side. These values can then directly be used with Eq. (4.1c) to populate mass flux values in the interfacial region  $(\Omega_{\Gamma})$ . Such an extension may be adopted from previous works [54, 60, 93], which have implemented a similar concept.

## Appendices

### Appendix A

### Numerical Convergence of CVSI

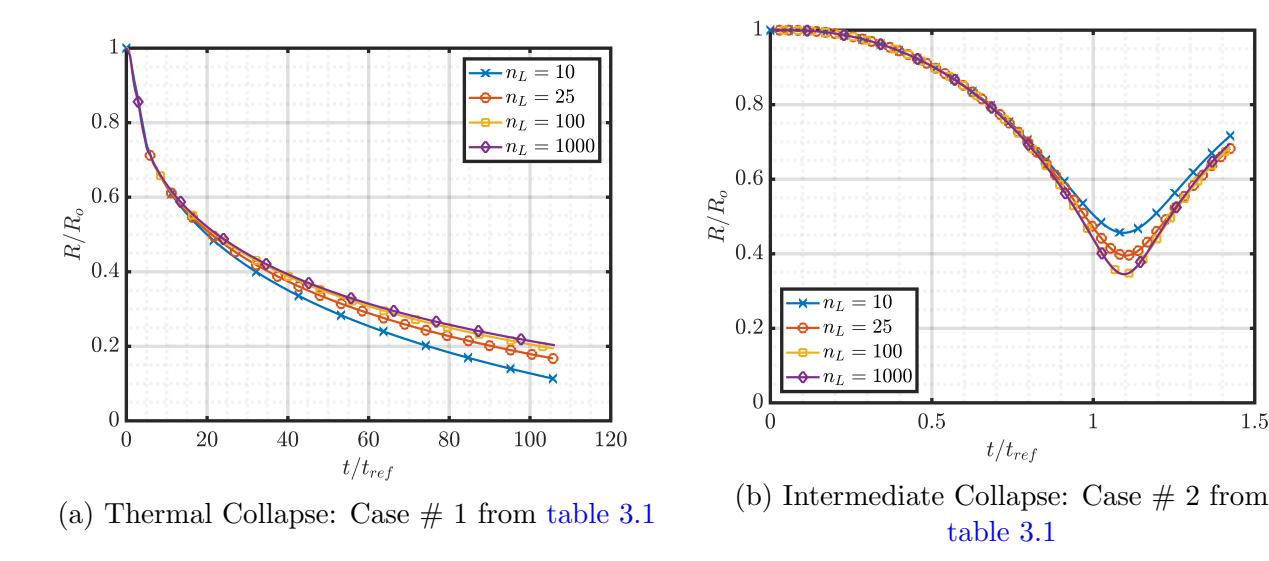
#### **Model Solutions**

The numerical convergence behavior of the predictions from the CVSI model was evaluated by considering the bubble radius versus time curves for a typical case of thermal, intermediate and inertial dominated collapse. The numerical parameters invoved are  $(\zeta, s_L, s_V, n_L, n_V)$ . The extent of the liquid domain is determined by  $\zeta$ , which is employed as a multiplier of the initial bubble radius,  $R_o$ . Grid compression near the interface is employed to reduce the overall computational burden and is controlled by the parameters  $s_L$  in the liquid domain (Eq. (2.31)) and  $s_V$  in the vapor domain (Eq. (2.33)). The total number of liquid and vapor computational cells is denoted by  $n_L$  and  $n_V$ , respectively. In all of the computations presented in the paper, we employ a value of  $s_L = 5$  and  $s_V = 5$  to ensure an adequate level of grid compression, and employ a corresponding value of  $n_L$  and  $n_V$  to ensure numerical convergence as detailed below.

The first numerical test corresponds to the calculation of liquid temperature and the

1.5

results are presented in figure A.1. In these calculations the following numerical parameters are held fixed at  $\zeta = 2$ ,  $s_L = 5$ ,  $s_V = 5$ , and  $n_V = 2000$ , and  $n_L$  is systematically varied from 10 to 1000. The results show that beyond a value of  $n_L = 100$ , the predictions have essentially converged.



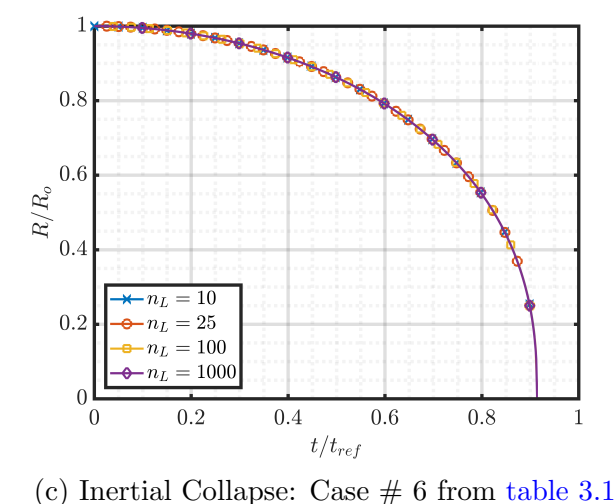


Figure A.1: Bubble radius versus time plot for different levels of grid refinement for liquid temperature equation, Eq. (2.24), with  $\zeta = 2$ ,  $s_L = 5$ ,  $s_V = 5$ , and  $n_V = 2000$ .

A similar analysis is conducted for the vapor side with parameters  $\zeta = 2$ ,  $s_L = 5$ ,  $s_V = 5$ , and  $n_L = 1000$ , and by varying the value of  $n_V$  from 10 to 1000. The results show that time variation of bubble radius is practically independent of  $n_V$ . This is expected because in figure 2.3a, we show that vapor side heat transfer is almost negligible when compared to liquid side heat transfer, and that it does not affect the rate of condensation during collapse.

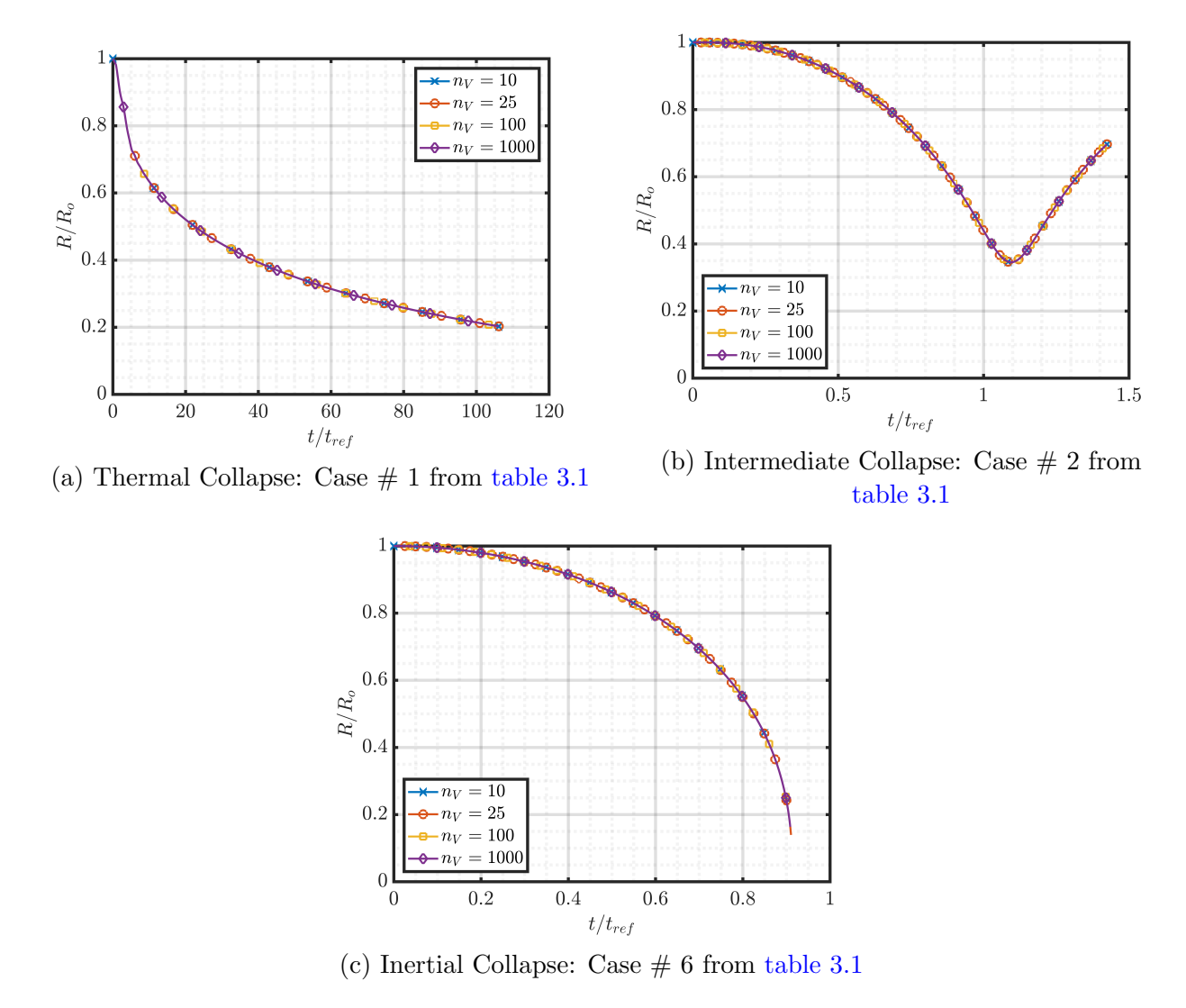
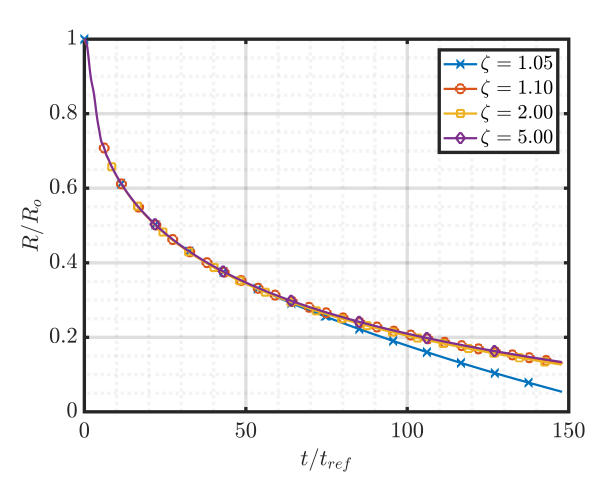
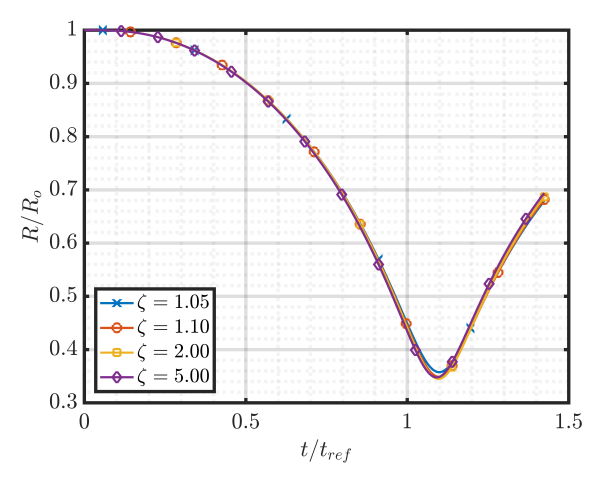


Figure A.2: Bubble radius versus time plot for different levels of grid refinement for vapor temperature equation, Eq. (2.18), with  $\zeta = 2$ ,  $s_L = 5$ ,  $s_V = 5$ , and  $n_L = 1000$ .

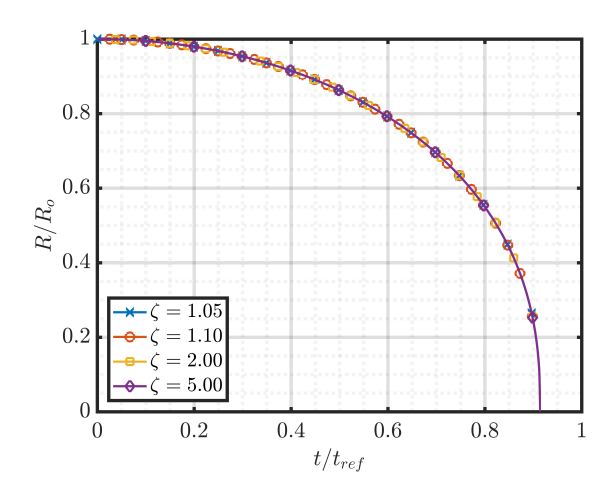
Lastly, the effect of the extent of liquid domain is evaluated by changing the value of  $\zeta = \{1.05, 1.1, 2, 5\}$ . This test is important as the solution of liquid temperature equation governs

the rate of condensation and the results should be independent of the far-field boundary condition, where  $T_L(r_{\infty},t)=T_{\infty}$ . Number of liquid shells,  $n_L$  was varied such that the average size of the shells can remain constant for different liquid domain sizes and hence,  $n_L=(\zeta-1)\times 100$ . The remaining parameters are held fixed at  $s_L=5$ ,  $s_V=5$ , and  $n_V=100$ . Except for a very small liquid domain represented by  $\zeta=1.05$ , the results are independent of the value of  $\zeta$ . There is practically no difference in the results of bubble radius for all three categories due to change in the physical domain that is solved for the liquid temperature equation.





- (a) Thermal Collapse: Case # 1 from table 3.1
- (b) Intermediate Collapse: Case # 2 from table 3.1



(c) Inertial Collapse: Case # 6 from table 3.1

Figure A.3: Bubble radius versus time plot for different extent of the liquid domain for Eq. (2.24), with  $s_L = 5$ ,  $s_V = 5$ ,  $n_L = 100$ , and  $n_V = 100$ .

## Appendix B

#### Relevant Derivations for Phase

## Change

Several expressions used in the derivations presented in  $\S(4.3)$  were referred to this section for a complete derivation.

# B.1 Relation between Material Volume and Control Volume with a surface of discontinuity

Let a generic material volume containing a surface of discontinuity be given by figure B.1.

If figure B.1 is treated as a material volume then it's salient features are:

•  $\partial\Omega_L$  and  $\partial\Omega_V$  are material surfaces, which means that they move with the same speed as the local fluid velocity

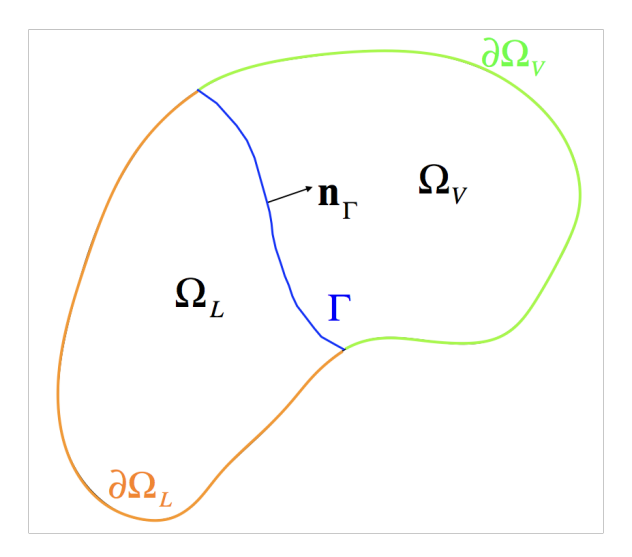


Figure B.1: Generic two-phase volume with interface

•  $\Gamma$  is a surface of discontinuity within the volume  $\Omega = \Omega_L \cup \Omega_V$ . This implies that  $\Omega_L$  and  $\Omega_V$  are not material volumes.

Using the fundamental transport equation [139], we can write the conservation equation for a variable  $\psi$  as,

$$\frac{\mathrm{d}}{\mathrm{d}t} \int_{\Omega_L} \psi dV = \int_{\Omega_L} \frac{\partial \psi}{\partial t} dV + \int_{\partial \Omega_L} \psi \left( \mathbf{u} \cdot \mathbf{n} \right) dS + \int_{\Gamma} \psi_L \left( \dot{x}_{\Gamma} \cdot \mathbf{n}_{\Gamma} \right) dS, \quad \text{and} \quad (B.1a)$$

$$\frac{\mathrm{d}}{\mathrm{d}t} \int_{\Omega_V} \psi dV = \int_{\Omega_V} \frac{\partial \psi}{\partial t} dV + \int_{\partial \Omega_V} \psi \left( \mathbf{u} \cdot \mathbf{n} \right) dS + \int_{\Gamma} \psi_V \left( \dot{x}_{\Gamma} \cdot (-\mathbf{n}_{\Gamma}) \right) dS$$
 (B.1b)

On adding both these equations, a transport equation for  $\psi$  is obtained for the entire material volume, given by,

$$\frac{\mathrm{d}}{\mathrm{d}t} \int_{\Omega} \psi dV = \int_{\Omega} \frac{\partial \psi}{\partial t} dV + \int_{\partial \Omega} \psi \left( \mathbf{u} \cdot \mathbf{n} \right) dS + \int_{\Gamma} \left( \psi_L - \psi_V \right) \left( \dot{x}_{\Gamma} \cdot \mathbf{n}_{\Gamma} \right) dS. \tag{B.2}$$

If figure B.1 is treated as a *control volume* then it's salient features are:

•  $\partial\Omega_L$  and  $\partial\Omega_V$  are static surfaces, and

•  $\Gamma$  is a surface of discontinuity within the volume  $\Omega = \Omega_L \cup \Omega_V$ . This implies that  $\Omega_L$  and  $\Omega_V$  are not control volumes.

Similar to Eq. (B.1), we can now write the conservation equation for  $\psi$  as,

$$\frac{\mathrm{d}}{\mathrm{d}t} \int_{\Omega_{L,i}} \psi dV = \int_{\Omega_{L,i}} \frac{\partial \psi}{\partial t} dV + \int_{\Gamma} \psi_L \left( \dot{x}_{\Gamma} \cdot \mathbf{n}_{\Gamma} \right) dS, \quad \text{and} \quad (B.3a)$$

$$\frac{\mathrm{d}}{\mathrm{d}t} \int_{\Omega_{V,i}} \psi dV = \int_{\Omega_{V,i}} \frac{\partial \psi}{\partial t} dV + \int_{\Gamma} \psi_V \left( \dot{x}_{\Gamma} \cdot (-\mathbf{n}_{\Gamma}) \right) dS. \tag{B.3b}$$

On adding both these equations, a transport equation for  $\psi$  is obtained for the entire control volume, given by,

$$\frac{\mathrm{d}}{\mathrm{d}t} \int_{\Omega_i} \psi dV = \int_{\Omega_i} \frac{\partial \psi}{\partial t} dV + \int_{\Gamma} (\psi_L - \psi_V) \left( \dot{x}_\Gamma \cdot \mathbf{n}_\Gamma \right) dS. \tag{B.4}$$

By considering a material volume which coincides with a stationary control volume at an instant of time, a relation between the transport equation of a *material volume* given by Eq. (B.2) and *control volume* given by Eq. (B.4) can be established. This is given by,

$$\frac{\mathrm{d}}{\mathrm{d}t} \int_{\Omega} \psi dV = \frac{\mathrm{d}}{\mathrm{d}t} \int_{\Omega_i} \psi dV + \int_{\partial \Omega_i} \psi \left( \mathbf{u} \cdot \mathbf{n} \right) dS. \tag{B.5}$$

## B.2 Generalized equation for velocity divergence for a Material Volume

Without phase change,  $\nabla \cdot \mathbf{u}$  or  $\int_{\partial \Omega_i} \mathbf{u} \cdot \mathbf{n} dS$  is equal to zero for two incompressible fluids in the bulk phases as well as across the interface. This does not hold true for phase change. For

a material volume enclosing a liquid-vapor interface, the velocity divergence can be written as,

$$\int_{\partial\Omega_i} \mathbf{u} \cdot \mathbf{n} dS = \int_{\partial\Omega_V} \mathbf{u}_V \cdot \mathbf{n} dS + \int_{\partial\Omega_L} \mathbf{u}_L \cdot \mathbf{n} dS.$$
 (B.6)

On adding and subtracting the vapor and liquid side integrals near the interface in Eq. (B.6) gives,

$$\int_{\partial\Omega_i} \mathbf{u} \cdot \mathbf{n} dS = \int_{\partial\Omega_V} \mathbf{u}_V \cdot \mathbf{n} dS + \int_{\Gamma} \mathbf{u}_{V,\Gamma} \cdot (-\mathbf{n}_{\Gamma}) dS$$
(B.7)

$$+ \int_{\partial \Omega_L} \mathbf{u}_L \cdot \mathbf{n}_{\Gamma} dS + \int_{\Gamma} \mathbf{u}_{L,\Gamma} \cdot \mathbf{n}_{\Gamma} dS$$
 (B.8)

$$-\int_{\Gamma} \mathbf{u}_{L,\Gamma} \cdot \mathbf{n} dS - \int_{\Gamma} \mathbf{u}_{V,\Gamma} \cdot (-\mathbf{n}_{\Gamma}) dS.$$
 (B.9)

Here  $\mathbf{n}_{\Gamma}$  is the interface normal pointing from liquid to vapor. Combining like integrals gives,

$$\int_{\partial\Omega_i} \mathbf{u} \cdot \mathbf{n} dS = \int_{\partial\Omega_V \cup \Gamma} \mathbf{u}_V \cdot \mathbf{n} dS + \int_{\partial\Omega_L \cup \Gamma} \mathbf{u}_L \cdot \mathbf{n} dS + \int_{\Gamma} (\mathbf{u}_V - \mathbf{u}_L)_{\Gamma} \cdot \mathbf{n}_{\Gamma} dS.$$
 (B.10)

Considering that both liquid and vapor phases are incompressible, an integral completely surrounding the liquid and vapor phases will be equal to zero. Hence, Eq. (B.10) simplifies to,

$$\int_{\partial\Omega_i} \mathbf{u} \cdot \mathbf{n} dS = \int_{\Gamma} (\mathbf{u}_V - \mathbf{u}_L)_{\Gamma} \cdot \mathbf{n}_{\Gamma} dS.$$
 (B.11)

Expressions for  $(\mathbf{u}_{V,\Gamma} \cdot \mathbf{n}_{\Gamma})$  and  $(\mathbf{u}_{L,\Gamma} \cdot \mathbf{n}_{\Gamma})$  are obtained from Eq. (4.1a) and substituted in Eq. (B.12) to give,

$$\int_{\partial\Omega_i} \mathbf{u} \cdot \mathbf{n} dS = \left(\frac{1}{\rho_V} - \frac{1}{\rho_L}\right) \int_{\Gamma} \dot{m}'' dS. \tag{B.12}$$

In cases without phase change  $\dot{m}''$  will be equal to zero at the interface and divergence of velocity will be zero throughout the domain as expected.

## B.3 Jump in pressure gradient at the interface due to phase change

Consider an interfacial control volume as shown in figure B.2. If the liquid in this volume

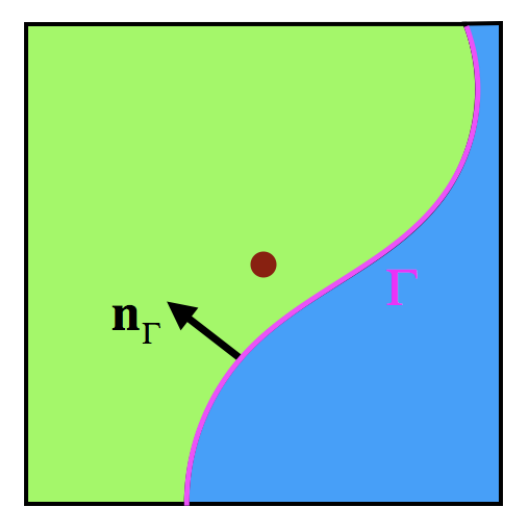


Figure B.2: Control volume  $(\Omega_i)$  that includes an interface between the liquid (blue) and vapor (green) phases. The red dot denotes the center of the control volume.

is assumed to be behave as ghost vapor, the momentum equation for such a volume can be

written as,

$$\frac{\mathrm{d}}{\mathrm{d}t} \int_{\Omega_i} \mathbf{u}_V dV + \int_{\partial\Omega_i} \mathbf{u}_V \left( \mathbf{u}_V \cdot \mathbf{n} \right) dS = -\frac{1}{\rho_V} \int_{\Omega_i} \nabla p_V dV, \tag{B.13}$$

where viscous and body forces have been assumed to be zero, and  $\partial\Omega_i$  refers to the boundary of the control volume. In the same way, if vapor is assumed to behave as a ghost liquid, a liquid momentum equation can be written for the same volume as,

$$\frac{\mathrm{d}}{\mathrm{d}t} \int_{\Omega_i} \mathbf{u}_L dV + \int_{\partial\Omega_i} \mathbf{u}_L \left( \mathbf{u}_L \cdot \mathbf{n} \right) dS = -\frac{1}{\rho_L} \int_{\Omega_i} \nabla p_L dV, \tag{B.14}$$

Subtracting Eq. (B.13) from Eq. (B.14) and rearranging the terms, we can write,

$$\int_{\Omega_{i}} \left( \frac{\nabla p_{V}}{\rho_{V}} - \frac{\nabla p_{L}}{\rho_{L}} \right) dV = \frac{\mathrm{d}}{\mathrm{d}t} \int_{\Omega_{i}} \left( \mathbf{u}_{L} - \mathbf{u}_{V} \right) dV + \int_{\partial\Omega_{i}} \left( \mathbf{u}_{L} \left( \mathbf{u}_{L} \cdot \mathbf{n} \right) - \mathbf{u}_{V} \left( \mathbf{u}_{V} \cdot \mathbf{n} \right) \right) dS. \tag{B.15}$$

Both liquid and vapor values are assumed to be known at all points either directly from fluid property or evaluated as a ghost value. The relation that defines the difference between liquid and vapor velocity at a location can be obtained from Eq. (4.1a) given by,

$$\llbracket \mathbf{u} \rrbracket = \mathbf{u}_{V}(\mathbf{x}, t) - \mathbf{u}_{L}(\mathbf{x}, t) = \dot{m}''(\mathbf{x}, t) \left( \frac{1}{\rho_{V}} - \frac{1}{\rho_{L}} \right) \mathbf{n}_{\Gamma}.$$
 (B.16)

This equation takes the assumption that tangential velocity along the interface remain con-

tinuous between liquid and vapor phases, which is mathematically summarized as,

$$\mathbf{u}_{L} - (\mathbf{u}_{L} \cdot \mathbf{n}_{\Gamma}) \, \mathbf{n}_{\Gamma} = \mathbf{u}_{V} - (\mathbf{u}_{V} \cdot \mathbf{n}_{\Gamma}) \, \mathbf{n}_{\Gamma}. \tag{B.17}$$

To enforce Eq. (B.16) away from the interface, the interfacial values of mass flux due to phase change  $(\dot{m}'')$  and interface normal  $(\mathbf{n}_{\Gamma})$  must be extended in the entire volume. It is assumed that these quantities are known at all locations,  $\mathbf{x} \in \Omega_i$ , using a constant normal-wise extrapolation given by,

$$\frac{\partial \dot{m}''}{\partial n_{\Gamma}} = 0. \tag{B.18}$$

On substituting Eq. (B.16) in Eq. (B.15) we get,

$$\int_{\Omega_{i}} \left( \frac{\nabla p_{V}}{\rho_{V}} - \frac{\nabla p_{L}}{\rho_{L}} \right) dV = -\frac{\mathrm{d}}{\mathrm{d}t} \int_{\Omega_{i}} \dot{m}'' \left( \frac{1}{\rho_{V}} - \frac{1}{\rho_{L}} \right) \mathbf{n}_{\Gamma} dV 
+ \int_{\partial\Omega_{i}} \left( \mathbf{u}_{L} \left( \mathbf{u}_{L} \cdot \mathbf{n} \right) - \left( \mathbf{u}_{L} + \dot{m}'' \left( \frac{1}{\rho_{V}} - \frac{1}{\rho_{L}} \right) \mathbf{n}_{\Gamma} \right) \left( \left( \mathbf{u}_{L} + \dot{m}'' \left( \frac{1}{\rho_{V}} - \frac{1}{\rho_{L}} \right) \mathbf{n}_{\Gamma} \right) \cdot \mathbf{n} \right) \right) dS.$$
(B.19)

The right hand side can be reduced to give,

$$\int_{\Omega_{i}} \left( \frac{\nabla p_{V}}{\rho_{V}} - \frac{\nabla p_{L}}{\rho_{L}} \right) dV = -\left( \frac{1}{\rho_{V}} - \frac{1}{\rho_{L}} \right) \frac{d}{dt} \int_{\Omega_{i}} \dot{\mathbf{m}}'' \mathbf{n}_{\Gamma} dV 
- \int_{\partial\Omega_{i}} \mathbf{u}_{L} \dot{\mathbf{m}}'' \left( \frac{1}{\rho_{V}} - \frac{1}{\rho_{L}} \right) (\mathbf{n}_{\Gamma} \cdot \mathbf{n}) dS 
- \int_{\partial\Omega_{i}} \dot{\mathbf{m}}'' \left( \frac{1}{\rho_{V}} - \frac{1}{\rho_{L}} \right) \mathbf{n}_{\Gamma} (\mathbf{u}_{L} \cdot \mathbf{n}) dS 
- \int_{\partial\Omega_{i}} \left( \dot{\mathbf{m}}'' \left( \frac{1}{\rho_{V}} - \frac{1}{\rho_{L}} \right) \right)^{2} \mathbf{n}_{\Gamma} (\mathbf{n}_{\Gamma} \cdot \mathbf{n}) dS$$
(B.20)

This is a vector equation and consequently the equality should specifically hold in the direction of the interface normal as well. Equation (B.20) written in the interface normal direction is given by,

$$\int_{\Omega_{i}} \left[ \frac{\nabla p}{\rho} \right] \cdot \mathbf{n}_{\Gamma} dV = -\left( \frac{1}{\rho_{V}} - \frac{1}{\rho_{L}} \right) \left( \frac{\mathrm{d}}{\mathrm{d}t} \int_{\Omega_{i}} \dot{m}'' dV - \int_{\partial\Omega_{i}} \left( \mathbf{u}_{L} \cdot \mathbf{n}_{\Gamma} \right) \dot{m}'' \left( \mathbf{n}_{\Gamma} \cdot \mathbf{n} \right) dS - \int_{\partial\Omega_{i}} \dot{m}'' \left( \mathbf{u}_{L} \cdot \mathbf{n} \right) dS - \int_{\partial\Omega_{i}} \left( \dot{m}'' \left( \frac{1}{\rho_{V}} - \frac{1}{\rho_{L}} \right) \right) \left( \mathbf{n}_{\Gamma} \cdot \mathbf{n} \right) dS \right). \tag{B.21}$$

Now, using the Gauss divergence theorem, the surface integrals on R.H.S. can be written as volume integrals to give,

$$\int_{\Omega_{i}} \left[ \left[ \frac{\nabla p}{\rho} \right] \right] \cdot \mathbf{n}_{\Gamma} dV = -\left( \frac{1}{\rho_{V}} - \frac{1}{\rho_{L}} \right) \left( \frac{\mathrm{d}}{\mathrm{d}t} \int_{\Omega_{i}} \dot{m}'' dV - \int_{\Omega_{i}} \nabla \cdot \left( u_{Ln} \dot{m}'' \mathbf{n}_{\Gamma} \right) dV - \int_{\Omega_{i}} \nabla \cdot \left( \dot{m}'' \mathbf{n}_{L} \right) dV - \left( \frac{1}{\rho_{V}} - \frac{1}{\rho_{L}} \right) \int_{\Omega_{i}} \nabla \cdot \left( \dot{m}'' \mathbf{n}_{\Gamma} \right) dV \right). \tag{B.22}$$

Here,  $u_{Ln} = \mathbf{u}_L \cdot \mathbf{n}_{\Gamma}$ .

In this equation, the last term refers to the divergence of mass flux in the interface normal direction, which is equal to zero due to Eq. (B.18). For the first divergence term on the R.H.S. of Eq. (B.22),

$$\nabla \cdot (u_{Ln}\dot{m}''\mathbf{n}_{\Gamma}) = \frac{\partial (u_{Ln}\dot{m}'')}{\partial n_{\Gamma}},$$

which can be further reduced due to Eq. (B.18) to give,

$$\nabla \cdot (u_{Ln}\dot{m}''\mathbf{n}_{\Gamma}) = \dot{m}''\frac{\partial u_{Ln}}{\partial n_{\Gamma}}.$$

Assuming that the size of control volume is small such that all points remain near the interface, we can approximate  $u_{Ln} = \dot{\mathbf{x}}_{\Gamma} \cdot \mathbf{n}_{\Gamma} + \dot{m}''/\rho_L$  due to Eq. (4.35a). On substituting this it can be shown that,

$$\nabla \cdot (u_{Ln}\dot{m}''\mathbf{n}_{\Gamma}) \sim \dot{m}'' \frac{\partial \left(\dot{\mathbf{x}}_{\Gamma} \cdot \mathbf{n}_{\Gamma}\right)}{\partial n_{\Gamma}} + \frac{\dot{m}''}{\rho_{L}} \frac{\partial \dot{m}''}{\partial n_{\Gamma}}, \tag{B.23}$$

which is also equal to zero.

The remaining divergence term on the R.H.S. of Eq. (B.22) can be rewritten as,

$$\nabla \cdot (\dot{m}'' \mathbf{u}_L) = \mathbf{u}_L \cdot \nabla \dot{m}'' + \dot{m}'' \nabla \cdot \mathbf{u}_L. \tag{B.24}$$

Due to the incompressibility of liquid phase,  $\nabla \cdot \mathbf{u}_L = 0$  for the entire volume. To simplify the last remaining term on R.H.S. of Eq. (B.24), we first define an orthogonal coordinate system with directions,  $\mathbf{n}_{\Gamma}$ ,  $\mathbf{z}_1$  and  $\mathbf{z}_2$ . Using this system, that term can be written as,

$$\nabla \cdot (\dot{m}'' \mathbf{u}_L) = u_{t1} \frac{\partial \dot{m}''}{\partial z_1} + u_{t2} \frac{\partial \dot{m}''}{\partial z_2}.$$
 (B.25)

While this term is not equal to zero in general, for most practical applications related to bubble dynamics, the change in rate of mass flux along the interface tangent direction will be very small. Hence, it can also be neglected.

Considering that all three terms related to the advection of mass flux due to phase change in a generic interfacial control volume shown in figure B.2 are equal to zero, the jump in pressure gradient is found to be,

$$\left[ \left[ \frac{\nabla p}{\rho} \right] \right] \cdot \mathbf{n}_{\Gamma} = -\left( \frac{1}{\rho_V} - \frac{1}{\rho_L} \right) \frac{\mathrm{d}\dot{m}''}{\mathrm{d}t}. \tag{B.26}$$

## B.3.1 Test for the derived expression of jump in pressure gradient for vapor bubble

For a spherical vapor bubble with incompressible liquid and vapor phases, undergoing growth or collapse, Plesset [10] derived that,

$$\dot{m}'' = \rho_V \dot{R}, \text{ and}$$
 (B.27)

$$p_L(r,t) = p_{\infty}(t) + \rho_L \left( \frac{1}{r} \left( 2R\dot{R}^2 + R^2\ddot{R} \right) - \frac{1}{2} \left( \frac{R^4\dot{R}^2}{r^4} \right) \right).$$
 (B.28)

under the assumption that  $\rho_V \ll \rho_L$ . Due to vapor incompressibility, velocity of vapor inside the bubble is zero and the pressure is considered to be uniform. This implies that pressure gradient of vapor remains zero  $(\nabla p_V = 0)$ .

Due to the sign convention observed in this work, interface normal points from liquid to the vapor phase, and hence,  $\mathbf{n}_{\Gamma} = -\hat{r}$ . At first, we evaluate the left hand side of Eq. (B.26), which can be expressed as,

$$\left[ \left[ \frac{\nabla p}{\rho} \right] \right] \cdot \mathbf{n}_{\Gamma} = \left( \frac{\nabla p_V}{\rho_V} - \frac{\nabla p_L}{\rho_L} \right)_{\Gamma} \cdot \mathbf{n}_{\Gamma}. \tag{B.29}$$

Considering the spherical symmetry of the bubble system, this equation can be rewritten as,

$$\left[ \left[ \frac{\nabla p}{\rho} \right] \right] \cdot \mathbf{n}_{\Gamma} = \left( \frac{1}{\rho_{V}} \left. \frac{\partial p_{V}}{\partial r} \right|_{\Gamma} - \frac{1}{\rho_{L}} \left. \frac{\partial p_{L}}{\partial r} \right|_{\Gamma} \right) (\hat{\mathbf{r}}) \cdot (-\hat{\mathbf{r}}).$$
(B.30)

As noted earlier, the pressure gradient in the vapor phase remains zero. Pressure gradient on the liquid side can be evaluated from Eq. (B.28) at r = R(t). Equation (B.30) can thus be written as,

$$\left[ \left[ \frac{\nabla p}{\rho} \right] \cdot \mathbf{n}_{\Gamma} = -\left( -\frac{1}{\rho_L} \left( -\rho_L \ddot{R} \right) \right) = -\ddot{R}. \tag{B.31}$$

Hence, the jump in pressure gradient along the normal direction is proportional to the acceleration of bubble interface.

Now, evaluating the right hand side of Eq. (B.26) with the assumption that  $\rho_V \ll \rho_L$  gives,

$$-\left(\frac{1}{\rho_V} - \frac{1}{\rho_L}\right) \frac{\mathrm{d}\dot{m}''}{\mathrm{d}t} = -\frac{1}{\rho_V} \frac{\mathrm{d}\dot{m}''}{\mathrm{d}t}.$$
 (B.32)

On substituting the expression in Eq. (B.27) we get,

$$-\left(\frac{1}{\rho_V} - \frac{1}{\rho_L}\right) \frac{\mathrm{d}\dot{m}''}{\mathrm{d}t} = -\frac{1}{\rho_V} \left(\rho_V \ddot{R}\right) = -\ddot{R}.$$
 (B.33)

The final expression for both left and right hand sides of Eq. (B.26) simplifies to  $-\ddot{R}$ , which validates the derived expression for the jump in pressure gradient along the normal direction of an interface undergoing phase change for a spherical bubble.

### Appendix C

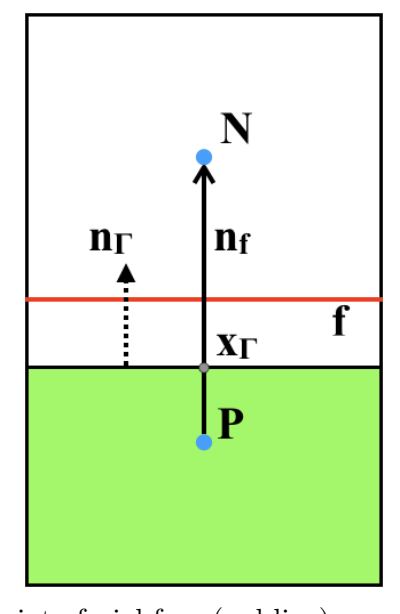
### Derivations for Ghost Fluid Method

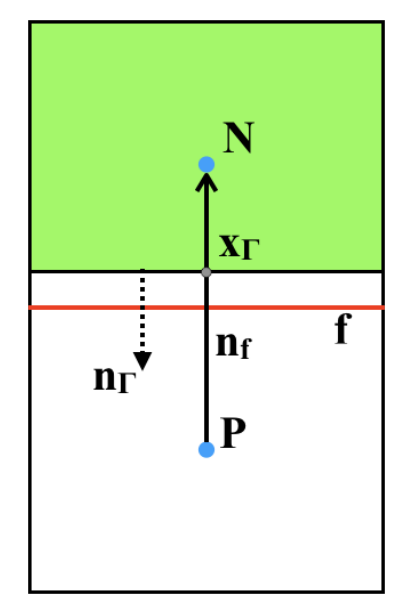
In this section, we derive the expressions for ghost values of a general variable Z, which is characterized by the following jump conditions at the interface:

$$[\![Z]\!]_{\Gamma} = Z_{V,\Gamma} - Z_{L,\Gamma} = \Delta Z,$$
 and (C.1a)

$$[\![\eta \nabla Z]\!]_{\Gamma} \cdot \mathbf{n}_{\Gamma} = (\eta_V \nabla Z_V - \eta_L \nabla Z_L)_{\Gamma} \cdot \mathbf{n}_{\Gamma} = \delta_{\Gamma}.$$
 (C.1b)

A ghost value is needed in the adjacent computational volume if a cell face lies between a liquid and a vapor cell. Such faces are termed as interfacial faces identified by Eq. (4.33). Graphical representation of such a system is shown in figure C.1a and figure C.1b. In the case of figure C.1a, the pressure and velocity values stored at cell - center P belong to the liquid phase, and those stored at the cell - center N belong to the vapor phase. To obtain a liquid or vapor, velocity or pressure value at face f requires interpolation between cells P and N with values belonging to the same phase. Hence, a ghost liquid must be defined for





(a) An interfacial face (red line) owned by a liquid cell (P) and shared by a neighbor vapor cell (N).

(b) An interfacial face (red line) owned by a vapor cell (P) and shared by a neighbor liquid cell (N).

Figure C.1: Graphical representation of an interfacial face. In both figures, interface normal  $(\mathbf{n}_{\Gamma})$  points from liquid to vapor phase, and face normal  $(\mathbf{n}_{f})$  faces from the owner cell (P) to neighbor cell (N).

cell N and similarly a ghost vapor for cell P. The same holds true for figure C.1b.

Note that the interface is represented with a line parallel to the face. This is a simplifying assumption for the Ghost Fluid Method. In all the following calculations, we primarily use the jump in discontinuities along the face normal,  $\mathbf{n}_f$ . Distance of the interface is stored as a ratio given by,

$$\frac{\overline{P\Gamma}}{\overline{PN}} = \frac{\mathbf{x}_{\Gamma} - \mathbf{x}_{P}}{\mathbf{x}_{N} - \mathbf{x}_{P}} \sim \frac{\alpha_{P} - 0.5}{\alpha_{P} - \alpha_{N}} = \lambda_{j}.$$
 (C.2)

This is similar to another Ghost Fluid work by Vukčević et al. [112]. The position of  $\mathbf{x}_{\Gamma}$  is assumed to coincide with the iso-surface  $\alpha = 0.5$  for the purpose of pressure and velocity calculations using GFM.

# C.1 Ghost values related to an interfacial face owned by liquid cell

This situation is represented by figure C.1a. Firstly, using the gradient jump condition given by Eq. (C.1b), an expression for the value of  $Z_{\Gamma}$  can be obtained in terms of the known values,  $Z_P$ ,  $Z_N$ ,  $\Delta Z_{\Gamma}$ ,  $\lambda_j$ , and  $\delta_{\Gamma}$ .

Using OpenFOAM terminology, each face has a designated owner cell, and a neighbor cell. The sign convention dictates that the face normal  $(\mathbf{n}_f)$ , faces from its owner to the neighbor. With this sign convention, a discrete form of Eq. (C.1b) can be written as,

$$\eta_V \frac{Z_N - Z_{V,\Gamma}}{(1 - \lambda_j) \Delta x} - \eta_L \frac{Z_{L,\Gamma} - Z_P}{\lambda_j \Delta x} = \delta_{\Gamma}. \tag{C.3}$$

Rearranging this equation,

$$\lambda_{j}\eta_{V}\left(Z_{N}-Z_{V,\Gamma}\right)-\eta_{L}\left(1-\lambda_{j}\right)\left(Z_{L,\Gamma}-Z_{P}\right)=\delta_{\Gamma}\left(1-\lambda_{j}\right)\lambda_{j}\Delta x.\tag{C.4}$$

Substitute Eq. (C.1a) in the above equation to give,

$$\lambda_{i}\eta_{V}\left(Z_{N}-Z_{L,\Gamma}-\Delta Z_{\Gamma}\right)-\eta_{L}\left(1-\lambda_{i}\right)\left(Z_{L,\Gamma}-Z_{P}\right)=\delta_{\Gamma}\left(1-\lambda_{i}\right)\lambda_{i}\Delta x.\tag{C.5}$$

Collecting all the  $Z_{L,\Gamma}$  values on the left hand side gives,

$$(\lambda_{j}\eta_{V} + (1 - \lambda_{j}) \eta_{L}) Z_{L,\Gamma} = \lambda_{j}\eta_{V} Z_{N} + (1 - \lambda_{j}) \eta_{L} Z_{P} - \lambda_{j}\eta_{V} \Delta Z_{\Gamma} - \delta_{\Gamma} (1 - \lambda_{j}) \lambda_{j} \Delta x.$$
(C.6)

The final expression for  $Z_{L,\Gamma}$  can be written as,

$$Z_{L,\Gamma} = \lambda_j \frac{\eta_V}{\eta_i^*} Z_N + (1 - \lambda_j) \frac{\eta_L}{\eta_i^*} Z_P - \lambda_j \frac{\eta_V}{\eta_i^*} \Delta Z_\Gamma - (1 - \lambda_j) \lambda_j \frac{1}{\eta_i^*} \delta_\Gamma \Delta x, \tag{C.7}$$

where  $\eta_j^* = (\lambda_j \eta_V + (1 - \lambda_j) \eta_L)$ . The vapor side value at the interface can be obtained by adding  $\Delta Z_{\Gamma}$  to Eq. (C.7), which gives,

$$Z_{V,\Gamma} = \lambda_j \frac{\eta_V}{\eta_i^*} Z_N + (1 - \lambda_j) \frac{\eta_L}{\eta_i^*} Z_P + (1 - \lambda_j) \frac{\eta_L}{\eta_i^*} \Delta Z_\Gamma - (1 - \lambda_j) \lambda_j \frac{1}{\eta_i^*} \delta_\Gamma \Delta x, \tag{C.8}$$

#### Liquid value in cell N

Using Taylor series expansion the liquid value evaluated at the interface in Eq. (C.7) can be extrapolated to the vapor cell N. The expansion is written out as,

$$\left(Z_L^{ghost}\right)_N = Z_{L,\Gamma} + \left(\left(\mathbf{x}_N - \mathbf{x}_{\Gamma}\right) \cdot \mathbf{n}_{\Gamma}\right) \frac{\partial Z_L}{\partial \mathbf{n}_f}.$$
(C.9)

Substituting the distance of cell-center N from the interface, and writing the derivative in discrete form, gives,

$$\left(Z_L^{ghost}\right)_N = Z_{L,\Gamma} + (1 - \lambda_j) \, \Delta x \left(\frac{Z_{L,\Gamma} - Z_P}{\lambda_j \Delta x}\right).$$
(C.10)

On rearranging and substituting the expression for  $Z_{L,\Gamma}$  from Eq. (C.7), we get,

$$\left(Z_L^{ghost}\right)_N = \frac{1}{\lambda_j} \left(\lambda_j \frac{\eta_V}{\eta_j^*} Z_N + (1 - \lambda_j) \frac{\eta_L}{\eta_j^*} Z_P - \lambda_j \frac{\eta_V}{\eta_j^*} \Delta Z_\Gamma - (1 - \lambda_j) \lambda_j \frac{1}{\eta_j^*} \delta_\Gamma \Delta x\right) - \frac{1 - \lambda_j}{\lambda_j} Z_P.$$
(C.11)

Collecting like terms, adding and subtracting  $Z_N$ , gives,

$$\left(Z_L^{ghost}\right)_N = Z_N + \left\{\frac{1-\lambda_j}{\lambda_j} \left(\frac{\eta_L}{\eta_j^*} - 1\right) Z_P + \left(\frac{\eta_V}{\eta_j^*} - 1\right) Z_N\right\} - \frac{\eta_V}{\eta_j^*} \Delta Z_\Gamma - (1-\lambda_j) \frac{1}{\eta_j^*} \delta_\Gamma \Delta x. \tag{C.12}$$

Interestingly, the term within  $\{...\}$  can be considerably simplified to give a final form for  $\left(Z_L^{ghost}\right)_N$  as,

$$\left(Z_L^{ghost}\right)_N = Z_N + (1 - \lambda_j) \frac{\eta_L - \eta_V}{\eta_j^*} \left(Z_P - Z_N\right) - \frac{\eta_V}{\eta_j^*} \Delta Z_\Gamma - (1 - \lambda_j) \frac{1}{\eta_j^*} \delta_\Gamma \Delta x. \tag{C.13}$$

#### Vapor value in cell P

Using Taylor series expansion the vapor value evaluated at the interface in Eq. (C.8) can be extrapolated to the liquid cell P. The expansion is written out as,

$$\left(Z_V^{ghost}\right)_P = Z_{V,\Gamma} + \left(\left(\mathbf{x}_P - \mathbf{x}_{\Gamma}\right) \cdot \mathbf{n}_{\Gamma}\right) \frac{\partial Z_V}{\partial \mathbf{n}_f}.$$
(C.14)

Substituting the distance of cell-center P from the interface, and writing the derivative in discrete form, gives,

$$\left(Z_V^{ghost}\right)_P = Z_{V,\Gamma} - \lambda_j \Delta x \frac{Z_N - Z_{V,\Gamma}}{(1 - \lambda_j) \Delta x}.$$
(C.15)

On rearranging and substituting the expression for  $Z_{V,\Gamma}$  from Eq. (C.8), we get,

$$\left(Z_V^{ghost}\right)_P = \frac{1}{1-\lambda_j} \left(\lambda_j \frac{\eta_V}{\eta_j^*} Z_N + (1-\lambda_j) \frac{\eta_L}{\eta_j^*} Z_P + (1-\lambda_j) \frac{\eta_L}{\eta_j^*} \Delta Z_\Gamma - (1-\lambda_j) \lambda_j \frac{1}{\eta_j^*} \delta_\Gamma \Delta x\right) - \frac{\lambda_j}{1-\lambda_j} Z_N.$$
(C.16)

Collecting like terms, adding and subtracting  $Z_P$ , gives,

$$\left(Z_V^{ghost}\right)_P = Z_P + \left\{ \left(\frac{\eta_L}{\eta_j^*} - 1\right) Z_P + \frac{\lambda_j}{1 - \lambda_j} \left(\frac{\eta_V}{\eta_j^*} - 1\right) Z_N \right\} + \frac{\eta_L}{\eta_j^*} \Delta Z_\Gamma - \lambda_j \frac{1}{\eta_j^*} \delta_\Gamma \Delta x. \tag{C.17}$$

Similar to Eq. (C.13), the term within  $\{...\}$  can be considerably simplified to give a final form for  $\left(Z_V^{ghost}\right)_P$  as,

$$\left(Z_V^{ghost}\right)_P = Z_P + \lambda_j \frac{\eta_L - \eta_V}{\eta_j^*} \left(Z_P - Z_N\right) + \frac{\eta_L}{\eta_j^*} \Delta Z_\Gamma - \lambda_j \frac{1}{\eta_j^*} \delta_\Gamma \Delta x. \tag{C.18}$$

## C.2 Ghost values related to an interfacial face owned by vapor cell

A similar analysis is done for the case shown in figure C.1b, where the interfacial face is owned by a cell that is tagged as vapor. Due to the direction of face normal pointing opposite to interface normal and  $\lambda_j \Delta x$  defined as the distance between vapor cell & interface, all the expressions obtained in the previous section are somewhat modified.

In its discrete form, Eq. (C.1b) can be written as,

$$\eta_V \frac{Z_{V,\Gamma} - Z_P}{\lambda_j \Delta x} - \eta_L \frac{Z_N - Z_{L,\Gamma}}{(1 - \lambda_j) \Delta x} = -\delta_{\Gamma}.$$
 (C.19)

The negative sign on the R.H.S. is because  $\mathbf{n}_{\Gamma} \cdot \mathbf{n}_f < 0$ , when the owner of interfacial face is a vapor cell. Rearranging above equation gives,

$$(1 - \lambda_j) \eta_V (Z_{V,\Gamma} - Z_P) - \lambda_j \eta_L (Z_N - Z_{L,\Gamma}) = -\delta_\Gamma (1 - \lambda_j) \lambda_j \Delta x.$$
 (C.20)

Substitute Eq. (C.1a) in the above equation to give,

$$(1 - \lambda_i) \eta_V (Z_{L,\Gamma} + \Delta Z_{\Gamma} - Z_P) - \lambda_i \eta_L (Z_N - Z_{L,\Gamma}) = -\delta_{\Gamma} (1 - \lambda_i) \lambda_i \Delta x. \tag{C.21}$$

Collecting all the  $Z_{L,\Gamma}$  values on the left hand side gives,

$$(\lambda_{j}\eta_{L} + (1 - \lambda_{j}) \eta_{V}) Z_{L,\Gamma} = (1 - \lambda_{j}) \eta_{V} Z_{P} + \lambda_{j} \eta_{L} Z_{N} - (1 - \lambda_{j}) \eta_{V} \Delta Z_{\Gamma} - \delta_{\Gamma} (1 - \lambda_{j}) \lambda_{j} \Delta x.$$
(C.22)

The final expression for  $Z_{L,\Gamma}$  can be written as,

$$Z_{L,\Gamma} = (1 - \lambda_j) \frac{\eta_V}{\eta_j^{**}} Z_P + \lambda_j \frac{\eta_L}{\eta_j^{**}} Z_N - (1 - \lambda_j) \frac{\eta_V}{\eta_j^{**}} \Delta Z_\Gamma - \delta_\Gamma \frac{1}{\eta_j^{**}} (1 - \lambda_j) \lambda_j \Delta x, \qquad (C.23)$$

where  $\eta_j^{**} = (\lambda_j \eta_L + (1 - \lambda_j) \eta_V)$ . The vapor side value at the interface can be obtained by adding  $\Delta Z_{\Gamma}$  to Eq. (C.23), which gives,

$$Z_{V,\Gamma} = (1 - \lambda_j) \frac{\eta_V}{\eta_j^{**}} Z_P + \lambda_j \frac{\eta_L}{\eta_j^{**}} Z_N + \lambda_j \frac{\eta_L}{\eta_j^{**}} \Delta Z_\Gamma - \delta_\Gamma \frac{1}{\eta_j^{**}} (1 - \lambda_j) \lambda_j \Delta x, \tag{C.24}$$

Not repeating the analysis presented in  $\S(C.1)$  for the same cases when the owner of interfacial face is a vapor cell, we directly write out the final expressions. In this case, the owner cell P is populated with a ghost liquid value, while the neighbor cell N is populated with a ghost vapor value. These values are given by,

$$\left(Z_L^{ghost}\right)_P = Z_P + \lambda_j \frac{\eta_V - \eta_L}{\eta_j^{**}} \left(Z_P - Z_N\right) - \frac{\eta_V}{\eta_j^{**}} \Delta Z_\Gamma - \frac{1}{\eta_j^{**}} \delta_\Gamma \lambda_j \Delta x, \quad \text{and} \quad (C.25)$$

$$\left( Z_V^{ghost} \right)_N = Z_N + (1 - \lambda_j) \frac{\eta_V - \eta_L}{\eta_j^{**}} \left( Z_P - Z_N \right) + \frac{\eta_L}{\eta_j^{**}} \Delta Z_\Gamma - \frac{1}{\eta_j^{**}} \delta_\Gamma \left( 1 - \lambda_j \right) \Delta x$$
 (C.26)

#### C.3 Interpolated values at interfacial face

Based on the four separate ghost value expressions obtained from Eq. (C.13), Eq. (C.18), Eq. (C.25), and Eq. (C.26), Z can now be interpolated to get a liquid and vapor value at the interfacial faces. These values are given by,

1. Liquid value at the interfacial face when face is owned by a liquid cell

$$(Z_L)_j^* = rac{Z_P + \left(Z_L^{ghost}\right)_N}{2},$$

which can be rewritten with substitution from Eq. (C.13) to give,

$$(Z_L)_j^* = (1 - \lambda_j) \frac{\eta_L - \eta_V}{\eta_j^*} Z_P + \frac{\eta_V}{\eta_j^*} \frac{Z_P + (Z_N - \Delta Z_\Gamma)}{2} - \frac{1}{2} \frac{1}{\eta_j^*} \delta_\Gamma (1 - \lambda_j) \Delta x. \quad (C.27)$$

2. Vapor value at the interfacial face when face is owned by a liquid cell

$$(Z_V)_j^* = \frac{Z_N + \left(Z_V^{ghost}\right)_P}{2},$$

which can be rewritten with substitution from Eq. (C.18) to give,

$$(Z_V)_j^* = -\lambda_j \frac{\eta_L - \eta_V}{\eta_j^*} Z_N + \frac{\eta_L}{\eta_j^*} \frac{(Z_P + \Delta Z_\Gamma) + Z_N}{2} - \frac{1}{2} \frac{1}{\eta_j^*} \delta_\Gamma \lambda_j \Delta x.$$
 (C.28)

3. Liquid value at the interfacial face when face is owned by a vapor cell

$$(Z_L)_j^{**} = \frac{Z_N + \left(Z_L^{ghost}\right)_P}{2},$$

which can be rewritten with substitution from Eq. (C.25) to give,

$$(Z_L)_j^* = -\lambda_j \frac{\eta_V - \eta_L}{\eta_j^{**}} Z_N + \frac{\eta_V}{\eta_j^{**}} \frac{(Z_P - \Delta Z_\Gamma) + Z_N}{2} - \frac{1}{2} \frac{1}{\eta_j^{**}} \delta_\Gamma \lambda_j \Delta x.$$
 (C.29)

4. Vapor value at the interfacial face when face is owned by a vapor cell

$$(Z_V)_j^{**} = \frac{Z_P + \left(Z_V^{ghost}\right)_N}{2},$$

which can be rewritten with substitution from Eq. (C.26) to give,

$$(Z_V)_j^* = (1 - \lambda_j) \frac{\eta_V - \eta_L}{\eta_i^{**}} Z_P + \frac{\eta_L}{\eta_i^{**}} \frac{Z_P + (Z_N + \Delta Z_\Gamma)}{2} - \frac{1}{2} \frac{1}{\eta_i^{**}} \delta_\Gamma (1 - \lambda_j) \Delta x. \quad (C.30)$$

#### C.4 Gradient calculations at interfacial face

Using the owner-neighbor values for individual phases, we can evaluate both liquid and vapor gradient at an interfacial face. These expression are given by,

1. Liquid value at the interfacial face when face is owned by a liquid cell

$$\left(\nabla_j^{\perp} Z\right)_L^* = \frac{\left(Z_L^{ghost}\right)_N - Z_P}{\Delta x},$$

which can be rewritten with substitution from Eq. (C.13) to give,

$$\left(\nabla_{j}^{\perp}Z\right)_{L}^{*} = \frac{\eta_{V}}{\eta_{j}^{*}} \left(\frac{Z_{N} - Z_{P}}{\Delta x}\right) + \frac{\eta_{V}}{\eta_{j}^{*}} \left(\frac{0 - \Delta Z_{\Gamma}}{\Delta x}\right) - \frac{1}{\eta_{j}^{*}} \delta_{\Gamma} \left(1 - \lambda_{j}\right). \tag{C.31}$$

2. Vapor value at the interfacial face when face is owned by a liquid cell

$$\left(\nabla_j^{\perp} Z\right)_V^* = \frac{Z_N - \left(Z_V^{ghost}\right)_P}{\Delta x},$$

which can be rewritten with substitution from Eq. (C.18) to give,

$$\left(\nabla_j^{\perp} Z\right)_V^* = \frac{\eta_L}{\eta_j^*} \left(\frac{Z_N - Z_P}{\Delta x}\right) + \frac{\eta_L}{\eta_j^*} \left(\frac{0 - \Delta Z_{\Gamma}}{\Delta x}\right) + \frac{1}{\eta_j^*} \delta_{\Gamma} \lambda_j. \tag{C.32}$$

3. Liquid value at the interfacial face when face is owned by a vapor cell

$$\left(\nabla_j^{\perp} Z\right)_L^{**} = \frac{Z_N - \left(Z_L^{ghost}\right)_P}{\Delta x},$$

which can be rewritten with substitution from Eq. (C.25) to give,

$$\left(\nabla_j^{\perp} Z\right)_L^{**} = \frac{\eta_V}{\eta_j^{**}} \left(\frac{Z_N - Z_P}{\Delta x}\right) + \frac{\eta_V}{\eta_j^{**}} \left(\frac{\Delta Z_\Gamma - 0}{\Delta x}\right) + \frac{1}{\eta_j^{**}} \delta_{\Gamma} \lambda_j. \tag{C.33}$$

4. Vapor value at the interfacial face when face is owned by a vapor cell

$$\left(\nabla_j^{\perp} Z\right)_V^{**} = \frac{\left(Z_V^{ghost}\right)_N - Z_P}{\Delta x},$$

which can be rewritten with substitution from Eq. (C.26) to give,

$$\left(\nabla_{j}^{\perp}Z\right)_{V}^{**} = \frac{\eta_{L}}{\eta_{j}^{**}} \left(\frac{Z_{N} - Z_{P}}{\Delta x}\right) + \frac{\eta_{L}}{\eta_{j}^{**}} \left(\frac{\Delta Z_{\Gamma} - 0}{\Delta x}\right) - \frac{1}{\eta_{j}^{**}} \delta_{\Gamma} \left(1 - \lambda_{j}\right). \tag{C.34}$$

## **Bibliography**

- [1] Raunak Bardia and Mario F Trujillo. Assessing the physical validity of highly-resolved simulation benchmark tests for flows undergoing phase change. *International Journal of Multiphase Flow*, 112:52–62, 2019.
- [2] Douglas T. Ryddner and Mario F. Trujillo. Modeling Urea-Water Solution Droplet Evaporation. Emission Control Science and Technology, 1:80–97, 2015.
- [3] Raunak Bardia and Mario F Trujillo. An improved categorization of vapor bubble collapse: Explaining the coupled nature of hydrodynamic and thermal mechanisms.

  International Journal of Heat and Mass Transfer, 145:118754, 2019.
- [4] E. Ruckenstein. On heat transfer between vapour bubbles in motion and the boiling liquid from which they are generated. *Chemical Engineering Science*, 10:22–30, 1959.
- [5] Glen Edward Thorncroft. Heat Transfer and Vapor Bubble Dynamics in Forced Convection Boiling. PhD thesis, University of Florida, 1997.
- [6] V. K. Dhir. Boiling heat transfer. Annual Review of Fluid Mechanics, 30:365–401, 1998.

- [7] Jungho Kim. Review of nucleate pool boiling bubble heat transfer mechanisms. *International Journal of Multiphase Flow*, 35:1067–1076, 2009.
- [8] Lord Rayleigh. On the pressure developed in a liquid during the collapse of a spherical cavity. *Philosophical Magazine Series* 6, 34:94–98, 1917.
- [9] R. T. Knapp and A. Hollander. Laboratory investigations of the mechanism of cavitation. *Transaction of the ASME*, 1948.
- [10] Milton S. Plesset. The dynamics of cavitation bubbles. Journal of Applied Mechanics, pages 277–282, 1949.
- [11] Eric Johnsen and Tim Colonius. Numerical simulations of non-spherical bubble collapse. *Journal of Fluid Mechanics*, 629:231–262, 2009.
- [12] Christopher E. Brennen. Cavitation and bubble dynamics. Cambridge University Press, 2003.
- [13] Parag R. Gogate and Abhijeet M. Kabadi. A review of applications of cavitation in biochemical engineering/biotechnology. *Biochemical Engineering Journal*, 44:60–72, 2009.
- [14] Satish G. Kandlikar. History, advances, and challenges in liquid flow and flow boiling heat transfer in microchannels: A critical review. *Journal of Heat Transfer*, 134:034001, 2012.
- [15] Chirag R. Kharangate and Isaam Mudawar. Review of computational studies on boiling

- and condensation. International Journal of Heat and Mass Transfer, 108:1164–1196, 2017.
- [16] Y. T. Shah, B. G. Kelkar, S. P. Godbole, and W. D. Deckwer. Design parameters estimations for bubble column reactors. AIChE Journal, 28:353–379, 1982.
- [17] Nigar Kantarci, Fahir Borak, and Kutlu O. Ulgen. Bubble column reactors. Process Biochemistry, 40:2263–2283, 2005.
- [18] Christopher Earls Brennen. Cavitation in medicine. *Interface Focus*, 5(5):20150022, 2015.
- [19] Paul Dergarbedian. Observations on bubble growths in various superheated liquids.

  \*Journal of Fluid Mechanics\*, 9:39–48, 1960.
- [20] L. W. Florschuetz and B. T. Chao. On the mechanics of Vapor Bubble Collapse. Journal of Heat Transfer, 87:209–220, 1965.
- [21] Robert Cole and Herman L. Shulman. Bubble growth rates at high jakob numbers.

  International Journal of Heat and Mass Transfer, 9:1377–1390, 1966.
- [22] F. C. Hooper and A. H. Abdelmessih. The flashing of liquids at higher superheats. Chemical Engineering Progress, 62:83, 1966.
- [23] D. D. Wittke and B. T. Chao. Collapse of vapor bubbles with translatory motion. Journal of Heat Transfer, 89(1):17–24, 1967.
- [24] P.G. Kosky. Bubble growth measurements in uniformly superheated liquids. Chemical Engineering Science, 23:695–706, 1968.

- [25] L.W. Florschuetz, C.L. Henry, and A.Rashid Khan. Growth rates of free vapor bubbles in liquids at uniform superheats under normal and zero gravity conditions. *Interna*tional Journal of Heat and Mass Transfer, 12:1465–1489, 1969.
- [26] Yeong-Cheng Lien. Bubble growth rates at reduced pressure. PhD thesis, Massachusetts Institute of Technology, 1969.
- [27] S. J. Board and R. B. Duffey. Spherical vapour bubble growth in superheated liquids. Chemical Engineering Science, 26:263–274, 1971.
- [28] S. J. Board and A. D. Klimpton. Spherical vapoure bubble collapse. Chemical Engineering Science, 29:363–371, 1974.
- [29] Shigeo Fujikawa and Teruaki Akamatsu. Experimental investigations of cavitation bubble collapse by a water tube. Japan Society of Mechanical Engineers, 21(152): 223–230, 1978.
- [30] T G Theofanous, T H Bohrer, M C Chang, and P D Patel. Experiments and Universal Growth Relations for Vapor Bubbles With Microlayers. *Journal of Heat Transfer*, 100: 41–48, 1978.
- [31] Y. M. Chen and F. Mayinger. Measurement of heat transfer at the phase interface of condensing bubbles. *International Journal of Multiphase Flow*, 18(6):877–890, 1992.
- [32] Forrest R. Gilmore. The growth or collapse of a spherical bubble in a viscous compressible liquid. Technical report, California Institute of Technology, 1952.

- [33] M. S. Plesset and S. A. Zwick. The growth of vapor bubbles in superheated liquids.

  \*Journal of Applied Physics, 25(4):493–500, 1954.
- [34] M. S. Plesset and T. P. Mitchell. On the stability of the spherical shape of a vapor cavity in a liquid. *Quarterly of Applied Mathematics*, 13(4):419–430, 1955.
- [35] L.E. Scriven. On the dynamics of phase growth. *Chemical Engineering Science*, 10: 1–13, 1959.
- [36] B.B Mikic, W.M Rohsenow, and P Griffith. On bubble growth rates. International Journal of Heat and Mass Transfer, 13:657–666, 1970.
- [37] E. Pattantyus-H. Temperature variation and collapse time at the condensation of vapour bubble. *International Journal of Heat and Mass Transfer*, 15:2419–2426, 1972.
- [38] T. G. Theofanous and P. D. Patel. Universal relations for bubble growth. *International Journal of Heat and Mass Transfer*, 19:425–429, 1976.
- [39] Andrea Prosperetti and Milton S. Plesset. Vapour-bubble growth in a superheated liquid. Journal of Fluid Mechanicsl, 85:349–368, 1978.
- [40] A. Prosperetti and A. Lezzi. Bubble dynamics in a compressible liquid. part 1. first-order theory. *Journal of Fluid Mechanics*, 168:457–478, 1986.
- [41] Andrea Prosperetti. Vapor Bubbles. Annual Review of Fluid Mechanics, 49:221–248, 2017.
- [42] T. Theofanous, L. Biasi, H.S. Isbin, and H. Fauske. A theoretical study on bubble

- growth in constant and time-dependent pressure fields. Chemical Engineering Science, 24:885–897, 1969.
- [43] M. Dalle Donne and M. P. Ferranti. The growth of vapor bubbles in superheated Sodium. *International journal of heat and mass transfer*, 18:477–493, 1975.
- [44] Samuel W. J. Welch. Local simulation of two-phase flows including interface tracking with mass transfer. *Journal of Computational Physics*, 121:142–154, 1995.
- [45] H. S. Lee and H. Merte Jr. Spherical vapor bubble growth in uniformly superheated liquids. *International journal of heat and mass transfer*, 39:2427–2447, 1996.
- [46] Y Hao and Andrea Prosperetti. The dynamics of vapor bubbles in acoustic pressure fields. Physics of fluids, 11(8):2008–2019, 1999.
- [47] G. Son, V. K. Dhir, and N. Ramanujapu. Dynamics and heat transfer associated with a single bubble during nucleate boiling on a horizontal surface. *Journal of Heat Transfer*, 121:623–631, 1999.
- [48] I. Akhatov, O. Lindau, A. Topolnikov, R. Mettin, N. Vakhitova, and W. Lauterborn. Collapse and rebound of a laser-induced cavitation bubble. *Physics of Fluids*, 13(10): 2805–2819, 2001.
- [49] A.J. Robinson and R.L. Judd. Bubble growth in a uniform and spatially distributed temperature field. *International Journal of Heat and Mass Transfer*, 44:2699–2710, 2001.
- [50] G. Tomar, G. Biswas, A. Sharma, and A. Agrawal. Numerical simulation of bubble

- growth in film boiling using a coupled level-set and volume-of-fluid method. *Physics* of Fluids, 17:112103, 2005.
- [51] Binze Yang and Andrea Prosperetti. Vapour bubble collapse in isothermal and non-isothermal liquids. *Journal of fluid mechanics*, 601:253–279, 2008.
- [52] Siegfried Müller, Mathieu Bachmanna, Dennis Kröninger, Thomas Kurz, and Philippe Helluy. Comparison and validation of compressible flow simulations of laser-induced cavitation bubbles. *Computers and Fluids*, 38(9):1850–1862, 2009.
- [53] Edip Can and Andrea Prosperetti. A level set method for vapor bubble dynamics.

  \*Journal of Computational Physics, 231:1533–1552, 2012.
- [54] Sébastien Tanguy, Michaël Sagan, Benjamin Lalanne, Frédéric Couderc, and Catherine Colin. Benchmarks and numerical methods for the simulation of boiling flows. *Journal* of Computational Physics, 264:1–22, 2014.
- [55] Max Koch, Christiane Lechner, Fabian Reuter, Karsten Köhler, Robert Mettin, and Werner Lauterborn. Numerical modeling of laser generated cavitation bubbles with the finite volume and volume of fluid method, using openfoam. *Computers & Fluids*, 126:71–90, 2016.
- [56] Duc Q Nguyen, Ronald P Fedkiw, and Myungjoo Kang. A boundary condition capturing method for incompressible flame discontinuities. *Journal of Computational Physics*, 172(1):71–98, 2001.
- [57] Sébastien Tanguy, Thibaut Ménard, and Alain Berlemont. A level set method for vaporizing two-phase flows. *Journal of Computational Physics*, 221(2):837–853, 2007.

- [58] Frédéric Gibou, Liguo Chen, Duc Nguyen, and Sanjoy Banerjee. A level set based sharp interface method for the multiphase incompressible Navier–Stokes equations with phase change. *Journal of Computational Physics*, 222:536–555, 2007.
- [59] Lucia Rueda Villegas, Romain Alis, Mathieu Lepilliez, and Sébastien Tanguy. A Ghost Fluid/Level Set Method for boiling flows and liquid evaporation: Application to the Leidenfrost effect. *Journal of Computational Physics*, 316:789–813, 2016.
- [60] Lakshman Anumolu and Mario F. Trujillo. Gradient augmented level set method for phase change simulations. *Journal of Computational Physics*, 353:377–406, 2018.
- [61] Christopher E. Brennen. Cavitation and Bubble Dynamics. Cambridge University Press, 2014.
- [62] A D Okhotsimskii. The thermal regime of vapour bubble collapse at different Jacob numbers. *International Journal of Heat and Mass Transfer*, 31:1569–1576, 1988.
- [63] J. Naude and F. Méndez. Numerical analysis of an asymptotic model for the collapse of a vapor bubble. *Heat and Mass Transfer*, 43(4):325–331, 2007.
- [64] Mamoru Akiyama. Bubble collapse in subcooled boiling. *Bulletin of the JSME*, 16: 570–575, 1973.
- [65] PA Pavlov. Fast collapse of a vapor bubble. International Journal of Heat and Mass Transfer, 104:627–633, 2017.
- [66] P Hawtin, GA Henwood, and RA Huber. On the collapse of water vapour cavities in a bubble analogue apparatus. *Chemical Engineering Science*, 25(7):1197–1209, 1970.

- [67] H Delmas and H Angelino. Vapour bubble collapse: The influence of the initial radius and of subcooling. *Chemical Engineering Science*, 32(7):723–727, 1977.
- [68] V Prodanovic, D Fraser, and M Salcudean. Bubble behavior in subcooled flow boiling of water at low pressures and low flow rates. *International Journal of Multiphase Flow*, 28(1):1–19, 2002.
- [69] De-wen Yuan, Liang-ming Pan, Deqi Chen, Hui Zhang, Jing-hua Wei, and Yan-ping Huang. Bubble behavior of high subcooling flow boiling at different system pressure in vertical narrow channel. *Applied Thermal Engineering*, 31(16):3512–3520, 2011.
- [70] WX Tian, RH Chen, JL Zuo, SZ Qiu, GH Su, Y Ishiwatari, and Y Oka. Numerical simulation on collapse of vapor bubble using particle method. *Heat Transfer Engineering*, 35(6-8):753–763, 2014.
- [71] Christopher E Brennen. Fission of collapsing cavitation bubbles. *Journal of Fluid Mechanics*, 472:153–166, 2002.
- [72] Ichiro Ueno, Yasusuke Hattori, and Ryota Hosoya. Condensation and collapse of vapor bubbles injected in subcooled pool. *Microgravity Science and Technology*, 23(1):73–77, 2011.
- [73] Javier Rodríguez-Rodríguez, Alejandro Sevilla, Carlos Martínez-Bazán, and José Manuel Gordillo. Generation of microbubbles with applications to industry and medicine. *Annual Review of Fluid Mechanics*, 47:405–429, 2015.
- [74] Shigeo Fujikawa and Teruaki Akamatsu. Effects of the non-equilibrium condensation of

- vapour on the pressure wave produced by the collapse of a bubble in a liquid. *Journal* of Fluid Mechanics, 97:481–512, 1980.
- [75] R.I. Nigmatulin and N.S. Khabeev. Dynamics of Vapor Bubbles. Fluid Dynamics, 10: 415–421, 1975.
- [76] S. A. Klein. F-Chart: EES V10.118. http://www.fchart.com/ees/, 1992-2017.
- [77] Octave Levenspiel. Collapse of steam bubbles in water. Industrial & Engineering Chemistry, 51(6):787–790, 1959.
- [78] Andrea Prosperetti, Lawrence A. Crum, and Kerry W. Commander. Nonlinear bubble dynamics. Journal of Acoustical Society of America, 83(2):502–514, 1988.
- [79] Andrea Prosperetti. Bubble dynamics: some things we did not know 10 years ago. In Bubble Dynamics and Interface Phenomena, pages 3–16. Springer, 1994.
- [80] RI Nigmatulin, NS Khabeev, and FB Nagiev. Dynamics, heat and mass transfer of vapour-gas bubbles in a liquid. *International Journal of Heat and Mass Transfer*, 24 (6):1033–1044, 1981.
- [81] Y Hao and Andrea Prosperetti. The collapse of vapor bubbles in a spatially non-uniform flow. *International journal of heat and mass transfer*, 43(19):3539–3550, 2000.
- [82] D Juric and G Tryggvason. Computations of Boiling Flows. International Journal of Multiphase Flow, 24:387–410, 1998.
- [83] Samuel W.J. Welch and John Wilson. A Volume of Fluid Based Method for Fluid Flows with Phase Change. *Journal of Computational Physics*, 160:662–682, 2000.

- [84] Tao Ye, Wei Shyy, and Jacob N. Chung. A Fixed-Grid, Sharp-Interface Method for Bubble Dynamics and Phase Change. *Journal of Computational Physics*, 174:781–815, 2001.
- [85] Gihun Son. A Numerical Method for Bubble Motion with Phase Change. Numerical Heat Transfer, Part B: Fundamentals, 39:509–523, 2001.
- [86] Abhijit Mukherjee and Satish G. Kandlikar. Numerical simulation of growth of a vapor bubble during flow boiling of water in a microchannel. *Microfluidics and Nanofluidics*, 1:137–145, 2005.
- [87] Ding Li and Vijay K. Dhir. Numerical Study of Single Bubble Dynamics During Flow Boiling. Journal of Heat Transfer, 129:864, 2007.
- [88] Gihun Son and Vijay K. Dhir. Three-dimensional simulation of saturated film boiling on a horizontal cylinder. *International Journal of Heat and Mass Transfer*, 51:1156– 1167, 2008.
- [89] S. Hardt and F. Wondra. Evaporation model for interfacial flows based on a continuumfield representation of the source terms. *Journal of Computational Physics*, 227:5871– 5895, 2008.
- [90] Christian Kunkelmann and Peter Stephan. CFD Simulation of Boiling Flows Using the Volume-of-Fluid Method within OpenFOAM. Numerical Heat Transfer, Part A: Applications, 56:631–646, 2009.
- [91] D. Z. Guo, D. L. Sun, Z. Y. Li, and W. Q. Tao. Phase Change Heat Transfer Simulation

- for Boiling Bubbles Arising from a Vapor Film by the VOSET Method. Numerical Heat Transfer, Part A: Applications, 59:857–881, 2011.
- [92] M. Magnini, B. Pulvirenti, and J. R. Thome. Numerical investigation of hydrodynamics and heat transfer of elongated bubbles during flow boiling in a microchannel.

  International Journal of Heat and Mass Transfer, 59:451–471, 2013.
- [93] Yohei Sato and Bojan Ničeno. A sharp-interface phase change model for a massconservative interface tracking method. *Journal of Computational Physics*, 249:127– 161, 2013.
- [94] Seungwon Shin and Beomjoon Choi. Numerical simulation of a rising bubble with phase change. *Applied Thermal Engineering*, 100:256–266, 2016.
- [95] Yeng-Yung Tsui and Shi-Wen Lin. Three-dimensional modeling of fluid dynamics and heat transfer for two-fluid or phase change flows. *International Journal of Heat and Mass Transfer*, 93:337–348, 2016.
- [96] Isaac Perez-Raya and Satish G Kandlikar. Discretization and implementation of a sharp interface model for interfacial heat and mass transfer during bubble growth. International Journal of Heat and Mass Transfer, 116:30–49, 2018.
- [97] Muhammad Irfan and Metin Muradoglu. A front tracking method for direct numerical simulation of evaporation process in a multiphase system. *Journal of Computational Physics*, 337:132–153, 2017.
- [98] M.S. Plesset and Andrea Prosperetti. Bubble Dynamics and Cavitation. Annual Review of Fluid Mechanics, 9:145–185, 1977.

- [99] M.D. Mikhailov and A.P. Freire. The drag coefficient of a sphere: An approximation using shanks transform. *Powder Technology*, 237:432–435, 2013.
- [100] Douglas T. Ryddner. Advection of Reconstructed aVoF Method with Phase Change.
  PhD thesis, University of Wisconsin-Madison, 2018.
- [101] China Rama Lakshman Anumolu. Towards Numerical Methods for Two Phase Flow Simulations Undergoing Phase-change Phenomena. PhD thesis, The University of Wisconsin-Madison, 2017.
- [102] G. Son and V. K. Dhir. Numerical simulation of saturated film boiling on a horizontal surface. *Journal of Heat Transfer*, 119:525–533, 1997.
- [103] G. Son and V. K. Dhir. Numerical simulation of film boiling near critical pressures with a level set method. *Journal of Heat Transfer*, 120:183–192, 1998.
- [104] Moon Soo Lee, Amir Riaz, and Vikrant Aute. Direct numerical simulation of incompressible multiphase flow with phase change. *Journal of Computational Physics*, 344: 381–418, 2017.
- [105] Min Chai, Kun Luo, Changxiao Shao, Haiou Wang, and Jianren Fan. Interface-resolved detailed numerical simulation of evaporating two-phase flows with robin boundary conditions on irregular domains. *International Journal of Heat and Mass Transfer*, 145:118774, 2019.
- [106] Yohei Sato and Bojan Niceno. A conservative local interface sharpening scheme for the constrained interpolation profile method. *International Journal for Numerical Methods* in Fluids, 70:441–467, 2012.

- [107] Alexandre Joel Chorin. Numerical solution of the navier-stokes equations. *Mathematics* of computation, 22(104):745–762, 1968.
- [108] Sreeyuth Lal, Yohei Sato, and Bojan Niceno. Direct numerical simulation of bubble dynamics in subcooled and near-saturated convective nucleate boiling. *International Journal of Heat and Fluid Flow*, 51:16–28, 2015.
- [109] Yohei Sato and Bojan Niceno. Pool boiling simulation using an interface tracking method: From nucleate boiling to film boiling regime through critical heat flux. *International Journal of Heat and Mass Transfer*, 125:876–890, 2018.
- [110] Yohei Sato and Bojan Niceno. Large eddy simulation of upward co-current annular boiling flow using an interface tracking method. *Nuclear Engineering and Design*, 321: 69–81, 2017.
- [111] Ronald P Fedkiw, Tariq Aslam, Barry Merriman, and Stanley Osher. A non-oscillatory eulerian approach to interfaces in multimaterial flows (the ghost fluid method). *Journal of computational physics*, 152(2):457–492, 1999.
- [112] Vuko Vukčević, Hrvoje Jasak, and Inno Gatin. Implementation of the ghost fluid method for free surface flows in polyhedral finite volume framework. *Computers & fluids*, 153:1–19, 2017.
- [113] Majid Haghshenas, James A Wilson, and Ranganathan Kumar. Finite volume ghost fluid method implementation of interfacial forces in piso loop. *Journal of Computational Physics*, 376:20–27, 2019.

- [114] Xu-Dong Liu, Ronald P Fedkiw, and Myungjoo Kang. A boundary condition capturing method for poisson's equation on irregular domains. *Journal of computational Physics*, 160(1):151–178, 2000.
- [115] OpenCFD. OpenFOAM The Open Source CFD Toolbox User's Guide. ESI-OpenCFD, 1706 edition, 6 June 2017.
- [116] Suraj S Deshpande, Lakshman Anumolu, and Mario F Trujillo. Evaluating the performance of the two-phase flow solver interfoam. *Computational science & discovery*, 5(1):014016, 2012.
- [117] Raunak Bardia, Zhi Liang, Pawel Keblinski, and Mario F Trujillo. Continuum and molecular-dynamics simulation of nanodroplet collisions. *Physical Review E*, 93(5): 053104, 2016.
- [118] Suraj S. Deshpande, Lakshman Anumolu, and Mario F. Trujillo. Evaluating the performance of the two-phase flow solver interfoam. *Computational Science and Discovery*, 5(1):014016, 2012.
- [119] Johan Roenby, Henrik Bredmose, and Hrvoje Jasak. A computational method for sharp interface advection. *Royal Society Open Science*, 3:160405, 2016.
- [120] D. L. Youngs. Numerical Methods for Fluid Dynamics, chapter Time-dependent multimaterial flow with large fluid distortion, pages 273–285. Academic Press, New York, 1982.
- [121] W. J. Rider and D. B. Kothe. Reconstructing volume tracking. *Journal of Computational Physics*, 141:112–152, 1998.

- [122] D. J. E. Harvie and D. F. Fletcher. A new volume of fluid advection algorithm: the stream scheme. *Journal of Computational Physics*, 162:1–32, 2000.
- [123] E. Aulisa, S. Manservisi, R. Scardovelli, and S. Zaleski. A geometrical area-preserving volume-of-fluid advection method. *Journal of Computational Physics*, 192:355–364, 2004.
- [124] Alexandre Joel Chorin. The numerical solution of the navier-stokes equations for an incompressible fluid. Bulletin of the American Mathematical Society, 73(6):928–931, 1967.
- [125] Raad I Issa. Solution of the implicitly discretised fluid flow equations by operator-splitting. *Journal of computational physics*, 62(1):40–65, 1986.
- [126] D. Bhaga and M. E. Weber. Bubbles in viscous liquids: shapes, wakes and velocities. Journal of Fluid Mechanics, 105:61–85, 1981.
- [127] G. Ryskin and L. G. Leal. Numerical solution of free-boundary problems in fluid mechanics. part 2. buoyancy-driven motion of a gas bubble through a quiescent liquid. *Journal of Fluid Mechanics*, 148:19–35, 1984.
- [128] M. Sussman, K. M. Smith, M. Y. Hussaini, M. Ohta, and R. Zhi-Wei. A sharp interface method for incompressible two-phase flow. *Journal of Computational Physics*, 221: 469–505, 2007.
- [129] Thomas Bonometti and Jacque Magnaudet. An interface-capturing method for incompressible two-phase flows. validation and application to bubble dynamics. *International Journal of Multiphase Flow*, 33:109–133, 2007.

- [130] Zhaoyuan Wang, Jianming Yang, Bonguk Koo, and Frederick Stern. A coupled level set and volume-of-fluid method for sharp interface simulation of plunging breaking waves. *International Journal of Multiphase Flow*, 35:227–246, 2009.
- [131] S. Hysing, S.Turek, D. Kuzmin, N. Parolini, E. Burman, S. Ganesan, and L. Tobiska. Quantitative benchmark computations of two-dimensional bubble dynamics. *International Journal for Numerical Methods in Fluids*, 60:1259–1288, 2009.
- [132] Mirco Magnini. CFD Modeling of Two-Phase Boiling Flows in the Slug Flow Regime with an Interface Capturing Technique. PhD thesis, University of Bologna, 2012.
- [133] Jeremiah U Brackbill, Douglas B Kothe, and Charles Zemach. A continuum method for modeling surface tension. *Journal of computational physics*, 100(2):335–354, 1992.
- [134] Vasilios Alexiades. Mathematical modeling of melting and freezing processes. Routledge, 2017.
- [135] BK Sreedhar, SK Albert, and AB Pandit. Cavitation damage: Theory and measurements—a review. Wear, 372:177–196, 2017.
- [136] T Brooke Benjamin and Ao T Ellis. The collapse of cavitation bubbles and the pressures thereby produced against solid boundaries. *Philosophical Transactions for the Royal Society of London. Series A, Mathematical and Physical Sciences*, pages 221–240, 1966.
- [137] S Al Issa, P Weisensee, and R Macián-Juan. Experimental investigation of steam bubble condensation in vertical large diameter geometry under atmospheric pressure

- and different flow conditions. *International Journal of Heat and Mass Transfer*, 70: 918–929, 2014.
- [138] Satish G. Kandlikar. Fundamental issues related to flow boiling in minichannels and microchannels. *Experimental Thermal and Fluid Science*, 26:389–407, 2002.
- [139] I-Shih Liu. A continuum mechanics primer-on constitutive theories of materials, 2006.